Reliability-Based Analysis and Design of Reinforced Concrete Buildings against Progressive Collapse

A THESIS

SUBMITTED TO THE FACULTY OF THE GRADUATE SCHOOL

OF THE UNIVERSITY OF MINNESOTA

BY

BING XUE

IN PARTIAL FULFILLMENT OF THE REQUIREMENTS

FOR THE DEGREE OF

DOCTOR OF PHILOSOPHY

Jia-Liang Le, Advisor

October, 2015

Acknowledgements

I wish to express my deepest thanks and appreciation to my advisor, Professor Jia-Liang Le. During my four years' doctoral studies, Professor Le gave me incredible support and guidance to help me overcome numerous theoretical and practical challenges till the last moment of finishing this thesis.

I would like to thank all the people that helped me out during my graduate studies at the University of Minnesota. I would also like to thank the members of my thesis committee, Professor Susan Mantell, Professor Arturo Schultz and Professor Henryk Stolarski for their valuable suggestions on my thesis revision. I would like to thank Professor Steve Wojtkiewicz for introducing me to the software toolkit, DAKOTA, which greatly facilitates my research closely related with probabilistic analysis, uncertainty quantification and design optimization. I would like to thank my fellow graduate student Davide Giannuzzi for helping me with the debugging of computer programming and numerical modeling. I would like to thank my fellow graduate student Qingzhi Liu for the helpful discussion with him on reinforced concrete material and structures.

Dedication

To my wife, son and parents

Abstract

The objective of this research is to develop a new probabilistic framework to facilitate reliability-based analysis and design of reinforced concrete (RC) buildings against progressive collapse. In this study, a two-scale numerical model is developed to investigate the probabilistic collapse behavior of RC buildings subjected to local structural damage. In this model, a set of coarse-scale cohesive elements is used to model the failure behavior of potential damage zones (PDZ) in various RC structural members. The constitutive properties of the cohesive elements and their probability distributions are determined from detailed stochastic finite element simulations of the PDZs by taking into account the uncertainties in various material properties. The two-scale model is validated both experimentally and numerically for different types of structural subassemblages. With this two-scale model, the nonlinear dynamic analysis is applied to study the collapse behavior of a 2D 30-story RC frame structure and a 3D 10-story RC building subjected to sudden column removal. The results of the present probabilistic analysis are discussed in comparison with the existing deterministic approach, which reveals the importance of the probabilistic method for analysis of progressive collapse.

To further improve the computational efficiency of the proposed probabilistic method for reliability-based design optimization against progressive collapse, a linear elastic cohesive model inspired by the concept of energetic equivalence is developed based on the two-scale model. In this simplified method, the damage status of the PDZ is determined by comparing the elastic energy stored in the cohesive element with the actual energy dissipation capacity of the PDZ. This linear elastic cohesive model is combined with a sequential analysis method to identify different possible failure paths that could lead to collapse initiation. This energetic-equivalent model is applied to analyze the collapse

initiation risk of a prototype RC building. The results are compared with those obtained by using the nonlinear dynamic analysis. It is shown that the simplified model is far more efficient than the conventional nonlinear dynamic analysis, and it yields a reasonable upper bound of the collapse probability. Finally, this energetic-equivalent cohesive model is incorporated into a general optimization method for the optimum retrofitting of RC buildings to achieve a target collapse risk.

Contents

Acknowledgements **i**

Dedication **ii**

Abstract **iii**

List of Tables **viii**

List of Figures **ix**

1 Introduction **1**

1.1 Background 1

1.2 Objective 3

2 Two-Scale Computational Model **7**

2.1 Background 7

2.2 Model Description 9

2.3 Coarse-Scale Modeling of Potential Damage Zone 10

2.3.1 Effective Concrete Section 11

2.3.2 Longitudinal Reinforcement 13

2.3.3 Unloading and Reloading Behaviors 14

2.4 Fine-Scale Model Calibration 16
2.5 Conclusion 19

3 Model Validation **29**
3.1 Background 29
3.2 Experimental Validation 30
3.2.1 Frame Subassemblage 30
3.2.2 Flat-Slab Systems 34
3.3 Numerical Validation 37
3.4 Conclusion 39

4 Risk Assessment of RC Buildings with Two-Scale Model **54**
4.1 Background 54
4.2 Stochastic Simulation Framework 56
4.3 Risk Assessment of a 2D 30-Story RC Frame Structure 57
4.3.1 Collapse Simulation 58
4.3.2 Results and Discussion 60
4.4 Risk Assessment of a 3D 10-Story RC Building with a Flat-Slab System 64
4.4.1 Material Properties and External Loading 65
4.4.2 Results and Discussion of Deterministic Calculations 66
4.4.3 Results and Discussion of Stochastic Calculations 68
4.5 Conclusion 71

5 Simplified Energy-Based Analysis Method **94**
5.1 Background 94
5.2 Energetic-Equivalent Elastic Cohesive Model 96
5.3 Sequential Linear Elastic Structural Analysis 100
5.4 Application to Risk Analysis of RC Building 103

5.4.1 Description of Analysis 104
5.4.2 Results and Discussion 105
5.5 Conclusions 107

6 Reliability-Based Design Optimization 113
6.1 Background 113
6.2 Optimization Methods 115
6.2.1 Gradient-Based Methods 115
6.2.2 Non-gradient-Based Local Methods 117
6.2.3 Non-gradient-based Global Methods 118
6.3 Design Optimization for Structural System against Progressive Collapse 119
6.4 Application to A 10-Story RC Building 120
6.4.1 Description 120
6.5 Results and Discussion 123
6.6 Conclusion 127

7 Conclusions and Future Research 133
7.1 Conclusions 133
7.2 Outlook for Future Research 135

References 137

List of Tables

3.1 Material properties of concrete and steel for experimental validation. . . 41

4.1 Material properties for stochastic simulations. 73

4.2 Probability distribution for all RC sections. 74

4.3 Partial correlation matrix of the beam-end section. 75

4.4 Calculated probabilities of collapse extents. 76

4.5 Probability distributions of superimposed gravity loads. 77

4.6 Partial correlation matrix of one beam-end PDZ. 78

4.7 Partial correlation matrix of one interior-column PDZ. 79

4.8 Probability distribution for all RC sections. 80

4.9 Calculated collapse load factor α_l using deterministic analysis. 81

4.10 Calculated occurrence probabilities of collapse extents. 82

5.1 Comparison of calculated collapse probabilities. 109

6.1 Optimization results with three different algorithms. 128

6.2 Values of all design variables for the final optimal retrofitting scheme. . 129

List of Figures

1.1 Examples of progressive collapse. 6

2.1 Separation of cohesive constitutive law. 21

2.2 Cohesive element modeling of structural subsystems: a) frame subassemblage, b) beam-slab system, c) flat-slab system, and d) wall panel. . . . 22

2.3 Cohesive behavior of effective concrete section and longitudinal reinforcement. 23

2.4 Approximated shape of longitudinal reinforcement. 24

2.5 Analytical model for slip amount calculation. 25

2.6 Boundary condition for PDZ calibration: a single-mode loading; b) mixed-mode loading. 26

2.7 Random stress-strain curves for concrete in tension and compression and steel reinforcement. 27

2.8 Effective concrete section with random material properties for fine-scale calibration. 28

3.1 Design of the frame subassemblage for pushdown test. 42

3.2 Calibration results with fine-scale FE model under single-mode and mixed-mode loadings. 43

3.3 Result comparison of the PDZ responses under positive and negative bending. 44

3.4 Numerical implementation of detailed FE model and two-scale model. . 45
3.5 Result comparison between two numerical models and experimental testing [67]. 46
3.6 Detailed design of four flat-slab systems: a) Elsterner and Honestad (1956); b) Liu etal. (2015); c) Kanoh and Yoshizaki (1979); d) Hawkins etal. (1989). 47
3.7 Two-scale model of four flat-slab systems: a) Elsterner and Honestad (1956); b) Liu etal. (2015); c) Kanoh and Yoshizaki (1979); d) Hawkins etal. (1989). 48
3.8 Result comparison of four flat-slab systems: a) Elsterner and Honestad (1956); b) Liu etal. (2015); c) Kanoh and Yoshizaki (1979); d) Hawkins etal. (1989). 49
3.9 Schematic of a 10-story RC building with three subassemblages. 50
3.10 Detailed design of three subassemblages: a) interior span; b) exterior span; c) one three-story wall panel). 51
3.11 Two-scale model of three subassemblages: a) one quarter of four interior spans; b) four corner spans; c) one three-story wall panel). 52
3.12 Result of three subassemblages: a) one quarter of four interior spans; b) four corner spans; c) one three-story wall panel). 53
4.1 Stochastic analysis framework for risk assessment of building structures. 83
4.2 Distribution of sample points for the MCS and LHS methods with 5 samples. 84
4.3 Structural Design of a 2D 30-story RC frame structure. 85
4.4 Probabilistic distribution of cohesive properties of one PDZ. 86
4.5 Five initial damage scenarios for collapse analysis. 87
4.6 Four final collapse extents. 88

4.7 A 10-story RC building with eight initial damage scenarios. 89
4.8 Two-scale model of the 10-story prototype building. 90
4.9 Probabilistic distributions of cohesive properties of one beam-end PDZ. 91
4.10 Probabilistic distributions of cohesive properties of one interior-column PDZ. 92
4.11 Three final collapse extents of the 3D prototype building. 93
5.1 Energy-based equivalent stiffness calculation. 110
5.2 Flowchart for the failure sequence search with the simplified energy-based analysis method. 111
5.3 Concentrated damage regions on the floor. 112
6.1 Double-loop optimization framework for collapse risk control. 130
6.2 Strengthened traction-separation relationship for the PDZ ($i = s$ or c). . 131
6.3 Curves of convergence for all four optimization attempts. 132

Chapter 1

Introduction

1.1 Background

Progressive collapse is commonly defined as the large-scale failure of structures due to the propagation of local structural damage. Fig. 1.1 presents some notable cases of progressive collapse. This type of structural failure usually causes significant financial losses and human casualties. Collapses of the Alfred P. Murrah Federal Building and the World Trade Center Towers have also created profound societal and political impacts. Over the years, the risk of local structural damage caused by various abnormal events, such as gas explosion, blast, impact and fire, has continuously increased and, at the same time, the public has also been more aware of the severe consequences of progressive collapse. This leads to a continuing interest in assessing and improving the vulnerability of our buildings against progressive collapse.

Driven by gravitation, the local structural damage could possibly propagate into the other intact parts of the building and eventually lead to building collapse. This collapse process naturally involves various complex mechanisms, such as material damage and fracture, large deformation, debris impact and dynamics. Over the past two decades, a

considerable amount of efforts have been devoted to the investigation of various mechanisms involved in the progressive collapse. The existing analytical modeling techniques mainly focused on the behavior of individual structural components under impact loading [56, 108]. In some recent studies [19, 16, 94, 63, 85], 1D analytical models were used to study the collapse of the World Trade Center Towers based on a continuum framework, where the collapse front was assumed to have a simplified 1D motion described by either the d'Alembert principle or an extended Lagrange formulation. Although analytical models provide an efficient means for investigating the collapse behavior, they are not able to capture the physical process of the formation of the crush-front in the building. Moreover, in many cases the crush front may not occupy the entire floor, where the motion of the crush-front cannot be described by 1D models.

In recent years, there also have been several attempts to experimentally study the collapse behavior of 2D and 3D structural frames subjected to local column removal [67, 88, 110]. Because of the high experimental costs, controlled physical experiments on progressive collapse are usually limited to structural subassemblages or reduced-scale structural systems. Very few experimental studies have investigated the progressive collapse resistance of full-scale buildings [92, 90, 99]. Due to the limitations of analytical and experimental investigations, numerical simulation has become the major tool for the analysis of progressive collapse of buildings. Substantial efforts have been devoted toward developing various numerical models for progressive collapse with different levels of details, which include, the finite element model [6, 46], the discrete element model [75], the macro-element model [61, 11] and the applied element model [47].

These numerical models [61, 11, 75, 6, 46] were largely used for the alternate path analysis according to the recommendations of the General Services Administration (GSA) [42] and the U.S. Department of Defense Unified Facilities Criteria (UFC) [29],

where the initial structural damage was modeled by sudden removal of some key structural elements, such as columns and walls. These existing models have provided insights into various mechanisms of progressive collapse, which are essential for assessing the collapse resistance of buildings. However, these models cannot quantify the actual collapse risk since they were all developed in a deterministic framework. This also leads to the fact that the concept of structural reliability has not been fully incorporated into the current design recommendations for progressive collapse. By contrast, reliability-based design approach has widely been adopted for other hazard loading, such as earthquakes and wind.

1.2 Objective

The objective of this dissertation is to develop a new stochastic computational model to facilitate the reliability-based analysis and design of reinforced concrete (RC) buildings against progressive collapse. This entire dissertation is planned as follows:

- Chapter 2 presents a two-scale computational model for simulating the nonlinear behavior of various structural components of RC buildings (i.e. beams, columns, walls and slabs) under several multi-axial loading states. In this model, we consider that the nonlinear behavior of various structural members can be fully captured by a set of nonlinear cohesive elements, which represent the potential damage zones (PDZs) that could possibly form during the collapse process. The constitutive properties of the cohesive element are determined from detailed finite element simulations of the PDZs, which naturally take into account two physical length scales, namely the PDZ size and the crack band width of concrete material.

- In Chapter 3 the proposed two-scale model is validated both experimentally and numerically for different types of structural subassemblages. The experimental

validation involves the simulations of a recent experiment on a frame subassemblage under a column removal scenario and several experiments on flat-slab systems. In addition, the proposed model is also validated through the comparisons with the conventional FE simulations for other types of structural subassemblages including a flat-slab system, a frame-slab system and a wall panel.

- In Chapter 4 the two-scale computational model is applied to evaluate the collapse risks of a 2D 30-story RC frame structure and a 3D 10-story RC structure with a flat-slab system, by incorporating uncertainties from external loading and material properties. The collapse risks of these two prototype buildings are quantified for different initial local damage scenarios. Meanwhile, the existing deterministic simulation approach, which relies on mean material properties and gravity loading, is also used to investigate the collapse potential of these two buildings. By comparing the results from both the deterministic and stochastic simulations, the implication of the traditional deterministic approach on the structural reliability is studied.

- Chapter 5 proposes a simplified energy-based analysis method to further improve the computational efficiency of the aforementioned probabilistic analysis method. In this method, a linear cohesive element is developed to model the PDZs of different RC structural members based on an energetic equivalence principle. The linear cohesive element model is implemented in a sequential analysis framework to pursue the most probable failure sequence for a specific set of cohesive properties and load levels. Coupled with existing sampling methods, this sequential linear elastic analysis can efficiently evaluate the collapse initiation risk. Meanwhile, it is shown that this simplified method would yield an upper bound of the collapse risk.

- Chapter 6 establishes a reliability-based design optimization (RBDO) framework to search for the most cost-effective retrofitting scheme to ensure a target collapse risk. This RBDO framework is constructed by incorporating the proposed linear cohesive model into an optimization method. The design optimization uses a two-stage approach in which the non-gradient-based optimization method is first used to reach the region near the optimal solution point, and the gradient-based approach is then adopted to locate the optimal point.

- Chapter 7 summarizes the main results of this study and concludes this dissertation.

Figure 1.1: Examples of progressive collapse.

Chapter 2

Two-Scale Computational Model

2.1 Background

In the past decade, extensive efforts have been directed toward the development of computational models for the simulations of the collapse behavior of buildings. The full-scale continuum finite element (FE) simulation of progressive collapse can capture various detailed nonlinear structural behaviors directly from the material constitutive responses, but the computational cost is usually very high especially for large-scale buildings [6]. In a recent study [75], a discrete element model was developed to simulate the nonlinear structural behavior as well as debris impact, in which structural members, such as the beams, columns and slabs, were represented by spheres connected by springs. Similar to FE simulations, the main limitation of the discrete element model is the high computational cost.

Meanwhile, various reduced-order numerical models have been proposed to achieve a balance between model accuracy and computational affordability. Early attempts

include the development of a damage-dependent beam element within the framework of the slope-deflection method [55, 41]. Recent efforts have focused on macro-element based modeling of buildings [61, 11], which combines the beam-column elements and nonlinear springs for beam-column joints. The constitutive behavior of beam-column elements and connection springs were directly determined from the material constitutive relationships. This model was first developed for 2D steel and reinforced concrete (RC) frames [61, 11], and was later extended to 3D steel buildings [6]. The macro-element model provides an efficient means of modeling RC structures under large deformation. However, the model is not designed to effectively capture the disintegration of the structural members and subsequent debris impact during the collapse process.

Most recently, the applied element model (AEM) [47] was developed to evaluate the collapse potential of RC buildings after the removal of vertical support elements, i.e. columns and walls, according to the UFC guidelines [29]. In this model, the structural members are modeled by a set of solid elements connected by three uncoupled springs. This numerical model was designed to simulate the collapse initiation by capturing the fracture of component caused by the excessive gravity loading due to the initial loss of vertical elements, in which the component fracture is modeled by breakage of springs. However, these uncoupled springs cannot realistically represent the nonlinear behavior of RC components under complex loading conditions, such as combination of axial force, bending moment, torsion and shear. Meanwhile, the calibration of spring behavior does not consider the finite size of the structural damage zone.

This chapter presents a two-scale numerical model for simulating structural collapse of RC buildings subjected to given local structural damage. By using a nonlinear and a coarse-scale model physical calibrated procedure, the model is able to capture the nonlinear behavior of various structural components such as beams, columns, slabs and walls under complex loading conditions during the collapse process.

2.2 Model Description

In this study, a two-scale computational model is developed based on the concept of cohesive fracture [13, 30, 49, 18], which has widely been used in the fracture mechanics community. In this model, each structural member is modeled by a set of nonlinear cohesive elements representing the potential damage zones (PDZs) that could possibly form during collapse process, and the rest of the structural member is modeled by linear elastic elements. Therefore, the overall nonlinear structural behavior is fully determined by the mechanical behavior of the PDZs.

The locations of the PDZs must be identified a priori based on the qualitative understanding of the behaviors of structural components under impact loading. For instance, the PDZs in the beams are assumed to be at the quarter-span intervals and the two ends (Fig. 2.2a-b) to account for both single- and double-curvature bending. The PDZs of columns are placed at the mid-height and the two ends (Fig. 2.2a) according to the Shanley column model [96, 15, 53]. For slabs, the PDZs are located along the potential yield lines as well as at locations of potential punching shear failure around the columns [54]. Fig. 2.2b-c shows the PDZs in a typical frame-slab system and a flat-slab system, respectively. Based on a recently developed truss model for RC walls [82], the wall panel is divided into several subpanels and the PDZs are placed along their diagonals and perimeters (Fig. 2.2d).

Similar to cohesive modeling of material fracture, the cohesive element has a zero thickness, and the height of the cohesive element is chosen to be $0.85D_e$ for beams and slabs and $0.75D_e$ for walls and columns, where D_e is the distance between the centroid of the tensile reinforcement and the extreme material fiber in compression [70, 80]. The width of the cohesive element is equal to the actual width of the structural member. Each cohesive element consists of four integration points, which are allowed to exhibit different constitutive properties depending on the design of steel reinforcement.

Therefore, a single cohesive element can be used to simulate the behavior of PDZ under tension, compression, shear, bending, and combinations of these loading modes.

It is obvious that the determination of the mechanical behavior of the PDZs is critical for correctly capturing the overall failure behavior of structural members. It should be pointed out that the constitutive behavior of cohesive elements used for PDZs is determined by both material properties and structural dimension and geometry of PDZs. This is fundamentally different from the conventional use of cohesive elements for analysis of fracture of concrete materials, where the cohesive behavior is solely determined by the material properties [49, 18]. As will be described in detail later, the constitutive behavior of the cohesive elements is calibrated from the fine-scale FE simulations of the actual PDZs under different loading modes.

It is worthwhile to mention that the present model shares the similar spirit of the recently developed applied element model [47], where in both models the overall structural failure is represented by a set of local nonlinear elements. Nevertheless, different from the applied element model, in which each failure mode is represented by different uncoupled nonlinear springs, the present model uses a single cohesive element to model the mixed-mode failure of the PDZ. Furthermore, in the present model the constitutive behavior of the cohesive elements reflects the actual behavior of the PDZ. By contrast, the behavior of the nonlinear springs of the applied element model is characterized only by the material behavior, where the detailed PDZ geometry is not considered

2.3 Coarse-Scale Modeling of Potential Damage Zone

To formulate the constitutive relationship of the cohesive element for the PDZ, we separate each PDZ into two parts, namely the effective concrete section, which includes concrete and transverse reinforcement (if applicable), and the longitudinal reinforcement as indicated by Fig. 2.1. Therefore, the traction-separation relationship for each

integration point of the cohesive element can be written as

$$\sigma_n(w_n, w_m, w_l) = \sigma_n^c(w_n, w_m, w_l) + \rho_s \sigma_n^s(w_n, w_m, w_l) \tag{2.1a}$$

$$\tau_m(w_n, w_m, w_l) = \tau_m^c(w_n, w_m, w_l) + \rho_s \tau_m^s(w_n, w_m, w_l) \tag{2.1b}$$

$$\tau_l(w_n, w_m, w_l) = \tau_l^c(w_n, w_m, w_l) + \rho_s \tau_l^s(w_n, w_m, w_l) \tag{2.1c}$$

where σ_n, τ_i $(i = m, l)$ = total tractions in the normal and two orthogonal shear directions (Fig. 2.3a), σ_n^c, τ_i^c = normal and shear tractions of the effective concrete section, σ_n^s, τ_i^s = normal and shear tractions of the longitudinal reinforcement, w_n, w_i = normal and shear separations, and ρ_s = longitudinal reinforcement ratio.

2.3.1 Effective Concrete Section

The constitutive behavior of the effective concrete section is formulated based on the concept of mixed-mode cohesive fracture [25, 24, 113, 50, 39, 84]. To account for the interaction between normal and shear loading, we define the effective separation as $\bar{w} = \sqrt{w_n^2 + \alpha_i^2(w_m^2 + w_l^2)}$, where α_i $(i = t, c)$ = constants corresponding to tension-shear and compression-shear loading modes, respectively. It is easy to determine the effective traction $\bar{\sigma}$ that is work-conjugate to the effective separation $\bar{w}$ by using the principle of virtual work:

$$\bar{\sigma} \mathrm{d}\bar{w} = \sigma_n^c \mathrm{d}w_n + \tau_m^c \mathrm{d}w_m + \tau_l^c \mathrm{d}w_l \tag{2.2}$$

The increment of effective separation, $\mathrm{d}\bar{w}$ can be written as $\mathrm{d}\bar{w} = (\partial\bar{w}/\partial w_n)\mathrm{d}w_n + (\partial\bar{w}/\partial w_m)\mathrm{d}w_m + (\partial\bar{w}/\partial w_l)\mathrm{d}w_l$. With the definition of $\bar{w}$, Eq. 2.2 can be rewritten as:

$$\bar{\sigma}\left(\frac{w_n}{\bar{w}}\mathrm{d}w_n + \frac{\alpha_i^2 w_m}{\bar{w}}\mathrm{d}w_m + \frac{\alpha_i^2 w_l}{\bar{w}}\mathrm{d}w_l\right) = \sigma_n^c \mathrm{d}w_n + \tau_m^c \mathrm{d}w_m + \tau_l^c \mathrm{d}w_l \tag{2.3}$$

Since Eq. 2.3 is valid for any arbitrary values of $\mathrm{d}w_n$, $\mathrm{d}w_m$ and $\mathrm{d}w_l$, we must have

$$\sigma_n^c = \bar{\sigma}\sin\theta \tag{2.4a}$$

$$\tau_m^c = \alpha_i\bar{\sigma}\cos\theta\sin\varphi \tag{2.4b}$$

$$\tau_l^c = \alpha_i\bar{\sigma}\cos\theta\cos\varphi \tag{2.4c}$$

where mode mixity angles are defined as $\theta = \tan^{-1}\left(w_n/\alpha_i\sqrt{w_m^2+w_l^2}\right)$ and $\varphi = \tan^{-1}(w_m/w_l)$. Based on this formulation, it is evident that the effective concrete section can be fully determined by $\bar{\sigma}-\bar{w}$ relationship.

It has transpired from previous studies that the total energy dissipation and the peak load capacity are the main governing factors for the overall progressive collapse behavior [19, 16, 52, 94, 112, 104]. Therefore, the detailed shape of $\bar{\sigma}-\bar{w}$ curve is not of particular importance especially when the entire collapse process involves failures of a large number of cohesive elements (i.e. PDZs). In the present model, a simple bilinear curve is adopted to describe $\bar{\sigma}-\bar{w}$ relationship (Fig. 2.3b):

$$\bar{\sigma}(\bar{w}) = \begin{cases} \sigma_p\dfrac{\bar{w}}{\bar{w}_y} & (\bar{w}\le\bar{w}_y) \\ \sigma_p\dfrac{(\bar{w}_u-\bar{w})}{(\bar{w}_u-\bar{w}_y)} & (\bar{w}_y<\bar{w}\le\bar{w}_u) \\ 0 & (\bar{w}_u<\bar{w}) \end{cases} \tag{2.5}$$

where σ_p = maximum effective traction, $\bar{w}_y$ = effective separation at the maximum effective traction, $\bar{w}_u$ = ultimate effective separation at which the effective traction becomes zero, and $\sigma_p, \bar{w}_y$ and $\bar{w}_u$ are further related to the cohesive properties under single-mode loading:

$$\sigma_p = |\sigma_{ip}|\sin^{\beta_i}|\theta| + \alpha_i^{-1}|\sigma_{\tau p}|\cos^{\beta_i}|\theta| \tag{2.6}$$

$$\bar{w}_y = [(|w_{iy}|\sin|\theta|)^{\gamma_i} + (|w_{\tau y}|\cos|\theta|)^{\gamma_i}]^{1/\gamma_i} \tag{2.7}$$

$$\bar{w}_u = [(|w_{iu}|\sin|\theta|)^{\gamma_i} + (|w_{\tau u}|\cos|\theta|)^{\gamma_i}]^{1/\gamma_i} \tag{2.8}$$

where $\sigma_{ip}(i = t, c)$ = maximum tensile and compressive cohesive strengths of the effective concrete section, respectively, $\sigma_{\tau p}$ = shear cohesive strength of the effective concrete section, $w_{iy}(i = t, c)$ = separations at which the cohesive traction reaches σ_{ip} under pure tensile and compressive loading, respectively, $w_{iu}(i = t, c)$ = separations at which the cohesive traction becomes zero under pure tensile and compressive loading, respectively, $w_{\tau y}, w_{\tau u}$ = separations at which the cohesive traction reaches $\sigma_{\tau p}$ and 0, respectively, under pure shear loading, and $\beta_i, \gamma_i(i = t, c)$ = calibrated constants describing the tension-shear interaction and compression-shear interaction, respectively.

2.3.2 Longitudinal Reinforcement

The traction-separation relationship for longitudinal reinforcement is formulated based on the uniaxial stress-strain curve of the reinforcement modified by the bond-slip effect. Following Lew et al. [67], the total strain in the reinforcement can be calculated as

$$\epsilon(\sigma) = \epsilon_0(\sigma) + \frac{\Delta_s(\sigma)}{L_p} \tag{2.9}$$

where σ = actual bar stress, $\epsilon_0(\sigma)$ = bar strain corresponding to σ without considering the bond-slip effect, Δ_s = total slip at the bar stress of σ, and L_p = length of the PDZ. The actual bar strain $\epsilon_0(\sigma)$ can be calculated based on the actual uniaxial bar stress-strain curve. The total slip amount $\Delta_s(\sigma)$ is determined through an analytical model [95]:

$$\Delta_s = \begin{cases} \dfrac{\epsilon_0 \sigma d_b}{8\sqrt{f_c'}} & (\epsilon_0 \leq \epsilon_y) \\ \dfrac{\epsilon_0 \sigma d_b}{8\sqrt{f_c'}} + \dfrac{(\epsilon_0 + \epsilon_y)(\sigma - \sigma_y) d_b}{4\sqrt{f_c'}} & (\epsilon_0 \geq \epsilon_y) \end{cases} \tag{2.10}$$

where d_b is the diameter of the reinforcing bar; $f_c^{'}$ is the uniaxial compressive strength of concrete; σ_y and ϵ_y are the stress and strain of the reinforcing bar at the yielding point, respectively.

In this analytical model, the bond stress profile along the longitudinal reinforcement is characterized by two piecewise constant segments as indicated by Fig. 2.5 from [95] when the bar stress exceeds the yielding stress. Within the development length l_{dy}, the bar stress σ_s accumulates linearly with a uniform bond stress of $u_b = 1.0\sqrt{f_c'}$ till reaching the yielding stress σ_y while within the segment l_d' the bar stress exceeds the yielding stress and linearly increases with a reduced uniform bond stress of $u_b = 0.5\sqrt{f_c'}$. As the load increases, the reinforcing bar will eventually either rupture or be pulled out of the concrete. Therefore, the ultimate bar strength σ_{su} of the bar is determined by the minimum value of the bar rupture strength and the bar pullout strength, where the bar pullout strength can be calculated from the ACI recommendation [3].

Once the modified stress-strain relationship for the longitudinal reinforcement, $\sigma = f(\epsilon)$, is obtained, the corresponding cohesive tractions can be determined by projecting the actual bar stress onto the normal and shear directions. Since the length of the PDZ is relatively small, we may approximate the deformation of the reinforcement as a straight line with a slope $\phi = \tan^{-1}[\sqrt{w_m^2 + w_l^2}/(L_p + w_n)]$ as indicated by Fig. 2.4. Therefore, the total bar elongation w can be calculated as $w = \sqrt{(L_p + w_n)^2 + w_m^2 + w_l^2} - L_p$. The normal and shear tractions can be obtained as: $\sigma_n^s = f(w/L_p)\cos\phi$, $\tau_m^s = f(w/L_p)\sin\phi\sin\varphi$ and $\tau_l^s = f(w/L_p)\sin\phi\cos\varphi$. Since the slope ϕ is usually small, the longitudinal reinforcement would not contribute significantly to the shear behavior of the PDZ.

2.3.3 Unloading and Reloading Behaviors

During the collapse process, the structural components often experience some degrees of oscillation. However, it is expected that the amplitude of the oscillation is not large due to damping and therefore the failure of the structural components is mainly governed by the monotonic cohesive behavior. Here we include some simple representations of

unloading and reloading behavior for the cohesive elements. Following Eqs. 2.1a - 2.1c, we consider the effective concrete section and longitudinal steel reinforcement separately.

For the effective concrete section, the unloading and reloading behaviors are described in the $\bar{\sigma} - \bar{w}$ space. The unloading and reloading paths are enclosed by the monotonic effective traction-separation curve given by Eq. 2.5. Within the monotonic traction-separation envelope, the unloading-reloading path can be described as

$$\delta\bar{\sigma} = \bar{E}(1-\omega)\delta\bar{w} \tag{2.11}$$

where $\delta\bar{\sigma}, \delta\bar{w}$ = incremental effective traction and separation, $\bar{E} = \sigma_p/\bar{w}_y$ = undamaged elastic modulus, and ω = damage parameter, which represents the maximum damage extent that the cohesive element has ever experienced during the loading history. In this study, we write ω as

$$\omega = \min\left(\frac{\max_t\left[(1-E_p/\bar{E})h(\theta)\right]}{h(\theta)}, 1\right) \tag{2.12}$$

where $\max_t(x)$ = maximum value of x during the entire loading history, E_p = secant modulus = $\bar{\sigma}/\bar{w}$, and $h(\theta)$ describes the effect of the existing damage on the current material behavior when the degree of mode mixity changes. For instance, the damage in tension would have a small influence on the loading and unloading stiffnesses in compression whereas the damage in compression would greatly affect the loading and unloading stiffnesses in tension [66]. In this study, we assume that $h(\theta) = 0.6 - 0.4\sin\theta$ for the sake of simplicity since it is expected that the mode mixity ratio would not change significantly during the oscillation . Fig. 2.3b presents a schematic of unloading and reloading paths for the effective concrete section for a fixed degree of mode mixity.

For longitudinal steel reinforcement, the unloading and reloading responses can be computed based on the standard linear isotropic and kinematic strain hardening model [54], in which the unloading and reloading stiffnesses are equal to the initial elastic

modulus as shown in Fig. 2.3c, and the unloading and reloading paths are fully enclosed by the monotonic effective traction-separation curve.

2.4 Fine-Scale Model Calibration

As mentioned in Chapter 1, the objective of this study is to perform reliability based design and analysis of RC buildings against progressive collapse, which requires risk quantification through the stochastic structural analysis. Within the proposed framework, it is clear that the probabilistic distribution of mechanical behavior of the cohesive element (e.g. peak strengths and fracture energies) must be calibrated from the actual random structural behavior of the PDZs. Following Eqs. 2.1a to 2.1c, we calibrate the cohesive behavior and its associated randomness of the effective concrete section and longitudinal reinforcement separately.

For the effective concrete section, the randomness of cohesive behavior is determined by the random cohesive strengths and fracture energies under pure tension, compression and shear, which are denoted by σ_{tp}, σ_{cp}, $\sigma_{\tau p}$ and $G_{ft}, G_{fc}, G_{f\tau}$, respectively. The mode mixity parameters (i.e. α_i, β_i and γ_i) are considered to be deterministic. Therefore, the calibration consists of two parts: 1) stochastic FE simulations of the effective concrete section under tensile, compressive and shear loading, to determine the probability distributions of the respective cohesive strengths and fracture energies under single-mode loading; and 2) deterministic FE simulations of the effective concrete section under respective combined tension-shear and combined compression-shear loading with four different levels of mode mixity to determine the mode mixity parameters. The loading conditions for this calibration process are presented in Figure 2.6. The mode mixity parameters are calibrated by optimum fits of the simulated cohesive strengths and total energy dissipations under mixed-mode loading.

In both deterministic and stochastic FE simulations of the effective concrete section, the length of the PDZ, L_p, is chosen to be equal to $0.5D$ for beams, columns and walls [77, 9] and to be equal to D for slabs, where D = depth of the beam and column or the thickness of the slab and wall. Concrete material is modeled by continuum finite elements whereas the shear reinforcement is modeled by truss elements. The constitutive behavior of concrete is described by the damage plasticity model [66] and the constitutive behavior of the steel reinforcement is described by the isotropic kinematic hardening model. It is assumed that the uniaxial tension behavior follows an exponential softening curve. For uniaxial compression, we consider the unconfined and confined concrete separately. For the unconfined concrete section (i.e. concrete cover), a simple linear softening behavior is assumed, where the unconfined compressive strength and critical energy dissipation can be obtained from the standard compression test. For the confined concrete section (i.e. concrete section enclosed by the transverse reinforcement), we modify the unconfined compressive stress-strain relation such that the simulated behavior of the confined concrete section with the transverse reinforcement would match that simulated by using the widely used Kent and Park model in which the effect of transverse reinforcement on the behavior of concrete is implicitly included [60, 74].

In order to avoid the spurious mesh sensitivity for concrete materials due to its strain-softening behavior, we adopt the crack band model, where the FE mesh size is set to be the crack band width, i.e. approximately three times the maximum aggregate size [18]. Meanwhile, it has recently been demonstrated that for concrete the crack band width is approximately equal to the spatial auto-correlation length of the random field of material properties [40]. Therefore, in the stochastic FE simulations, we can consider that the material properties of each finite element are spatially uncorrelated as shown in Fig. 2.8, where different colors of the concrete and steel reinforcement

elements indicates different material properties among adjacent elements.

For the deterministic FE simulations, the mean material properties of concrete and steel reinforcement are used. For the stochastic FE simulations, the concrete strengths in tension and compression (f_t' and f_c') and the yielding and ultimate strengths (f_{sy} and f_{su}) of steel reinforcement are considered as random variables. The strains corresponding to these strengths are considered to be deterministic. Furthermore, f_t' and f_{sy} are assumed to be fully correlated with f_c' and f_{su} through the ratios of their mean values, respectively. The random stress-strain relationships of the concrete and steel are shown in Fig. 2.7. The present model indicates that the fracture energy density (i.e. the area under the stress-strain curve) is also random and is fully correlated to the respective material random strength. It is noted that the same statistical correlation between material strength and fracture energy density has recently been used for stochastic simulations of concrete fracture [40].

For the cohesive behavior of the longitudinal reinforcement, both total energy dissipation G_{fs} and ultimate strength σ_{su} are considered as two random variables. These two variables are calibrated based on the stress-strain relationship of the bare steel and the bond-slip behavior. The ultimate strength is determined by the minimum value of the bar pullout strength and the bar rupture strength. The total energy dissipation is calculated as the area under the modified bar stress-strain curve. As mentioned before, the random constitutive behavior of the bare steel is characterized by its random yield and ultimate strengths. The random pullout strength is calculated by applying the Monte Carlo method to the ACI bond strength equation [3], which is presented as bellow:

$$\frac{T_b}{(f_c')^{1/4}} = \frac{A_b f_s}{(f_c')^{1/4}} = [63 l_d (c_m + 0.5 d_b) + 2130 A_b](0.1\frac{c_M}{c_m} + 0.9) + 2226 t_r t_d \frac{N A_{tr}}{n} + 66 \quad (2.13)$$

where T_b is the bar force at bond failure in lb; A_b is the are of the bar in^2; d_b is the diameter of the bar in in; f_s is the bar stress at bond failure in psi; $f_c^{'}$ is the

compressive strength of concrete in psi; l_d is the development length in in; c_m and c_M are the minimum and maximum value of c_s and c_b in in; c_s is the minimum of c_{so} and $c_{sl} + 0.25$; c_{sl} is equal to half of the clear spacing between steel bars in in; c_{so} and c_b are the side and bottom cover thicknesses, respectively, in in; N is the number of transverse bar crossing the development length l_d; A_{tr} is the area of transverse bar crossing the potential splitting plane in in^2; n is the bar number developed along the splitting plane; t_r and t_d is equal to $9.6R_r + 0.28$ and $0.72d_b + 0.28$, respectively; R_r is the ratio between the rib area to the product of bar perimeter and rib spacing. The corresponding probability distributions of aforementioned relevant model parameters can also be found in [27]. With this information, the probability distributions of the total energy dissipation and the ultimate strength for the longitudinal reinforcement are calculated.

2.5 Conclusion

In this chapter, a new cohesive-fracture type computational model is developed for various structural components, to capture their nonlinear behaviors under general multi-axial loading states. The coarse-scale cohesive model is designed to essentially capture the energy dissipation of the PDZ under general mixed-mode loading. The cohesive behavior of the nonlinear elements for each PDZ can be physically calibrated by finite element simulations of the PDZ. It is noted that the proposed model naturally takes into account two physical length scales, namely the PDZ size and the crack band width. This is crucial for correctly capturing the nonlinear behavior of the PDZ due to the strain-softening behavior of concrete material. The PDZ size can be determined based on the experimental observation of the damage zone in RC structural members. The crack band width is set to be equal to three times the aggregate size of concrete, which is also approximately equal to the autocorrelation length of the random field of material

properties of concrete.

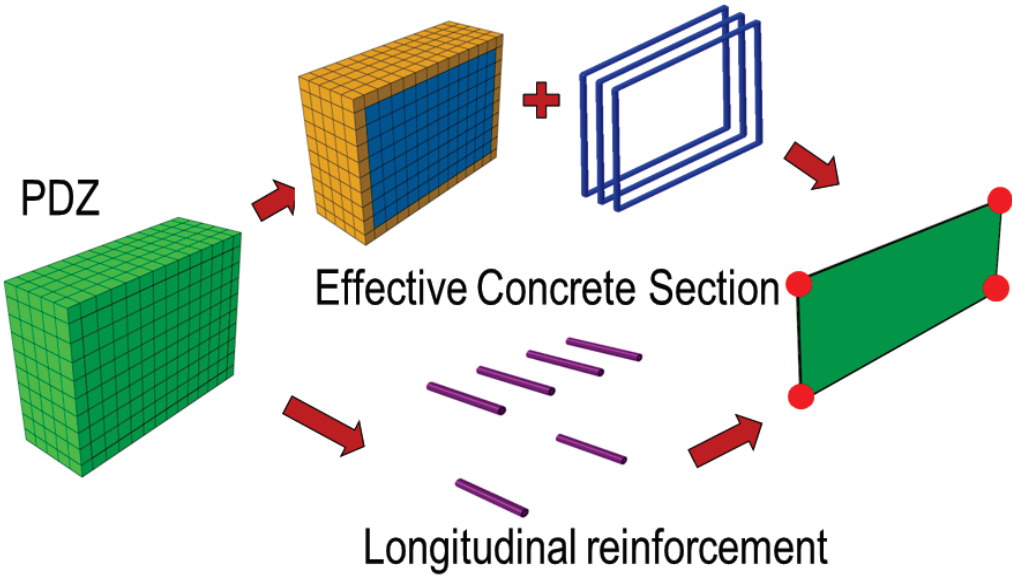

Figure 2.1: Separation of cohesive constitutive law.

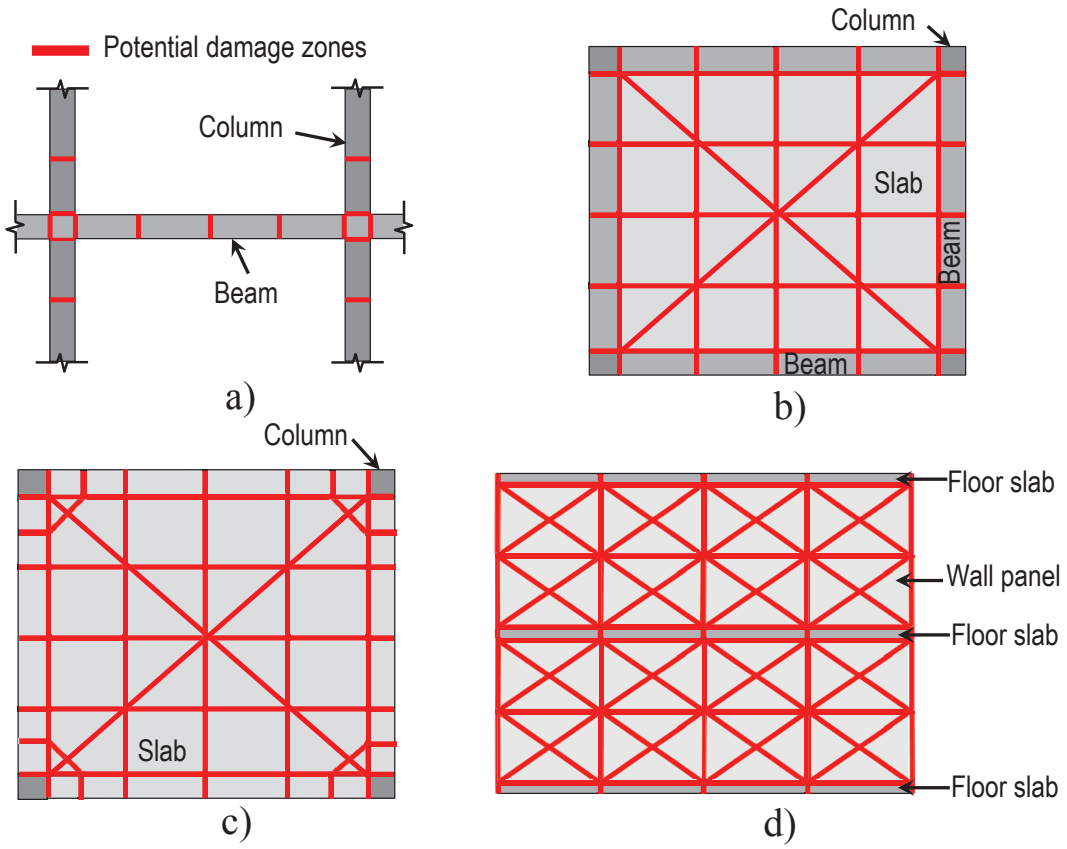

Figure 2.2: Cohesive element modeling of structural subsystems: a) frame subassemblage, b) beam-slab system, c) flat-slab system, and d) wall panel.

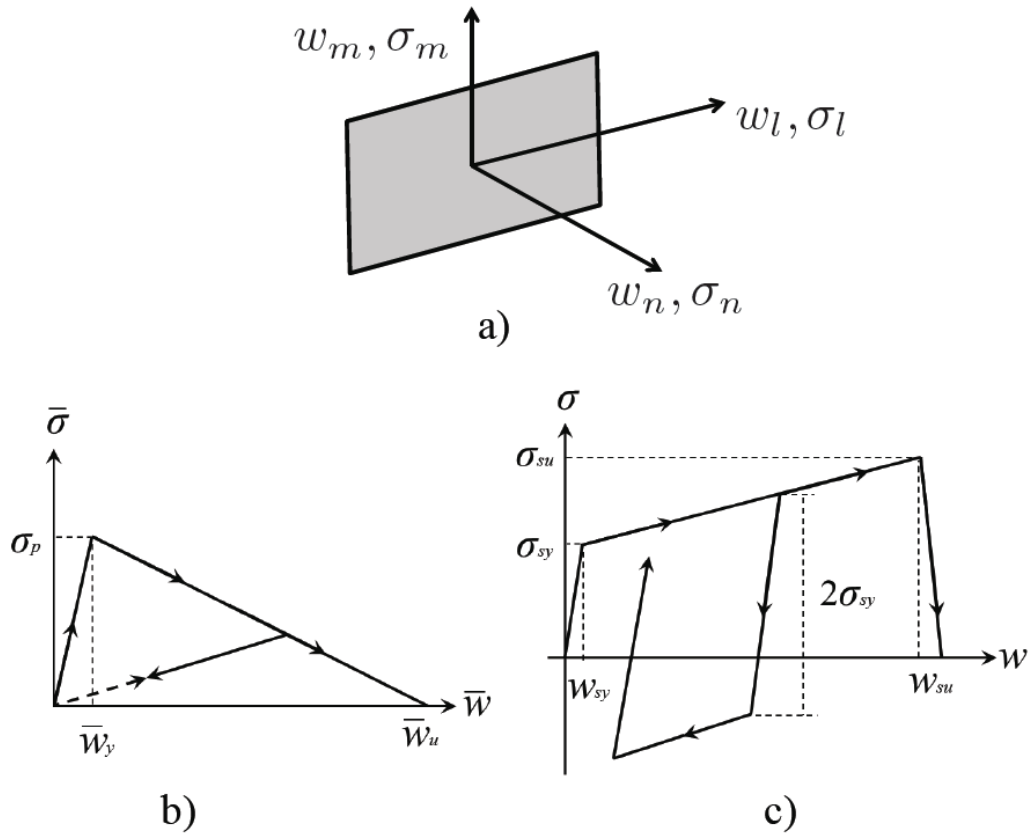

Figure 2.3: Cohesive behavior of effective concrete section and longitudinal reinforcement.

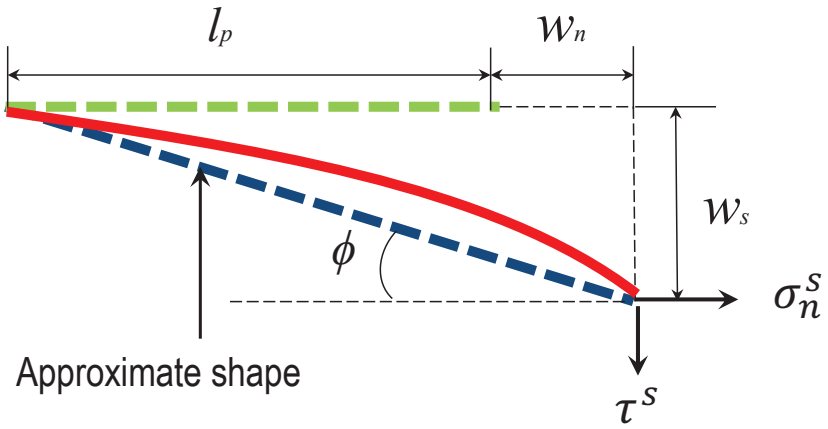

Figure 2.4: Approximated shape of longitudinal reinforcement.

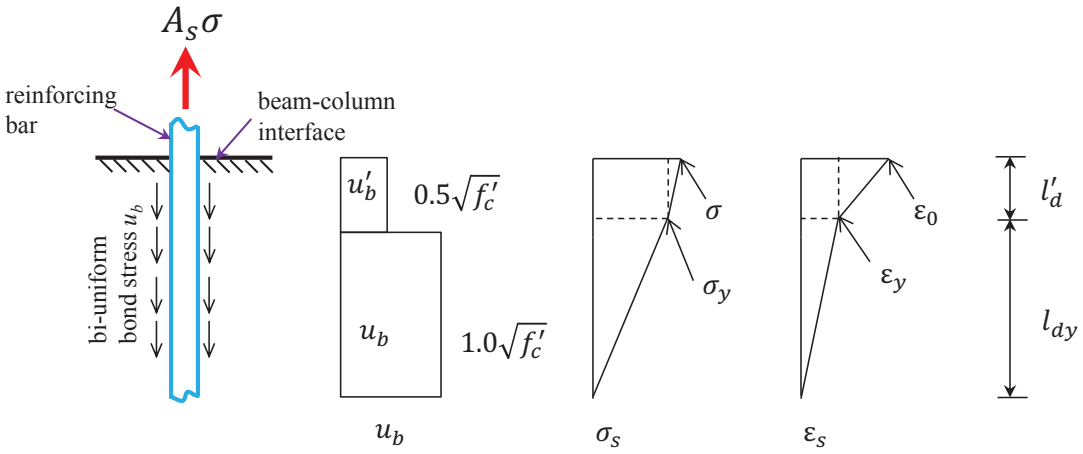

Figure 2.5: Analytical model for slip amount calculation.

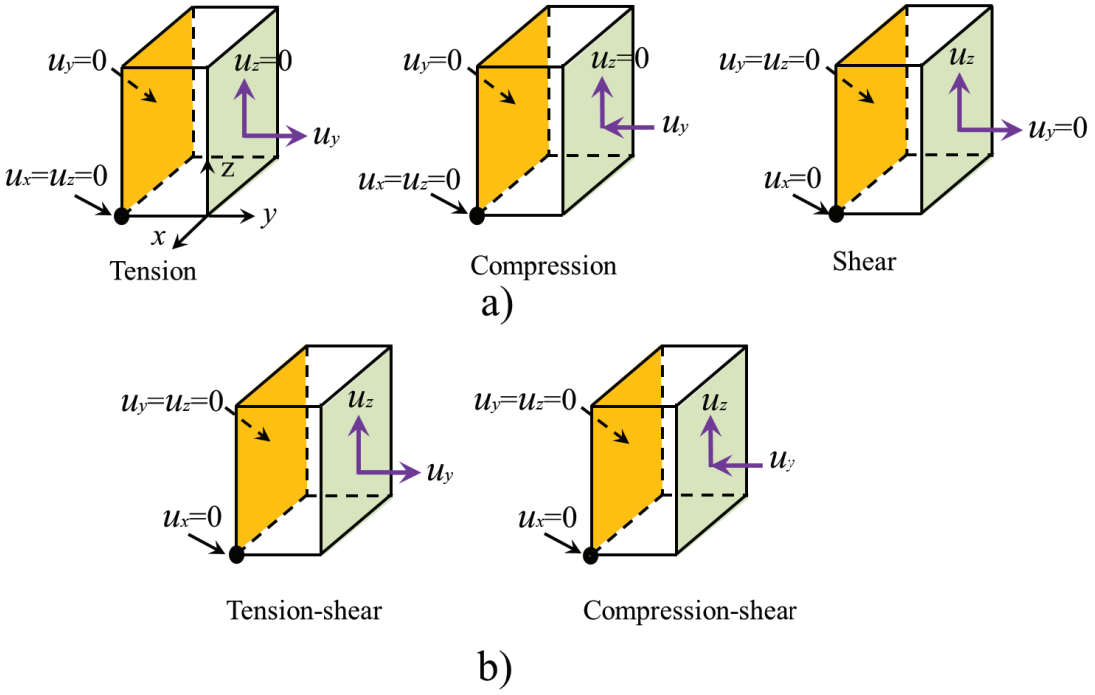

Figure 2.6: Boundary condition for PDZ calibration: a single-mode loading; b) mixed-mode loading.

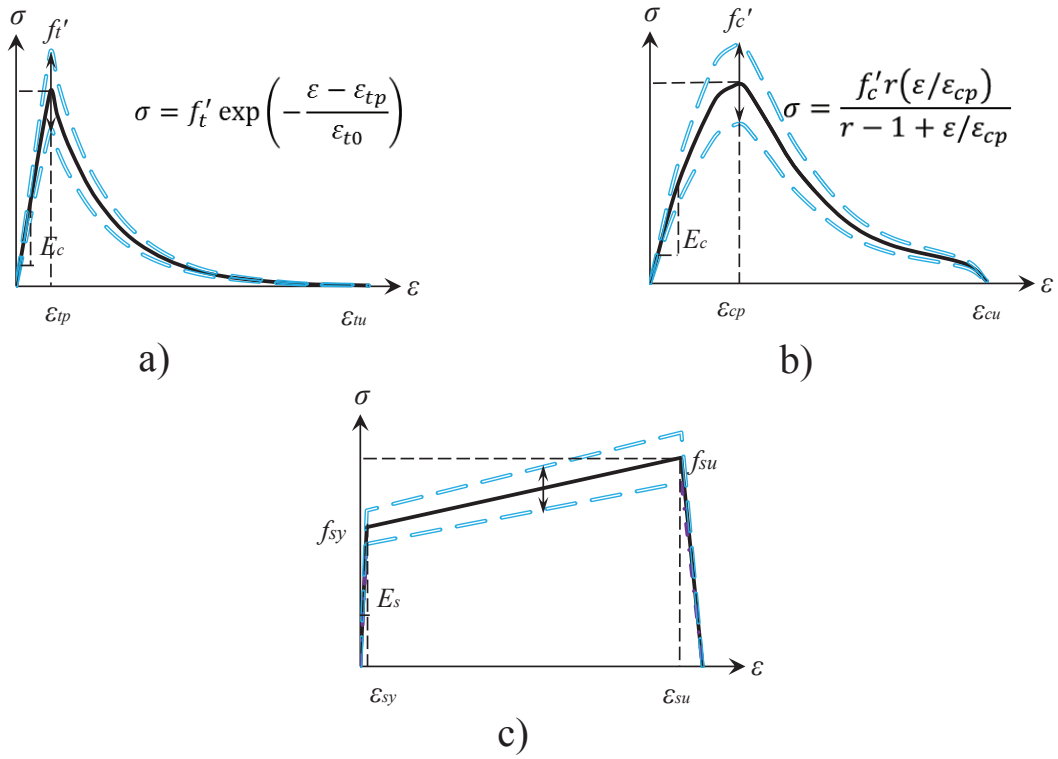

Figure 2.7: Random stress-strain curves for concrete in tension and compression and steel reinforcement.

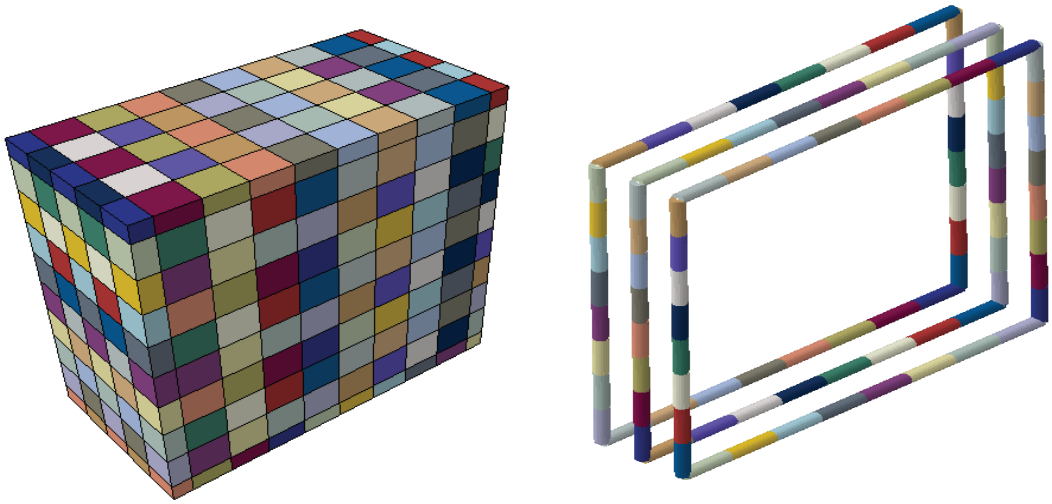

Figure 2.8: Effective concrete section with random material properties for fine-scale calibration.

Chapter 3

Model Validation

3.1 Background

To better understand of the mechanisms of progressive collapse, a number of experimental studies have been performed to study the global or local collapse behavior of RC buildings subject to initial damage. In [90] and [92], collapse resistance of two RC buildings, a six-story hotel building in San Diego, CA, constructed as early as 1924 and an 11-story hotel in Houston, TX, built in 1973, were investigated by suddenly removing one or two columns and observing the ensuing structural responses during the controlled demolition . However, controlled experiments on collapse of full-scale buildings are rare due to the prohibitive cost. Laboratory testing on structural collapse behavior is often limited to full-scale or reduce-scale structural subassemblage. For instance, a pushdown test on a 2D RC frame subassemblage was performed by National Institute of Standards and Technology (NIST) [67] to study the collapse behavior of this subassemblage under a central column removal scenario. A series of experiments has been performed to investigate the failure mechanisms of flat-slab systems under various boundary and loading conditions, which include: 1) concentric gravity loading on a simply supported flat slab

conducted by [36]; 2) concentric gravity loading on the slab with lateral constraints [69]; 3) torsional loading tests on the slab [59]; and 4) uneven gravity loading tests on the slab [45].

In this study, we validate the two-scale model against several previous experimental testing results and numerical simulations by the conventional FE simulations for different types of structural subassemblages. The experimental validation includes: 1) a pushdown test of a RC frame subassemblage conducted by NIST [88], where the applied loading and boundary condition resembled a column removal scenario and 2) four previous experiments on RC flat-slab systems by [69, 36, 45, 59] under different loading conditions, which include concentric downward loading with or without lateral constraints, eccentric downward loading and torsional loading. The numerical validation involves the comparisons of the structural responses of three different types of RC subassemblage, e.g. a frame-slab subassemblage, a flat-slab system and a shear wall panel obtained by the proposed two-scale model and the standard FE model. The focus of the present validation is on the accuracy of the cohesive element modeling of PDZs for the overall mean structural behavior. This is because, if the mean structural behavior can be well modeled by the cohesive elements, it can be reasonably expected that the stochastic response of the structural members in terms of the ultimate loading capacity and the energy dissipation can be well captured by the random constitutive behavior of the cohesive elements.

3.2 Experimental Validation

3.2.1 Frame Subassemblage

The proposed model is first tested against a push-down experiment on a RC frame subassemblage [88, 67], which was recently performed by the NIST. The detailed structural

design of this frame subassemblage is shown in Fig. 3.1. In order to investigate the nonlinear structural behavior under a column removal scenario, a downward displacement was applied at the location of the center column till the ultimate failure of the entire [88, 67].

Calibration of Cohesive Properties

To simulate this subassemblage test using the proposed two-scale model, the proposed constitutive relationship of the cohesive elements is calibrated through fine-scale FE simulations of the PDZ of the RC beams and columns. Since in this calculation the interest is the mean structural behavior, we only perform the deterministic fine-scale FE simulations to obtain the mean cohesive properties. For the FE simulations, we consider that the concrete and steel reinforcement have the stress-strain relationships as shown in Fig. 2.7 and the material properties for concrete and steel can be obtained from [67] as listed in Table 3.1.

We follow the calibration procedure discussed in Chapter 2. The traction-separation law of the longitudinal reinforcement under normal loading can be directly calculated based on Eq. 2.9. The uniaxial tensile and compressive behaviors of the effective concrete section can be obtained from the FE simulation of the PDZ without the longitudinal reinforcement. We note that the tensile resistance of the cohesive element is mainly due to the longitudinal reinforcement and therefore the tensile behavior of the effective concrete section is not critical. With these calibrations, we can obtain the cohesive behavior of the potential damage zone under uniaxial tension and compression. Fig. 3.2 shows that the cohesive behavior agrees well with the simulated behavior of a typical PDZ of beams under tension and compression. The traction-separation law under pure shear loading can be calibrated from the FE simulation of the PDZ under shear deformation, as shown in Fig. 3.2. Note that for compressive and shear loading

we consider the entire PDZ to fail once the concrete is totally damaged.

To calibrate the effect of the mode mixity, we simulate the response of the same PDZ under combined tension-shear and compression-shear loading with different degrees of mode mixity (Fig. 3.2). It is clear that, under the combined tension-shear loading, the normal traction-separation relation is still governed by the longitudinal reinforcement, and for different degrees of mode mixity the ultimate displacement of the longitudinal reinforcement varies. This may be explained by the FE simulation, which shows that large shear deformation would increase the elongation of the reinforcement, and further with the bond-slip effect, the reinforcement bars exhibit some curvature, which causes both the ultimate displacement and strength to vary. Based on the results in Fig. 3.2, we can obtain the mean behavior under single-mode loading (i.e. energy dissipation capacity and peak strength) and the values controlling the mixed-mode behavior, which are: α_c=0.54, β_c=0.30 and γ_c=2.00 for coupled compression-shear loading and α_t=2.25, β_t=1.00 and γ_t=2.00 for coupled tension-shear loading. Due to the simplified assumption on the shape of the softening cohesive law, we are not able to match the detailed fine-scale FE simulations exactly. Nevertheless, we calibrate all model parameters based on the optimum fits of the peak cohesive traction and total energy dissipations for all the loading scenarios, which are the governing factors of the collapse behavior.

As mentioned in Chapter 2, the cohesive element is designed to capture the flexural behavior of the entire PDZ. To demonstrate this capacity of the cohesive modeling of the PDZ, both the detailed FE model and one single cohesive element representing one PDZ are used to simulate the flexural behavior of the PDZ at the beam end under both positive and negative bending. The result comparison in Fig. 3.3 shows that the flexural behavior of the PDZ under these two bending conditions can be well captured by one single cohesive element from the elastic range to the yielding range till the total failure due to the reinforcement rupture.

Simulation of Frame Subassemblage Test

With the calibrated cohesive properties, we perform a deterministic simulation of the subassemblage test. Fig. 3.5 shows the simulated load-deflection curve and its comparison with the experimental measurement. It can be seen that the two-scale model can well capture the overall load capacity as well as the energy dissipation capacity of the frame subassemblage. It is noted that the present model does not match the measured load-deflection curve point by point due to the fact that we used a simplified constitutive relationship for the cohesive element with an aim of capturing the peak strength and energy dissipation.

Meanwhile, it is found that the present model is able to capture the main failure mechanism of the frame subassemblage, i.e. the arching effect and the catenary cation. The simulation shows that within the first ascending branch the entire beam is mainly in compression due to the arching effect gradually developed in the beam bounded by side columns. During the development of this arching effect, the top of the beam sections around the center column and the bottom of the beam sections near the side columns are in compression, accompanied by the shift of the neutral axis and the push of the side columns towards outside. As the loading continues, the overall resistance reaches its first peak before the concrete material at the top part of the beam section near the center column starts to get crushed. Afterwards, the resistance drops significantly due to concrete crushing until the catenary action gradually develops in beams, where the longitudinal reinforcement is mainly in tension and provides the overall resistance. As the vertical displacement increases, the catenary action is further developed, which leads to the second ascending branch of the force-deflection curve. Eventually, the longitudinal reinforcement ruptures in tension and the frame subassemblage loses its resistance at a maximum displacement of about 1.1 m. The simulated sequence of failure mechanisms agrees well with the experimental observations [88, 67].

In parallel with the proposed two-scale model, we also use the conventional FE model to simulate the behavior of this frame subassmeblage. In the FE simulation, the finite element size of concrete material is kept equal to 100 mm, which is about three times the maximum aggregate size. The constitutive behavior of concrete is considered to follow the aforementioned damage plasticity model. Steel reinforcement is modeled by truss elements, and the constitutive relationship is described by the stress-strain curve of the steel shown in Fig. 2.7, which is further modified by the bond-slip effect (Eq. 2.9). Fig. 3.5 shows the result of this FE simulation together with the result of the two-scale model and the experimental measurement. It is seen that the FE model agrees with the experimental result, which validates the FE model. Meanwhile, the result of the FE model is also consistent with the result of the two-scale model in terms of the peak load capacity and the total energy dissipation, which serves as a numerical verification of the two-scale model. However, the two-scale model which takes about only six minutes to finish the simulation saves up to 98% of the computational cost of the detailed FE model, which requires as long as around 10 hours by using the same computer.

3.2.2 Flat-Slab Systems

In addition to frame structures, we also consider four previous experiments on RC flat-slab systems with different types of loading and boundary conditions, which include: 1) a simply supported flat slab under concentric vertical loading without lateral constraint (Fig. 3.6a) [36]; 2) a flat slab under concentric vertical loading with lateral constraint (Fig. 3.6b) [69]; 3) a flat slab under torsion (Fig. 3.6c) [59]; and 4) a simply supported flat slab under uneven gravity loading (Fig. 3.6d) [45]. The mean mechanical properties of the cohesive elements are determined through the calibration procedure described in the previous section, where the stress-strain curves of concrete and steel reinforcement

are considered to follow Fig. 2.7. The material properties of concrete and steel reinforcement for these four experiments are obtained from the corresponding experimental records [36, 69, 45, 59] and listed in Table 3.1.

Fig. 3.8 compares the simulated load-deflection responses with the experimental measurements for all four cases. It is seen that the simulated and measured responses agree with each other reasonably well. The details of the simulated structural behaviors and the corresponding experimental observations are described as follows:

1) For specimen 1, a vertical downward displacement is applied on the top of the center column and the four edges of the slab simply sit on the supports, which are free to expand laterally. The present simulation shows that the overall stiffness of the slab degrades considerably after the bottom part of the slab around the center column cracks in tension. As the deflection continues to increase, the upper part of the slab around the column undergoes a combination of compressive and shear loading while the tensile force at the bottom of the slab is mainly taken by the steel reinforcement. At a deflection of 5.7 mm, the reinforcement at the bottom of the slab along the direction with the lower reinforcement ratio first reaches the yielding point. This computed deflection at this yielding point agrees well with that measured in the test, which is around 7 mm. Eventually, the top part of the slab around the column fails predominantly in shear, which is consistent with the experimental observation where the slab is punched through by the column at the end of testing.

2) For specimen 2, a vertical downward displacement is applied on the top of the center column and there are two clamps on each side of the slab to constrain the lateral motion of the slab. The failure mechanism of this specimen is very similar to that of specimen 1. During the loading process of the numerical simulation, the slab section around the column first experiences tensile concrete cracks and reinforcement yielding near the slab bottom surface. The ultimate failure is characterized by the

punching shear failure of concrete. Fig. 3.8 shows that the two-scale model can predict accurately both overall and detail nonlinear behaviors of this flat-slab subassemblage with lateral constraint.

3) For specimen 3, a torsional loading is applied on the column stud in the direction parallel to the short edge of the slab. The simulation shows that torsional cracks first develop at the corner of the slab-column interface. As the twisting angle increases, the slab reaches its peak load capacity and three cohesive elements at the slab-column corner experience a significant amount of damage. Such a damage pattern is consistent with the experimental observation [59]. Beyond the peak load, it is found that the load-deflection response exhibits a plateau with a slight decrease in load capacity, which indicates a relatively ductile behavior. The simulation shows a final drastic drop in load capacity at a twisting angle of about 0.0165 rad due to severe shear damage propagation from the corner of the column stud towards the far end of the slab. In the actual experiment, this failure mechanism occurred at a twisting angle about 0.018 rad, which agrees well with the simulation.

4) For specimen 4, uneven vertical loads are applied at multiple points close to the edge of the slab. In the simulation, it is observed that damage first occurs along the slab-column interface on the side where AV loading is applied. This damage subsequently propagates towards the two edges of the slab, where the BV loading is applied. This simulated cracking pattern agrees well with the experimental observation. The damage propagation leads to a considerable decrease in the overall stiffness of the slab. As the load increases, the reinforcement yields at the deflection of about 8.6 mm, where the experiment records the yielding point at a deflection of about 6.9 mm. With continued loading, more damage of concrete materials occurs along the slab-column surface on the side of AV loading, and starts to propagate towards the edge where AV loading is applied. Eventually, the slab-column connection on the side of AV loading points

undergoes severe damage under shear loading. The load-deflection curve reaches its peak and the entire slab undergoes a dynamic failure in this load-control test.

3.3 Numerical Validation

The proposed two-scale model is now numerically verified for three different types of structural subassemblages through the comparison with the conventional FE simulations. These three subassemblages are extracted from a prototype 10-story RC building with an interior flat-slab system and a perimeter frame system as shown in Fig. 3.9. The detailed design information of this prototype building can be found in [10, 12] except the slab, which is designed by the author according to ACI design code [2]. These three subassemblages are: 1) four interior spans of the 1st floor (Fig. 3.10a) as marked by red rectangle in Fig. 3.9; 2) a corner span of the 1st floor (Fig. 3.10b) as marked by blue rectangle in Fig. 3.9; 3) a three-story wall panel (Fig. 3.10c) as marked by green rectangle in Fig. 3.9. It is noted that the FE-based numerical validation has been commonly used for various reduced-order numerical models for progressive collapse [11, 88].

For the first two subassemblages, a controlled downward displacement is applied at the center and corner columns, respectively, to investigate the structural behavior under the scenario of column loss [12, 88]. For the wall panel, a horizontal displacement is applied to investigate its in-plane shear behavior. The simulations use the stress-strain relationships of concrete and steel reinforcement that are shown in Fig. 2.7, with the following model parameters for concrete: $f'_c = 27.6$ MPa, $f'_t = 2.92$ MPa, $E_c = 23.7$ GPa, $\epsilon_{cp} = 0.0019$, $\epsilon_{cu} = 0.0067$, $\epsilon_{tp} = 0.00012$ and $\epsilon_{tu} = 0.00128$, and for steel: $f_{sy} = 414$ MPa, $f_{su} = 621$ MPa, $E_s = 200$ GPa, $\epsilon_{sy} = 0.002$ and $\epsilon_{su} = 0.15$.

Figs. 3.11a-c show the representation of these three structural subassemblages using the two-scale model as well as the conventional FE model. For the first subassemblage, only one quarter of the structure is modeled due to the symmetry. In the conventional

FE simulations, the finite element of concrete has a mesh size of about 80 mm, which represents the crack band width of concrete, and the steel reinforcement is modeled by truss elements. For the present two-scale model, it is noted that cohesive elements are placed in the slabs around the column surface to represent the two sets of PDZs for potential punching shear failure mechanics. Fine-scale FE simulations are first performed for all PDZs, from which the corresponding cohesive properties are calibrated following the procedure described in the previous section except that here only the mean cohesive properties are needed. The behavior of the subassemblages is then simulated by using the calibrated cohesive model.

Figs. 3.12a-c compare the simulated load-deflection curves for the three subassemblages. For the first subassemblage, it can be seen that the load-deflection curve has an elastic portion followed by a hardening portion before reaching the ultimate failure. In the elastic portion, the downward displacement is sustained by the slab through its bending resistance. Once the displacement reaches some critical value, the slab near the center column experiences some level of combined flexural and shear damage. Subsequently, a large part of the slab around the center column undergoes tension and the peripheral part of the slab is under compression, which leads to the hardening branch. Such a membrane action has also been observed in some recent studies on RC slabs under progressive collapse loading [86]. With the increasing applied displacement, the portion of the slab that experiences tension increases and the peripheral compression region becomes smaller. Eventually, the slab reinforcement near the columns sequentially ruptures, which causes the subassemblage to lose its load-carrying capacity.

Different from the first subassemblage, which represents a flat-slab system, the second subassemblage consists of a set of perimeter beams and the downward displacement is applied at the corner column at the junction of the perimeter beams. The subassemblage first exhibits an elastic flexural behavior, and some level of compressive damage

occurs in the top part of the perimeter beams and the slab around the column where the displacement is applied, which causes a slight drop of the load-displacement curve. With the increasing downward displacement, the entire quarter of the slab around the corner column starts to experience significant tension, where the rest part of the slab is still under negative bending. By contrast, in the first subassemblage, the entire slab section is under tension as the center downward displacement is significantly large. Due to this difference, for the current subassemblage the load-deflection curve does not exhibit a hardening portion. The longitudinal reinforcement in the two perimeter beams around the corner column eventually ruptures, which causes the ultimate failure of the subassemblage.

For the wall panel under in-plane shear loading, the bottom-left part of the wall starts to experience some level of tensile cracking. Subsequently, a major diagonal crack propagates from the top-left corner towards the bottom-right corner, and the panel reaches its peak load. With the increasing in-plane displacement, severe shear damage occurs at the bottom part of the wall, which causes a sudden drop in the load capacity. Afterwards, the applied shear displacement is mainly resisted by the vertical wall reinforcement, which eventually ruptures causing the failure of the entire panel.

3.4 Conclusion

The proposed two-scale computational model in Chapter 2 is validated both experimentally and numerically. Several types of RC structural subassemblages are analyzed, which include frame subassemblage, flat-slab system, frame-slab system and wall panels. This series of validation studies shows that the present model is capable of simulating the nonlinear behavior of structural subassemblages during collapse process, especially some key mechanisms involved which include the catenary action and compressive archy effect in beams and the membrane effect in slabs. The two-scale model is shown to be

able to capture the overall energy dissipation of the structure during the failure process, which is essential for simulation of progressive collapse. Meanwhile, the two-scale model can save as much as 98% of the computational cost required by the detailed FE model accord to the validation results of the 2D frame. The demonstrated accuracy and efficiency of the two-scale model indicates its suitability for stochastic simulations of progressive collapse.

Table 3.1: Material properties of concrete and steel for experimental validation.

Validation Case	$f'_c(MPa)$	f_{sy} (MPa)	f_{su} (MPa)	ϵ_{su}
Lew et. al. (2011)[67]	32.0	462	641	0.18
Elstner and Hognestad (1956)[36]	20.3	332	552	0.15
Liu et. al. (2015)[69]	36.4	428	621	0.15
Kanoh and Yoshizaki (1979)[59]	35.3	377	537	0.15
Hawkins etl al (1989) [45]	28.9	472	744	0.14

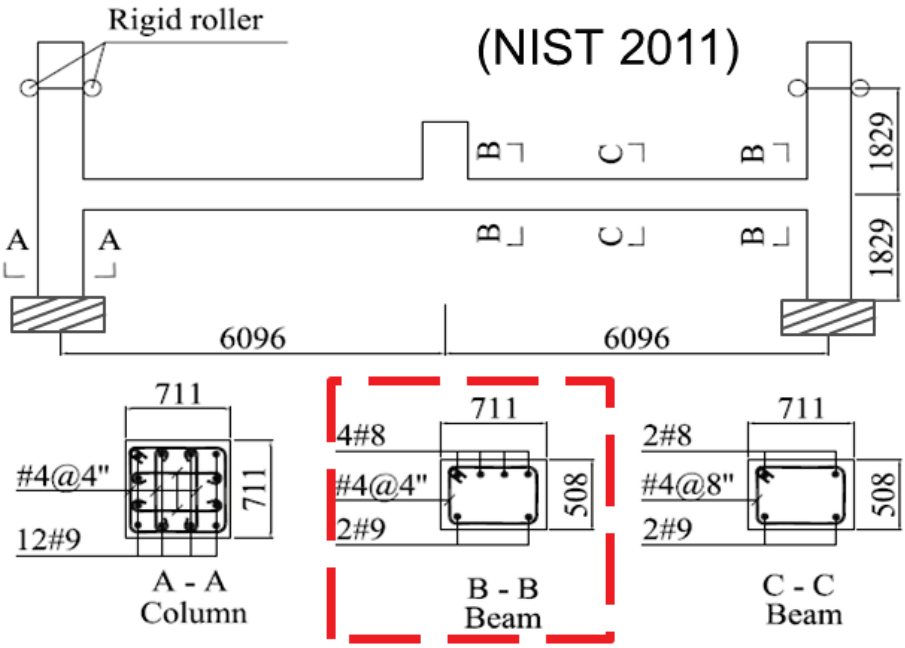

Figure 3.1: Design of the frame subassemblage for pushdown test.

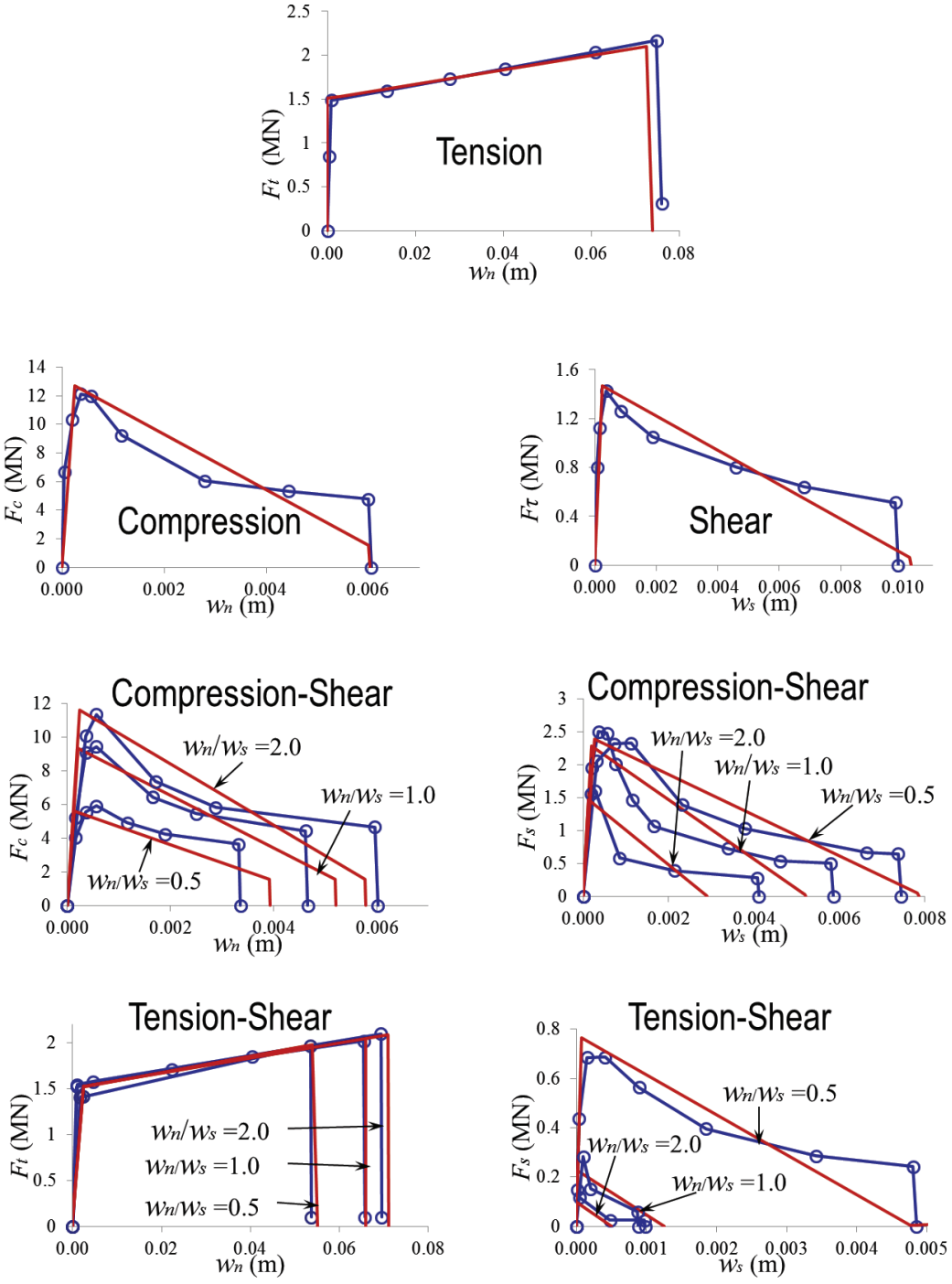

Figure 3.2: Calibration results with fine-scale FE model under single-mode and mixed-mode loadings.

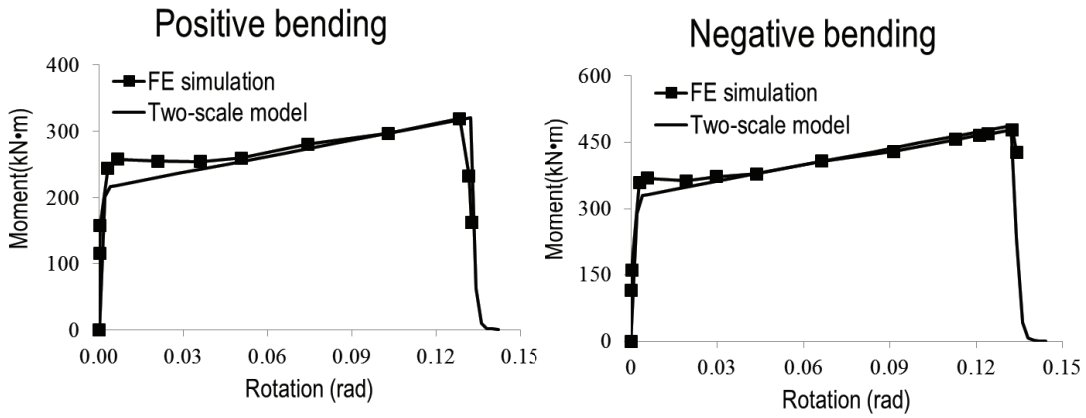

Figure 3.3: Result comparison of the PDZ responses under positive and negative bending.

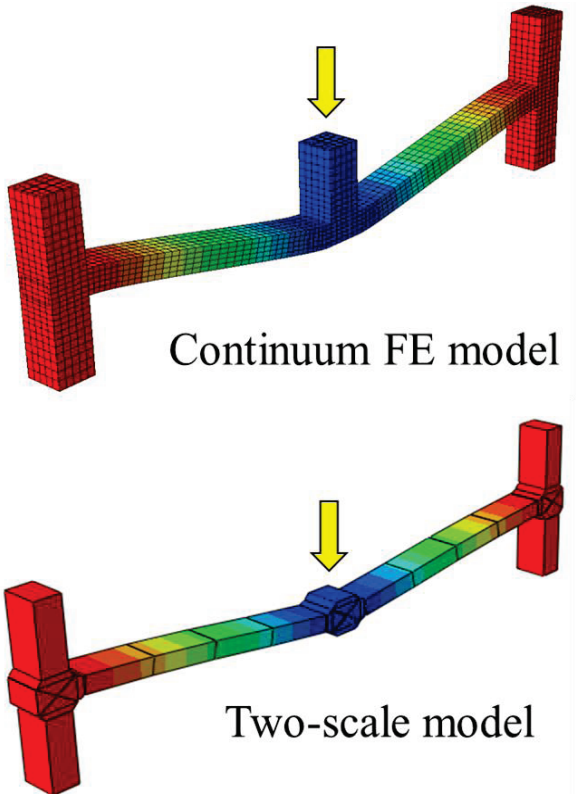

Figure 3.4: Numerical implementation of detailed FE model and two-scale model.

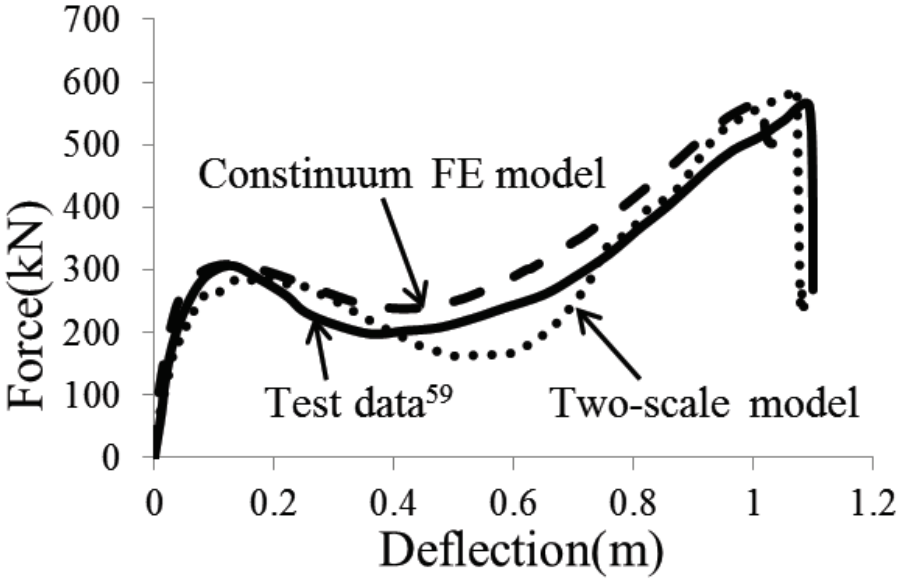

Figure 3.5: Result comparison between two numerical models and experimental testing [67].

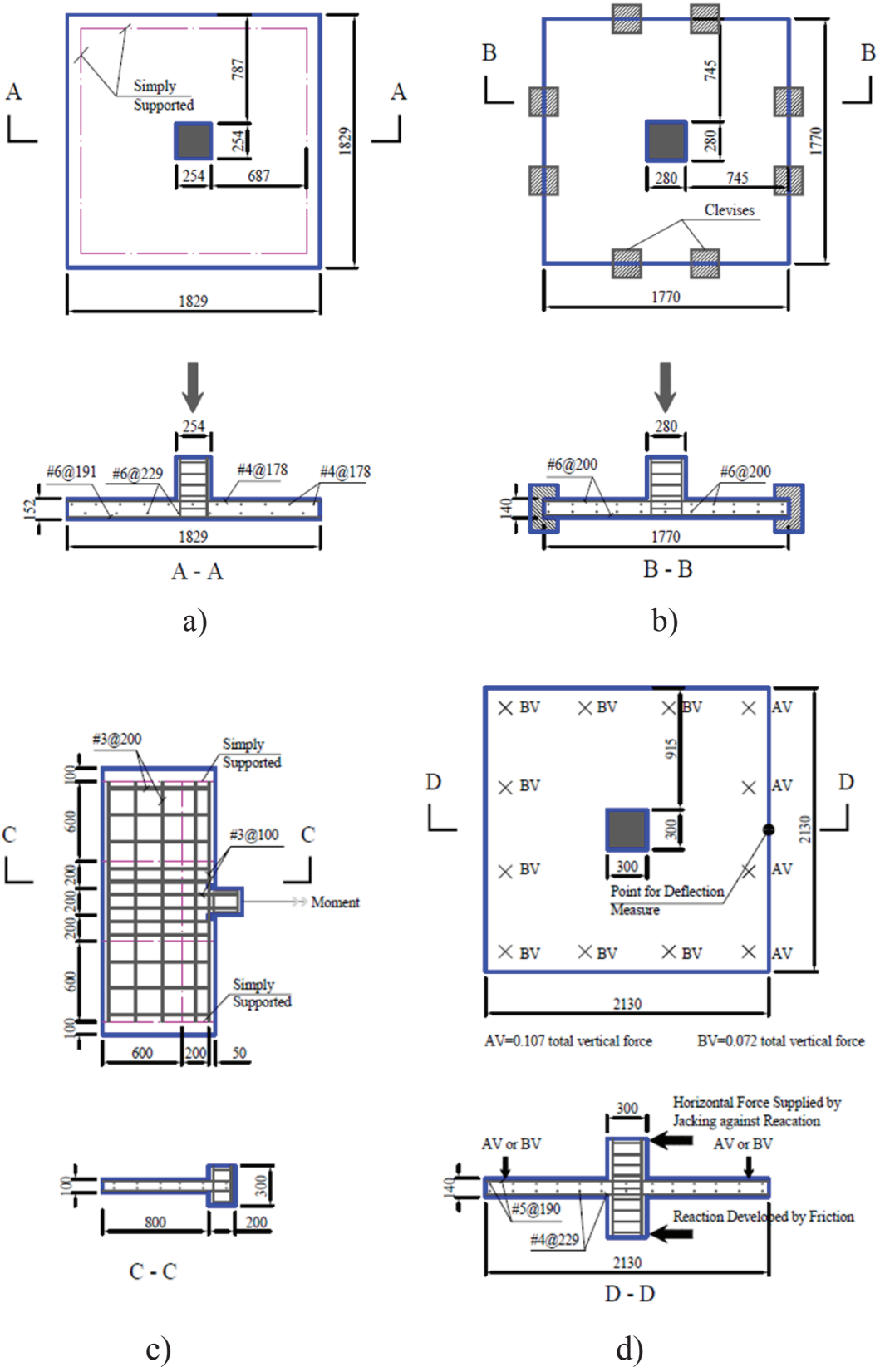

Figure 3.6: Detailed design of four flat-slab systems: a) Elsterner and Honestad (1956); b) Liu etal. (2015); c) Kanoh and Yoshizaki (1979); d) Hawkins etal. (1989).

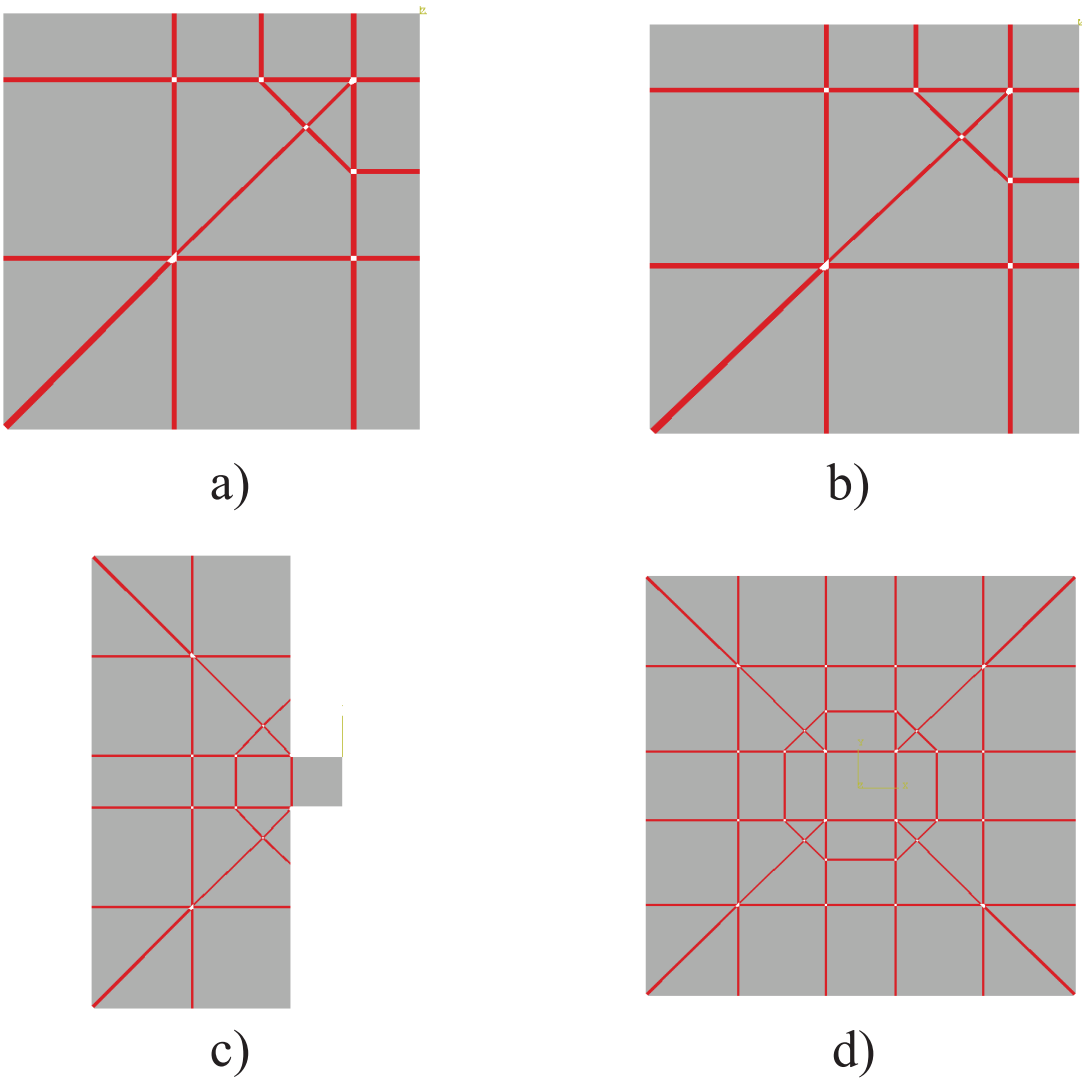

Figure 3.7: Two-scale model of four flat-slab systems: a) Elsterner and Honestad (1956); b) Liu etal. (2015); c) Kanoh and Yoshizaki (1979); d) Hawkins etal. (1989).

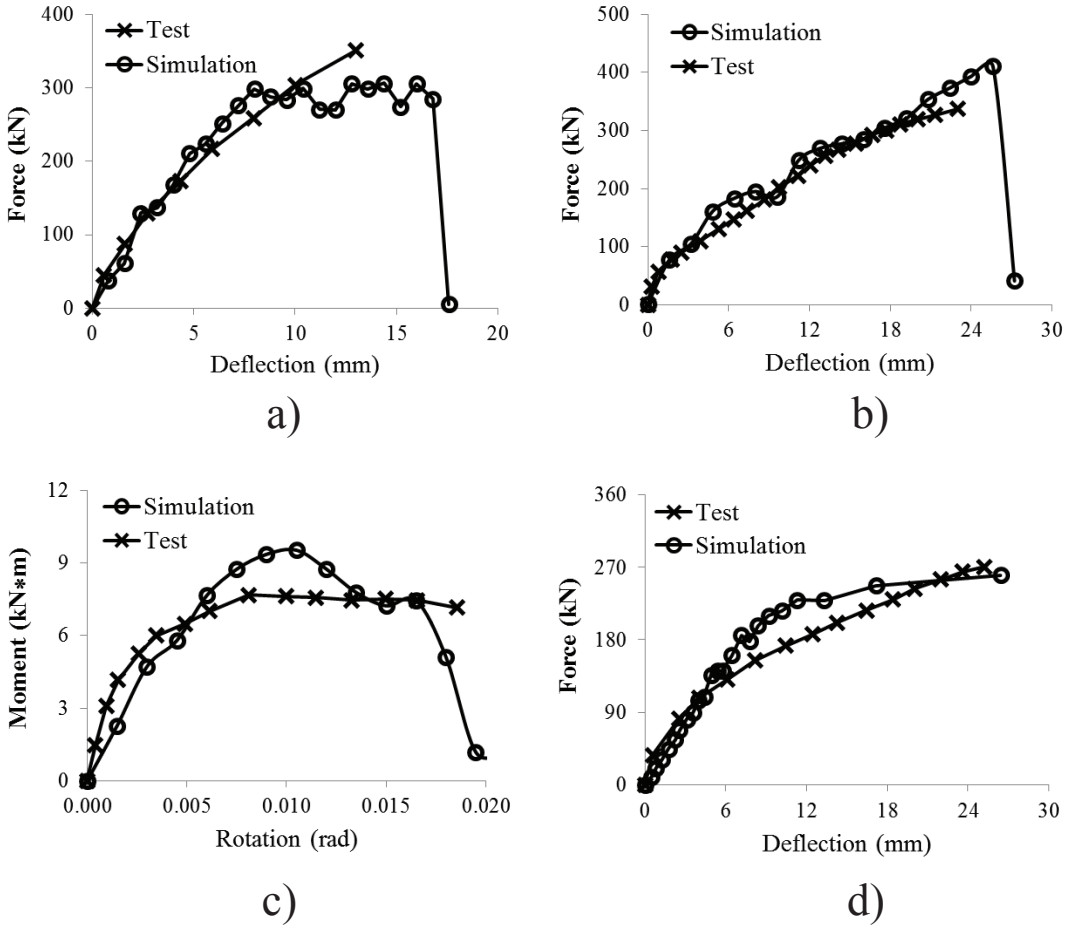

Figure 3.8: Result comparison of four flat-slab systems: a) Elsterner and Honestad (1956); b) Liu etal. (2015); c) Kanoh and Yoshizaki (1979); d) Hawkins etal. (1989).

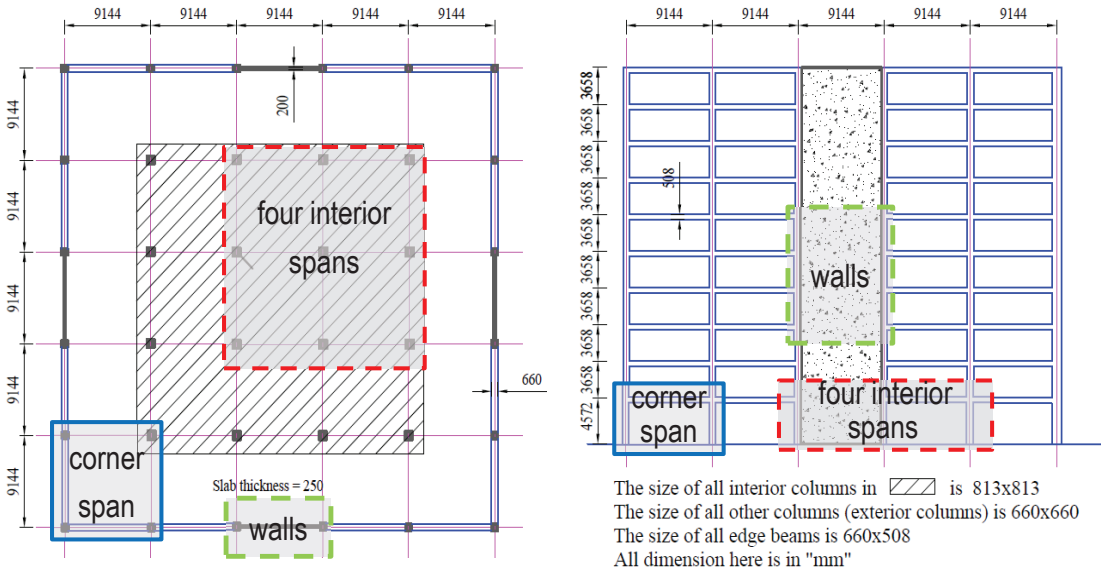

Figure 3.9: Schematic of a 10-story RC building with three subassemblages.

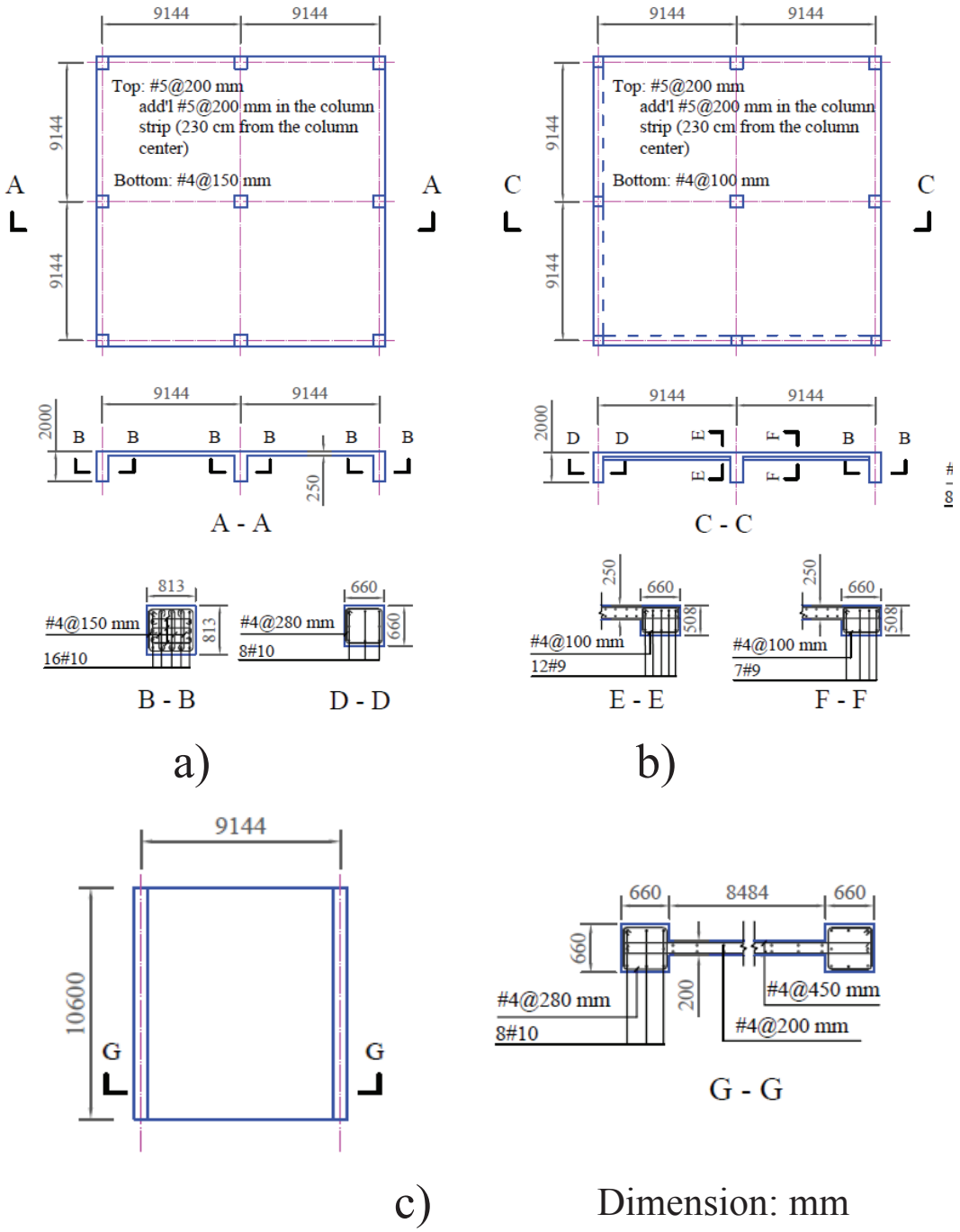

Figure 3.10: Detailed design of three subassemblages: a) interior span; b) exterior span; c) one three-story wall panel).

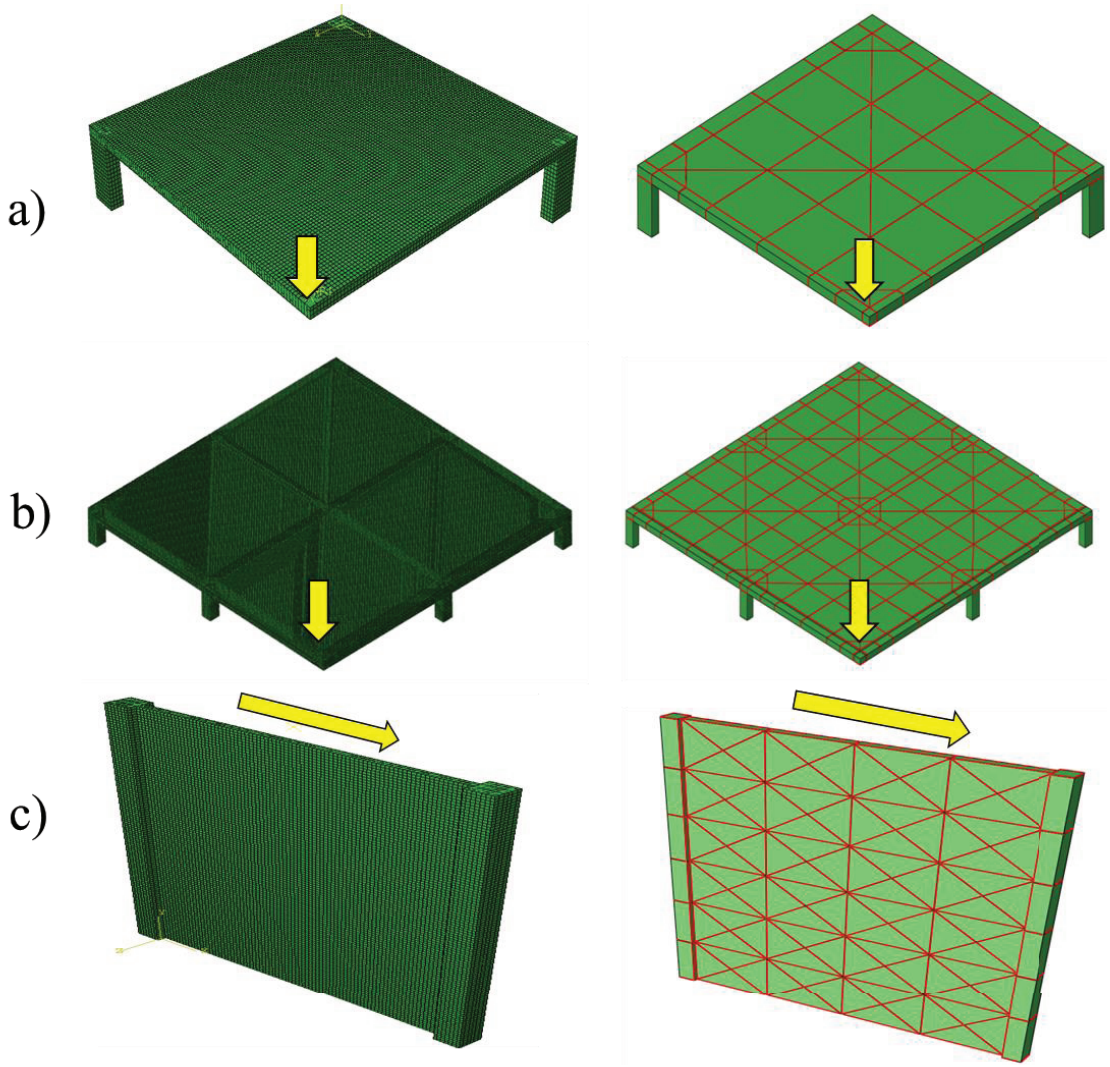

Figure 3.11: Two-scale model of three subassemblages: a) one quarter of four interior spans; b) four corner spans; c) one three-story wall panel).

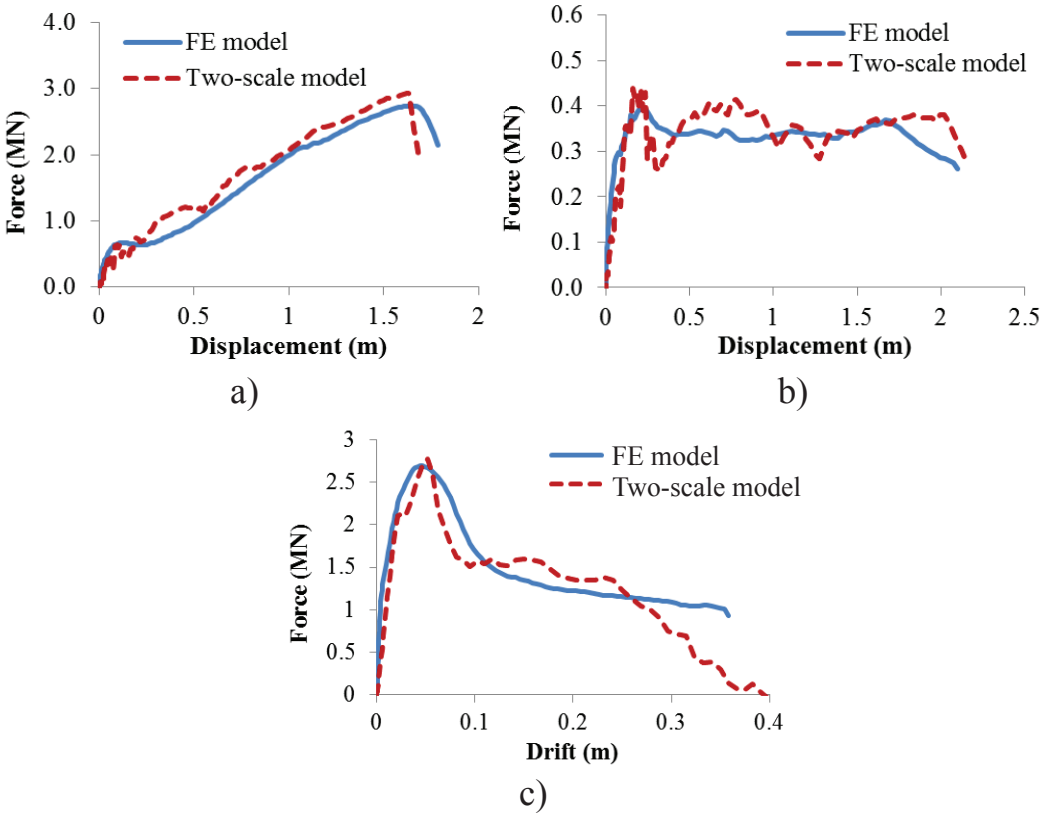

Figure 3.12: Result of three subassemblages: a) one quarter of four interior spans; b) four corner spans; c) one three-story wall panel).

Chapter 4

Risk Assessment of RC Buildings with Two-Scale Model

4.1 Background

Over the past several decades, there has been a continuing interest in understanding the vulnerability of buildings against progressive collapse through computational modeling [16, 11, 52, 47]. In contrast to the wide spread of probabilistic analysis and design methods for civil engineering structures against hazards like earthquakes, hurricanes, and fires, the existing computational modeling of progressive collapse was largely cast into a deterministic framework [105]. However, the importance of probabilistic analysis is evident due to the inherent uncertainties in applied loading and material properties [26, 31, 68, 34, 8, 57]. In view of the severe consequences of the progressive collapse, there is a clear need to evaluate the actual risk of buildings against progressive collapse.

The concept of probabilistic analysis of progressive collapse was first proposed by Ellingwood and Leyendecker [33]. Bennet [21] proposed a simple analytical method for evaluating the collapse risk of buildings, which is limited to structures with a small

number of failure sequences. The general mathematical formulation for risk analysis of progressive collapse can be written as [32, 34]

$$P_f = \sum_H P[C|LD]P[LD|H] \tag{4.1}$$

where $P[C]$ = occurrence probability of a collapse event C, $P[H]$ = occurrence probability of a hazard H, $P[LD|H]$ = probability of local structural damage LD for the given hazard H, and $P[C|LD]$ = occurrence probability of collapse event C for the given local structural damage LD. Among these quantities, $P[H]$ can approximately be estimated from the annual occurrence rate of the hazard [34] and $P[LD|H]$ can conservatively be considered to be equal to unity for the present alternate load path analysis [32]. There is a very limited amount of studies devoted to the computation of $P[C|LD]$ for full-scale buildings. Xu and Ellingwood [111] recently performed a probabilistic analysis of a structural connection under column removal scenario. Park and Kim [83] analyzed the collapse behavior of a 2D steel frame with considering uncertainties in material yield strength and applied loads. So far, there have been no attempts at probabilistic analysis of the overall collapse behavior of 3D RC buildings subjected to local structural damage. The need to develop such a stochastic numerical model, which can be used to evaluate the collapse risk, motivates the present study.

In this chapter, we apply the proposed two-scale computational model to the probabilistic analysis of RC buildings by incorporating the uncertainties in both gravity loading and material properties. As a demonstration, this probabilistic model is applied to assess the collapse risks of a 2D 30-story RC frame structure and a 3D 10-story RC structure under various initial damage scenarios. In addition to the probabilistic analysis, the existing deterministic analysis method which uses the mean material properties and gravity loading, is also carried out to investigate the implication of the deterministic method on reliability of buildings against progressive collapse.

4.2 Stochastic Simulation Framework

In this study, a stochastic simulation framework shown in Fig. 4.1 is established to facilitate the following probabilistic analysis of progressive collapse of buildings for given initial local damage scenarios. In this stochastic simulation framework, all random cohesive properties and external loads are sampled by using the Latin Hypercube Sampling (LHS) technique through Design Analysis Kit for Optimization and Terascale Applications (DAKOTA) [4], which starts each collapse evaluation as shown in Fig. 4.1. For a specific sample of all random resistance and loading variables, ABAQUS [1], a commercial FE software is used to evaluate the collapse process and extent for a given local damage scenario. In this framework, a Python interface in charge of pre- and post-processing of each collapse evaluation is developed to connect two existing software, DAKOTA [4] and ABAQUS [1] to form an uncertainty quantification loop. In pre-processing step, this user-developed Python interface will gather the sample information from DAKOTA and prepare the input file for the collapse evaluation with ABAQUS. During post-processing step, this Python interface is used to collect analysis results (i.e. collapse extent information) from ABAQUS output file and then return these information to DAKOTA.

The LHS method utilized in this study is a sampling technique developed by [72] to generate samples of random variables from a multidimensional distribution. The LHS method adopts a so-called stratified sample approach, which decreases the number of samples required by classical Monte-Carlo Sampling (MCS) method to reach an accurate random distribution as indicated by Fig. 4.2 on a two-dimensional space with the number of sample equal to 10. In this figure, the LHS method has one sample in each strip of the design space with equal probability for every random variable while the MCS method cannot ensure this kind of uniform distribution of samples unless a large number of samples are made. Therefore, compared to the MCS method, the LHS method can

significantly accelerate the convergence of the probabilistic analysis.

During the collapse evaluation, the cohesive element will be deleted once it is totally damaged. Therefore, during the collapse, structural components could be fragmented, and the debris could impact on the other intact structural components. In the present simulations, the impact is handled by the default contact algorithm in ABAQUS, where the contact behavior is prescribed in both normal and tangential directions. In the normal direction, the contact pressure-overclosure relationship is assumed to follow the so-called hard contact in ABAQUS [1], which would minimize the inter-penetration. In the tangential direction, we adopt a penalty model with a friction coefficient of 0.3, which allows a linear friction force-slip relationship during the stick state. Due to random material properties and gravity loads, the behavior of fragments will be highly stochastic, which leads to the randomness in energy losses during the impact.

4.3 Risk Assessment of a 2D 30-Story RC Frame Structure

We now apply the proposed two-scale model to perform stochastic simulations of a 2D 30-story RC frame under some column removal scenarios. The frame considered here is very similar to the prototype RC building recently studied by NIST [67]. The details of the frame are shown in Fig. 4.3. The beam span is 6 m, and the column height is 4 m except that the 1st story columns have a height of 4.5 m. In this study, we perform two types of simulations: 1) stochastic simulation, where we consider uncertainties in both material properties and gravity loads; and 2) mean-centered deterministic simulation, where we use the mean material properties and a set of factored loads suggested by the Unified Facilities Criteria (UFC) [29, 111].

4.3.1 Collapse Simulation

Using the cohesive element model for this frame, we have eight different types of PDZs (three for columns, two for beams, and three for joint panel zones), for which the constitutive behavior of the corresponding cohesive elements need to be calibrated based on the procedure discussed in Chapter 2. The constitutive properties of concrete and reinforcement and their associated probability distributions are listed in Table 4.1. As mentioned earlier, the probability distributions of parameters for bond strength follows [27]. Note that the coefficient of variation (CoV) for compressive and tensile strengths of concrete listed here is exclusively for one finite element, which is expected to be considerably higher than the CoV measured in the conventional laboratory tests on concrete specimens [17, 40].

Based on the deterministic fine-scale simulations, we find the same set of the mode mixity parameters, i.e. α_c=0.54, β_c=0.30 and γ_c=2.00 for coupled compression-shear loading and α_t=2.25, β_t=1.00 and γ_t=2.00 for coupled tension-shear loading, can be used for all eight types of PDZs. The LHS technique is used for the fine-scale stochastic simulations of the effective concrete sections, and the Monte Carlo simulation is used for determining the random cohesive properties of longitudinal reinforcement. It is found that the probability distributions of all the cohesive properties can be approximated to be Gaussian. As a demonstration, Fig. 4.4 plots on the Gaussian distribution paper the probability distributions of cohesive properties for the PDZ at the beam end. Table 4.2 presents the mean and CoV of the cohesive properties for the eight types of PDZs. Meanwhile, we also determine the correlations between the random cohesive properties for each PDZ, measured by the correlation coefficient equation below:

$$Correl(X,Y) = \frac{\sum(x-\bar{x})(y-\bar{y})}{\sqrt{\sum(x-\bar{x})^2 \sum(y-\bar{y})^2}} \tag{4.2}$$

As an example, Table 4.3 presents the correlation coefficients of all the random cohesive

properties of the PDZ at the beam end.

Besides the uncertainties associated with the material properties, we also include in the simulation the load randomness. Following [111], we consider that the dead load has a normal distribution with the mean value of $1.05DL$ and a CoV of 0.10 and that the live load has a Gumbel distribution with the mean value of $0.3LL$ and a CoV of 0.60, where DL = nominal dead load =19.21 kN/m and LL = nominal live load = 7.18 kN/m for beams and for columns and joint panels DL is equal to the self-weight and no live load is assigned [67]. The self-weight of the building is calculated from the densities of concrete and steel, i.e. 2400 kg/m^3 and 7850 kg/m^3, respectively. In the simulations, the gravity loads are gradually applied to the frame using a smooth step function for 4 seconds, which ensures that the forces in the frames are full stabilized. As a conventional approach for progressive collapse analysis, the local structural damage is simulated by sudden column removal. In this study, we consider removal of a perimeter column on the 1st, 8th, 16th, 26th and 29th story, one story at a time (Fig. 4.5), which represents in total five column removal scenarios. In all simulations, columns are removed in 0.05 second, which is similar to the procedure used in a recent numerical study of progressive collapse of RC frames [11]. All the simulations are performed using the commercial software ABAQUS/Explicit [1] with a damping ratio of 5% to include the damping effects of RC components.

For the stochastic modeling of the entire frame, we assume that 1) each random cohesive property is fully correlated by their mean ratios among all the beams within each five stories (i.e., 1st- 5th stories, 6th-10th stories, and so on); and 2) along each column line, each random cohesive property is fully correlated by their mean ratios among all the columns and joint panels within five stories. For each PDZ individual cohesive properties are partially correlated, e.g. Table 4.3. Similarly, we assume that the dead and live loads within each five stories are fully correlated respectively by

their mean ratio though the individual dead and live loads are independent of each other. All the random variables are sampled by using the LHS technique through the DAKOTA [4], where the individual partially correlated random cohesive properties are first transformed to independent ones by Nataf's model [44]. The simulation is terminated once the calculated probabilities of each collapse extent converge within a relative error of 5%.

As a comparative analysis, we also perform deterministic simulations for the above-mentioned five local damage scenarios. Following the UFC guidelines [29], we use the gravity load combination $1.2DL + 0.5LL$, and the mean cohesive properties are used in the simulations. The simulation procedure is the same as that used for the stochastic simulations.

4.3.2 Results and Discussion

To assess the severity of the propagation of local structural damage, we can generally define four levels of collapse extent as shown in Fig. 4.6: 1) intact: the crush front does not propagate, 2) local collapse: the crush front only propagates through the area where the columns are removed and it is arrested within one story, 3) partial collapse: the crush front propagates further than the local region defined in 2) but the damage does not propagate laterally into the other adjacent bays, and 4) total collapse: the crush front propagates into the entire structure.

Table 4.4 shows the calculated probabilities of the occurrence of the four levels of collapse extent for all five column removal scenarios. It is found that the probability of being intact decreases from 99.14% to 63.80% as we lower the column removal location (i.e. from 29th story to 1st story). This can be explained by a simple energetic analysis: in order for the crush front to propagate, we must satisfy the condition $mgh \geq \Delta W$, where m = mass of the upper falling part, h = story height, ΔW = total energy

dissipation capacity due to the damage of all the beams in the upper falling part. As a simplified analysis, we may approximately consider $\Delta W = n\Delta W_b$, where n = number of beams in the upper falling part, and W_b = average energy dissipation due to damage of each beam. However, mass m can be simply calculated as $m = nm_b + (n-1)m_c$, where m_b, m_c = masses of individual beam and column, respectively. It can be easily shown that $m(n_1)/m(n_2) > n_1/n_2$ (n_1, n_2 are the numbers of beams in the upper falling part for two column removal scenarios), i.e. the increase in mass m with the size of the falling mass is greater than the increase in the total energy dissipation capacity. This implies that as, we remove columns on a lower story, there is a higher chance for collapse to initiate.

This aforementioned explanation applies to the column removal on most stories except the roof story. According to [47, 89], under the the column-removal scenario at roof story, the building is more vulnerable to progressive collapse than removing the column on other stories because of the diminishing of the Vierendeel frame action. To investigate this Vierendeel action's effect on collapse resistance of frame structures, we perform the deterministic analysis of this 2D frame subjected to one perimeter-column removal at the roof story, which yields a total collapse extent. According to Table 4.4, the deterministic analysis predicts that the building would be intact after removing one perimeter column on the 26th and 29th stories, respectively. These deterministic analysis results demonstrate that the aforementioned mechanism related with mass and energy dissipation capacity and the Vierendeel action are two competing mechanisms. When it comes to the frame structure subjected to initial damage at roof story, the the Vierendeel action fully diminishes, which overweights the gain of resistance due to the aforementioned mechanism at roof story. However, if we lower down the location of column removal on other stories, the increase in collapse resistance due to the Vierendeel action is not significant and the previously discussed mass-energy dissipation mechanism

dominates the trend of collapse extents for the deterministic analysis.

In the meantime, it is interesting to note that the entire frame could possibly suffer a total collapse even though we just remove a perimeter column. Based on the simulation, it is observed that the total collapse is caused by the following mechanism: the initial column removal first leads to a downward propagation of the crush front (i.e. a crush-down mode). As the crush front finally reaches the ground, the ground exerts a large rebound force on the falling mass and causes the crush front to move upwards (i.e. a crush-up mode). During the crush-down and crush-up phases, the debris can severely damage the side columns at the lower stories, which induces a lateral propagation of the crush front and destroy the remaining five bays in a crush-up mode. The same mechanism was also reported based on a recently developed discrete element model of progressive collapse of RC frames [75]. Furthermore, it is observed that the probability of total collapse first increases and then decreases as the column is removed on a higher story. To explain this observation, we note that there are two competing mechanisms that govern the occurrence of the total collapse: as we remove columns on a higher story, the momentum of the falling part that hits the ground gets larger, which causes a larger impact force of the debris on the side intact columns and therefore leads to a higher chance of lateral propagation of the crush front. Nevertheless, at the same time, the duration of the crush-down phase becomes longer and therefore the debris has sufficient time to interact and to be pushed away from the remaining intact part of the frame. Therefore, among the five column removal cases considered here, the highest probability of the total collapse occurs when the column is removed on the 8th story.

It is also worthwhile to mention that the present simulations do not yield local collapse extent for all five column removal scenarios. From the simulations, it is seen that, as the collapse initiates, the upper falling mass would impact the beam at the lower story. Such a beam impact scenario has been studied by various analytical methods

[56, 108]. It has been shown that the dynamic impact loading can be approximately calculated by considering an idealized single-degree-of-freedom system [20, 56]: $F_d = mg\left(1+\sqrt{1+2Ch/mg}\right)$, where C = system stiffness. As a rough estimation, we may choose $C = 48EI/l_b^3$ by considering the beam is simply supported and impacted at the mid-span and $C = 192EI/l_b^3$ for a fixed end beam impacted at the mid-span [56], where E = Young's modulus, I = moment of inertia, and l_b = beam span. It can then be demonstrated that for all the column removal scenarios considered in this study the dynamic impact force exerted on the beam by the upper falling mass induces a moment that is much larger than the flexural capacity of the beam and therefore the probability that the beam on the lower story can resist the crush front is extremely low. The similar conclusion can be drawn by a recently proposed energy analysis of beam impact, which showed that the percentage of the energy imparted to the lower intact beam by the upper falling mass can vary from approximately 25% to 50% and from 50% to 70% of the initial kinetic energy of the falling mass for fully plastic and fully rigid impact scenarios, respectively and therefore a large dynamic impact force is expected [108].

Finally, we compare the present probabilistic analysis with the widely adopted deterministic analysis. The prediction of the collapse extent by the deterministic analysis is also listed in Table 4.4. It can be seen that the deterministic simulation is able to predict the occurrences of either total or partial collapse for the cases of column removal on the 1st, 8th and 16th story, which according to the probability analysis have the occurrence probabilities of 20.20%, 16.71% and 6.71%, respectively. For the case of column removal on the 26th story, the deterministic analysis predicts that the frame is intact while the stochastic simulation predicts a overall probability of partial and total collapses of 6.60%. According to [32], the tolerable collapse risk level for a given local damage scenario is on the order of 1%. Therefore, for this simulation, we can conclude

that the mean-centered deterministic analysis can be used for assessing the vulnerability of the frame against collapse for most local damage scenarios. Nevertheless, it may not always be able to predict the collapse extent of a low occurrence probability, which could still be of interest for design.

4.4 Risk Assessment of a 3D 10-Story RC Building with a Flat-Slab System

The present two-scale model is now used to investigate the collapse behavior of the aforementioned prototype 10-story RC building shown in Fig. 4.7 [10, 12]. The two-scale model of this prototype building is presented in Fig. 4.8 with cohesive element allocated at the place of PDZs, potentially formed during the collapse. In this study, we perform stochastic simulations for different local damage scenarios with considering random material properties and a combination of random gravity loads $1.05DL+0.3LL$ [111] (DL = nominal dead load including the self-weight and superimposed dead load and LL = nominal live load), and the occurrence probabilities of different collapse extents are calculated. Similar to the foregoing analysis of 2D frame, the conventional mean-centered deterministic simulations, which use the mean material properties and a combination of mean gravity loads $1.2DL+0.5LL$, are also performed. In both simulations, the initial local structural damage is represented by a sudden column/wall removal, which is a common procedure for the alternate load path analysis of progressive collapse [11, 6, 88]. Here we consider eight different column/wall-removal cases as shown in Fig. 4.7, which include the removal of two adjacent corner columns and the removal of a wall panel on the 1st, 5th, 9th and 10th story, respectively. The building is assumed to have a 5% damping ratio.

In this simulation, the gravity loads are first gradually applied to the entire building

using a smooth-step function in 1 second, which is sufficient to stabilize the force distribution in the building. The columns are then removed in 0.05 seconds, which is similar to the procedure used in the recent numerical simulations of progressive collapse of RC structures [11].

4.4.1 Material Properties and External Loading

Tables 4.1 and 4.5 show the material properties of concrete and steel reinforcement and the superimposed gravity loads with their probability distributions, respectively. The random constitutive properties of cohesive elements representing the PDZs are determined following the aforementioned calibration procedure. It is found that the probability distribution functions of all cohesive properties can be approximated by the Gaussian distribution. As a demonstration, Fig. 4.9 and Fig. 4.10 present on the Gaussian paper the simulated probability distributions of the cohesive properties of the PDZs at the end span of the beam and the interior column on the first story, respectively. The calculated CoV and mean values of all the random variables are listed in Table 4.8. Meanwhile, for each PDZ, the individual random cohesive properties are found to be partially correlated and the corresponding coefficients of correlation are determined through the fine-scale stochastic simulations as shown in Table 4.6 and Table 4.7, which are partial correlation matrices for the PDZs at the end of the beam and the interior column on the 1st story, respectively.

For the stochastic modeling of the entire building, the following assumptions are made regarding the spatial statistical correlation of each cohesive property of the PDZs: 1) within each story, the respective random cohesive properties are fully correlated by their mean ratios among all the PDZs in beams and slabs; 2) the respective random cohesive properties are fully correlated by their mean ratios among all the PDZs in the perimeter columns within two stories; 3) the respective random cohesive properties are

fully correlated by their mean ratios among all the PDZs in the interior columns within a quarter slab and along two-story height; 4) the respective random cohesive properties are fully correlated by their mean ratios among all the PDZs in a single wall panel of two story height. Note that for each PDZ, various random cohesive properties are partially correlated as determined by the fine-scale stochastic simulations. Furthermore, within a quarter of the floor, the dead and live loads are fully correlated respectively by their mean ratio though the individual dead and live loads are independent of each other. In the stochastic simulations, all the partially correlated random cohesive properties are firstly transformed to independent random variables through Nataf's transformation [44], and are then sampled by the LHS technique for the subsequent simulation of progressive collapse.

4.4.2 Results and Discussion of Deterministic Calculations

We first discuss the results of the deterministic calculations. It is found that for column removal and wall removal at the 1st, 5th, and 9th stories the building would suffer a total collapse, whereas the column removal and the wall removal at the 10th story the building would remain intact. To better understand the collapse resistance of the building for different initial damage cases, we scale the UFC gravity load combination for these four column removal cases at which the collapse initiates, i.e. $w = \alpha_l(1.2DL+0.5LL)$, where w = applied gravity load and α_l = collapse load factor. Table 4.9 shows the calculated values of α_l for the four column removal cases. As seen, the collapse resistance increases as we remove columns at a higher story. This trend is opposite to some recent studies on the effect of the location of column removal on the collapse vulnerability of RC frame buildings, which predicted that the building would not suffer more damage if columns are removed at a lower story [47, 89]. There are two main reasons for this difference, which are described as follows:

1) One of the primary collapse resisting mechanisms of RC frame structures is the Vierendeel frame action. It is clear that as we remove columns at a high story, the Vierendeel frame action diminishes, which leads to a lower collapse resistance. In contrast to the conventional RC frame structures, the present building consists of a frame-wall structure on its perimeter and a flat-slab system with a 250 mm thick slab. The present simulations show that after column removal on average about 75% of the addition gravity load is redistributed to the slab panels above the column removal location, and the remaining 25% is redistributed to the perimeter beams. Therefore, it is expected that the effect of Vierendeel frame action on the overall collapse resistance of the present building would not be as much as that of a conventional frame structure.

2) The other aspect that needs to be considered is the effect of the reduced roof loads. To evaluate this effect, we re-run the simulation by considering that the roof carries the same nominal gravity loads as the other floors do. Table 4.9 shows the computed α_l values for the case of full roof loads. It is seen that the collapse load exhibits a significant drop for column removal at the roof due to the loss of the Vierendeel frame action, which is consistent with the findings of some recent studies [47, 89]. By comparing the simulations for cases with full and reduced roof loads, it is observed that the reduction of roof loads has a more pronounced effect on the overall collapse resistance as we remove columns at higher stories. It is clear that, in comparison with the Vierendeel frame action, the reduction in roof loads has an opposite effect on the overall collapse resistance. For column removal at a higher story, the Vierendeel frame action diminishes, which indicates a reduction in overall resistance. On the other hand, the reduction in roof loads leads to lower applied gravity loads. For the building considered here, it shows that the reduction in roof loads has a more pronounced effect than the diminishing Vierendeel frame action. This is also partly due to the fact that a large portion of gravity load is redistributed to the flat slab. This explains the observed

pattern of the overall collapse load factor, which increases for column removal at higher stories.

4.4.3 Results and Discussion of Stochastic Calculations

For the stochastic simulations, we define three levels of collapse extent as shown in Fig. 4.11: 1) intact: there is no propagation of initial local damage, 2) partial collapse: the initial damage spreads into other parts of the building but the building still stands, and 3) total collapse: the entire building collapses. For each column removal scenario, the occurrence probabilities of these three collapse extents p_i $(i = 1, 2, 3)$ are calculated as $p_i = n_{ci}/n_t$, where n_t = total number of realizations in the stochastic simulation for a given initial damage scenario and n_{ci} = number of collapse extent i observed in n_t number of realizations. Table 4.10 shows the results of the calculated occurrence probabilities of the three levels of collapse extent.

The typical failure mechanism that is observed in the simulation can be described as follows: after the columns are suddenly removed, the upper part of the building starts to deform downwards and the load starts to be laterally redistributed to adjacent columns through the slab panels and perimeter beams. During the load redistribution, the PDZs of the perimeter beams start to experience significant flexural damage and the PDZs of the slabs around the adjacent columns experience combined flexural and shear damage. Subsequently more failure events occur around the intact columns in the slabs, which causes the entire floor to lose its structural integrity. It is observed that, once the entire floor falls onto the lower story, the slab on the lower story is unable to resist the upper falling slab due to the large impact force. This leads to an accelerated downward propagation of the structural damage, which is often referred to as the crush-down mode. It is noted that, during the crush-down phase, the stories above the initial falling slab may have already experienced a considerable amount of

damage. After several stories are damaged by the upper falling part, the columns on the lower stories fail due to the loss of lateral restraints as well as the debris impact. The stories above the initial collapsing slab hit the ground and experience a large rebound force, which cause the damage to propagate upward through the stories, which is often referred to as the crush-up phase. It is noted that sometimes the crush-up phase may not be discernible if the structure above the initial collapsing story has already been severely damaged.

It is worthwhile to comment on the partial collapse pattern shown in Fig. 4.11b. This is a rare event with a occurrence rate of 6%, where the sampled resistance of the second story is significantly lower than that of other stories and the columns on the first two stories have a relatively high resistance. It observed that during the load redistribution process the shear-dominant damage starts to occur in the vicinity of the column removal location, and progressively spread to the entire second floor. During the damage propagation, the slab panel near the column removal location starts to detach from the column face due to punching shear failure, and with an increasing deformation more shear failures occur around the column surfaces as well as the interface between columns and perimeter beams. Eventually, the entire floor falls onto the ground, and the large rebound force causes further damage to the perimeter beams and slab panels. It should be noted that Fig. 4.11b shows the final damage pattern after the floor impact the ground. Simulation indicates that the perimeter beams and slab panels fall together and it is the rebound force that damages the perimeter beams. Meanwhile, during the collapse process a limited amount of debris impact on the columns and for some sampled column resistances doubling the effective length of the columns is not sufficient to cause them to fail.

We now compare the results of the stochastic simulations with those obtained by the conventional deterministic simulations (Table 4.10). The deterministic calculations

show that the collapse load factors α_l for column removal at the 1st and 5th stories do not differ much. By contrast, the stochastic simulations show a considerable increase in the collapse probability. This can be attributed to the fact that the number of possible failure paths for column removal at the 1st story that can lead to collapse is much more than that for column removal at the 5th story. Since the cohesive resistances of beams and slabs of each floor are statistically independent, the increasing number of failure paths indicates a more likelihood of collapse initiation. It should be emphasized that such an effect can only be derived from probabilistic analysis. To a certain extent, this is analogous to the weakest link statistical model for material strength [14], which predicts that a large-size specimen would have a lower strength compared to a small-size specimen due to the existence of more possible weak material elements.

The comparison between the deterministic and stochastic simulations also reveals the implication of the UFC load factors in terms of the collapse risk of the building. As mentioned earlier, the occurrence probability of a local damage scenario due to hazards is on the order of 10^{-4} and the total collapse probability of a general building should be limited to the order of 10^{-6}, therefore the tolerable collapse probability for a given local damage scenario should be on the order of 0.01. Based on Table 4.10, it is clear that the deterministic calculations with the load factors suggested by UFC are able to predict a collapse extent with an actual occurrence probability around 7.67%, which is sufficient for most buildings. In the meantime, we also observe that the deterministic analysis fails to predict a collapse event of an occurrence probability of 0.5%, which could still be of interest to some sensitive buildings. In such a case, a probabilistic analysis would be required for assessing the vulnerability of building against progressive collapse.

4.5 Conclusion

Based on the two-scale model presented in Chapter 2, a probabilistic analysis procedure is developed to calculate the collapse risk of RC buildings for given initial structural damage. This analysis procedure is applied to the risk assessment of two prototype RC buildings, which include a 2D frame building and a 3D building with a flat-slab system and shearwalls. It is shown that the model can successfully capture the various collapse mechanisms, including crush-down, crush-up and lateral propagation of the crush-front..

With considering uncertainties in both material properties and gravity loads, we can evaluate the probabilities of the occurrence of various collapse extents of RC buildings subjected to a given initial damage scenario. By comparing the present stochastic analysis with the existing mean-centered deterministic analysis, it is found that for both the aforementioned 2D and 3D RC buildings the deterministic method can be generally used to assess the structural vulnerability against a reasonably low collapse probability ($\approx 5.00\%$). Such a collapse risk is generally acceptable for most conventional buildings. Nevertheless, for some sensitive RC buildings, where a lower collapse risk is required, probabilistic analysis becomes necessary and the present model provides an efficient means for such an analysis.

The probabilistic analysis takes into account different possible failure paths due to the randomness of material properties and applied gravity loads, whereas the deterministic calculation only captures the dominant failure path that corresponds to the mean behavior. This causes some differences in the prediction of the effect of initial damage location on the overall collapse resistance for these two types of analysis. From the analysis results of the 2D building, we can see that there are two competing mechanisms, the relation between mass and energy dissipation capacity per story and the Vierendeel effect in frame structure. For column removal at roof, the diminishing of Vierendeel effect takes control and makes the building more vulnerable to collapse compared to

column removals on stories immediate below the roof while for column removals on stories far away from the roof the first mechanism governs the collapse resistance pattern with an enhanced collapse resistance for a higher column-removal location. For the 3D prototype building, due to the randomness in material properties and gravity loading of each story, it is more likely to have more possible failure sequences for the column/wall removal on a lower story. More possible failure sequences together with the reduced roof load outperforms the weakened Vierendeel effect in a building with a flat-slab system, which leads to a monotonically increasing collapse risk for a lower column-removal location.

Table 4.1: Material properties for stochastic simulations.

	Concrete					
Parameter	f'_c	f'_t	ϵ_{cp}	ϵ_{tp}	ϵ_{cu}	ϵ_{tu}
Distr. type	Gaussian	Gaussian	Deterministic			
Mean	27.6	2.92	1.9e-3	1.2e-4	0.67e-3	1.28e-3
CoV	0.25	0.25	-	-	-	-
	Reinforcement					
Parameter	f_{sy}	f_{su}	ϵ_{sy}		ϵ_{su}	
Distr. type	Gaussian	Gaussian	Deterministic			
Mean	414	621	0.002		0.15	
CoV	0.05	0.05	-		-	

f'_c, f'_t, f_{sy} and f_{su} are in MPa, and CoV stands for coefficient of variation.

Table 4.2: Probability distribution for all RC sections.

Parameter		G_{fc}	σ_{cp}	$G_{f\tau}$	$\sigma_{\tau p}$	G_{ft}	σ_{tp}	G_{fs}	σ_{su}
Beam	mean	0.0657	27.39	0.0232	4.085	1.17E-04	2.405	37.76	588.0
End	CoV	4.05%	3.72%	6.09%	4.41%	12.06%	3.56%	12.89%	6.37%
Beam	mean	0.0612	26.72	0.0222	4.060	1.17E-04	2.401	37.76	588.0
Midspan	CoV	4.95%	3.76%	6.43%	4.25%	12.77%	3.93%	12.89%	6.37%
Column	mean	0.1467	28.69	0.0425	4.179	1.36E-04	2.326	45.31	589.2
F21-F30	CoV	6.91%	2.63%	5.39%	3.17%	13.68%	3.18%	10.99%	6.66%
Column	mean	0.1606	28.48	0.0483	4.332	1.34E-04	2.247	49.25	589.7
F11-F20	CoV	3.70%	2.21%	5.38%	2.28%	11.89%	2.72%	10.48%	6.62%
Column	mean	0.1968	29.09	0.0628	4.421	1.50E-04	2.278	53.49	592.2
F1-F10	CoV	7.98%	1.92%	5.31%	2.11%	10.03%	2.60%	9.60%	6.17%
Joint	mean	0.1549	30.19	0.3259	8.414	1.41E-04	2.864	52.34	589.2
F21-F30	CoV	6.91%	2.63%	5.39%	3.17%	13.68%	3.18%	10.99%	6.66%
Joint	mean	0.1755	30.15	0.3224	7.909	1.53E-04	2.862	54.59	589.7
F11-F20	CoV	3.70%	2.21%	5.38%	2.28%	11.89%	2.72%	10.48%	6.62%
Joint	mean	0.2232	31.46	0.3549	7.810	1.64E-04	2.877	57.52	590.2
F1-F10	CoV	7.98%	1.92%	5.31%	2.11%	10.03%	2.60%	9.60%	6.17%

$G_{fc}, G_{f\tau}, G_{ft}, G_{fs}$ are in MN/m, and $\sigma_{cp}, \sigma_{\tau p}, \sigma_{tp}, \sigma_{su}$ are in MPa.

Table 4.3: Partial correlation matrix of the beam-end section.

	Effective concrete section						Trans. reinfmt.	
Parameter	G_{fc}	σ_{cp}	$G_{f\tau}$	$\sigma_{\tau p}$	G_{ft}	σ_{tp}	G_{fs}	σ_{su}
G_{fc}	1.0000	0.3899	0.1167	0.3796	0.0730	0.3981		
σ_{cp}	0.3899	1.0000	0.2064	0.4646	0.0639	0.7094		
$G_{f\tau}$	0.1167	0.2064	1.0000	0.2291	0.0561	0.2506		
$\sigma_{\tau p}$	0.3796	0.4646	0.2291	1.0000	0.1131	0.5419		
G_{ft}	0.0730	0.0639	0.0561	0.1131	1.0000	0.1619		
σ_{tp}	0.3981	0.7094	0.2506	0.5419	0.1619	1.0000		
G_{fs}							1.0000	0.9188
σ_{su}							0.9188	1.0000

"Trans. reinfmt." means "Transverse Reinforcement"

Table 4.4: Calculated probabilities of collapse extents.

Location of column removal	Probabilistic analysis				Deterministic analysis
	Intact	Local	Partial	Total	Collapse extent
1st story	0.6380	0.0000	0.2020	0.1600	Partial collapse
8th story	0.7914	0.0000	0.0414	0.1671	Total collapse
16th story	0.9000	0.0000	0.0329	0.0671	Total collapse
26th story	0.9340	0.0000	0.0460	0.0200	Intact
29th story	0.9914	0.0000	0.0043	0.0043	Intact

Table 4.5: Probability distributions of superimposed gravity loads.

Load type	Mean	CoV	Distribution type
Dead load (floor)	1.44 kN/m^2	0.10	Gaussian
Live load (floor)	4.79 kN/m^2	0.60	Gumbel
Dead load (roof)	0.48 kN/m^2	0.10	Gaussian
Live load (roof)	1.20 kN/m^2	0.60	Gumbel

Table 4.6: Partial correlation matrix of one beam-end PDZ.

	Effective concrete section						Long. reinfmt.	
Parameter	G_{fc}	σ_{cp}	$G_{f\tau}$	$\sigma_{\tau p}$	G_{ft}	σ_{tp}	G_{fs}	σ_{su}
G_{fc}	1.0000	0.0998	0.0169	0.0211	0.1389	0.0758		
σ_{cp}	0.0998	1.0000	0.2524	0.4142	0.0428	0.7174		
$G_{f\tau}$	0.0169	0.2524	1.0000	0.1667	0.0039	0.2242		
$\sigma_{\tau p}$	0.0211	0.4142	0.1667	1.0000	0.1893	0.5223		
G_{ft}	0.1389	0.0428	0.0039	0.1893	1.0000	0.1888		
σ_{tp}	0.0758	0.7174	0.2242	0.5223	0.1888	1.0000		
G_{fs}							1.0000	0.8744
σ_{su}							0.8744	1.0000

"Long. reinfmt." means "Longitudinal Reinforcement"

Table 4.7: Partial correlation matrix of one interior-column PDZ.

	Effective concrete section						Long. reinfmt.	
Parameter	G_{fc}	σ_{cp}	$G_{f\tau}$	$\sigma_{\tau p}$	G_{ft}	σ_{tp}	G_{fs}	σ_{su}
G_{fc}	1.0000	0.1386	0.0875	0.0373	-0.083	0.0375		
σ_{cp}	0.1386	1.0000	0.1999	0.5053	0.0922	0.6293		
$G_{f\tau}$	0.0875	0.1999	1.0000	0.3689	0.0300	0.2467		
$\sigma_{\tau p}$	0.0373	0.5053	0.3689	1.0000	0.1615	0.5629		
G_{ft}	-0.083	0.0922	0.0300	0.1615	1.0000	0.2324		
σ_{tp}	0.0375	0.6293	0.2467	0.5629	0.2324	1.0000		
G_{fs}							1.0000	0.8899
σ_{su}							0.8899	1.0000

"Long. reinfmt." means "Longitudinal Reinforcement"

Table 4.8: Probability distribution for all RC sections.

Parameter		G_{fc}	σ_{cp}	$G_{f\tau}$	$\sigma_{\tau p}$	G_{ft}	σ_{tp}	G_{fs}	σ_{su}
Beam	mean	0.0658	27.42	0.0231	4.077	1.13E-4	2.404	42.71	614.2
F1-F4	CoV	4.04%	3.57%	6.52%	4.00%	11.15%	3.55%	6.89%	4.51%
Beam	mean	0.0658	27.42	0.0231	4.077	1.13E-4	2.404	43.66	619.9
F5-F7	CoV	4.04%	3.57%	6.52%	4.00%	11.15%	3.55%	8.57%	5.00%
Beam	mean	0.0658	27.42	0.0231	4.077	1.13E-4	2.404	41.04	620.3
F8-F10	CoV	4.04%	3.57%	6.52%	4.00%	11.15%	3.55%	8.63%	5.03%
Col-in	mean	0.1742	28.75	0.0507	4.350	1.36E-4	2.246	43.97	539.66
F1-F2	CoV	4.12%	2.13%	5.35%	2.55%	11.81%	2.92%	7.99%	4.62%
Col-in	mean	0.1461	28.10	0.0471	4.326	1.38E-4	2.246	52.31	588.2
F3-F5	CoV	3.47%	2.16%	4.66%	2.40%	11.38%	2.79%	8.46%	5.39%
Col-in	mean	0.1309	27.20	0.0420	4.299	1.37E-4	2.249	57.49	616.7
F6-F10	CoV	9.44%	2.21%	4.52%	2.53%	11.55%	2.91%	7.40%	4.86%
Col-ex	mean	0.1051	27.04	0.0332	4.107	1.24E-4	2.318	39.03	542.8
F1-F2	CoV	5.16%	2.95%	6.36%	3.59%	11.62%	3.25%	9.19%	4.59%
Col-ex	mean	0.0756	26.53	0.0289	4.084	1.25E-4	2.314	51.80	617.6
F3-F5	CoV	4.73%	2.75%	9.26%	3.65%	12.14%	3.24%	8.15%	4.99%
Col-ex	mean	0.0756	26.53	0.0289	4.084	1.25E-4	2.314	44.25	620.0
F3-F10	CoV	4.73%	2.75%	9.26%	3.65%	12.14%	3.24%	8.10%	5.17%
Wall	mean	0.0224	24.38	0.0119	4.089	1.34E-4	2.473	18.55	620.2
F1-F10	CoV	4.03%	4.35%	4.43%	3.90%	8.32%	3.30%	9.19%	5.06%
Slab-1	mean	0.0238	23.11	0.0148	3.536	1.10E-4	2.589	30.35	619.9
F1-F10	CoV	6.91%	7.39%	8.83%	6.43%	9.58%	5.52%	7.35%	5.04%
Slab-2	mean	0.0188	22.10	0.0110	3.507	1.10E-4	2.571	30.35	619.9
F1-F10	CoV	7.00%	7.25%	6.02%	6.40%	10.33%	5.95%	7.35%	5.04%

Note: 1. $G_{fc}, G_{f\tau}, G_{ft}, G_{fs}$ are in MN/m, and $\sigma_{cp}, \sigma_{\tau p}, \sigma_{tp}, \sigma_{su}$ are in MPa.
2. "Col-ex" and "Col-in" mean exterior and interior column sections, respectively.
3. "Slab-1" and "Slab-2" mean slab sections with and without shear studs, respectively.

Table 4.9: Calculated collapse load factor α_l using deterministic analysis.

Column removal location	Reduced roof loads	Full roof loads
1st story	0.852	0.845
5th story	0.854	0.845
9th story	0.945	0.849
10th story	1.070	0.837

Table 4.10: Calculated occurrence probabilities of collapse extents.

Column/Wall removal case	Location of removal	Probabilistic analysis			Det. analysis
		Intact	Partial	Total	collapse extent
2 perimeter columns	1st story	0.2450	0.0600	0.6950	Total
2 perimeter columns	5th story	0.4650	0.0000	0.5350	Total
2 perimeter columns	9th story	0.9233	0.0000	0.0767	Total
2 perimeter columns	10th story	0.9950	0.0000	0.0050	Intact
Wall panel	1st story	0.0800	0.0300	0.8900	Total
Wall panel	5th story	0.1850	0.0000	0.8150	Total
Wall panel	9th story	0.8350	0.0000	0.1650	Total
Wall panel	10th story	1.0000	0.0000	0.0000	Intact

note: "det." means "deterministic"

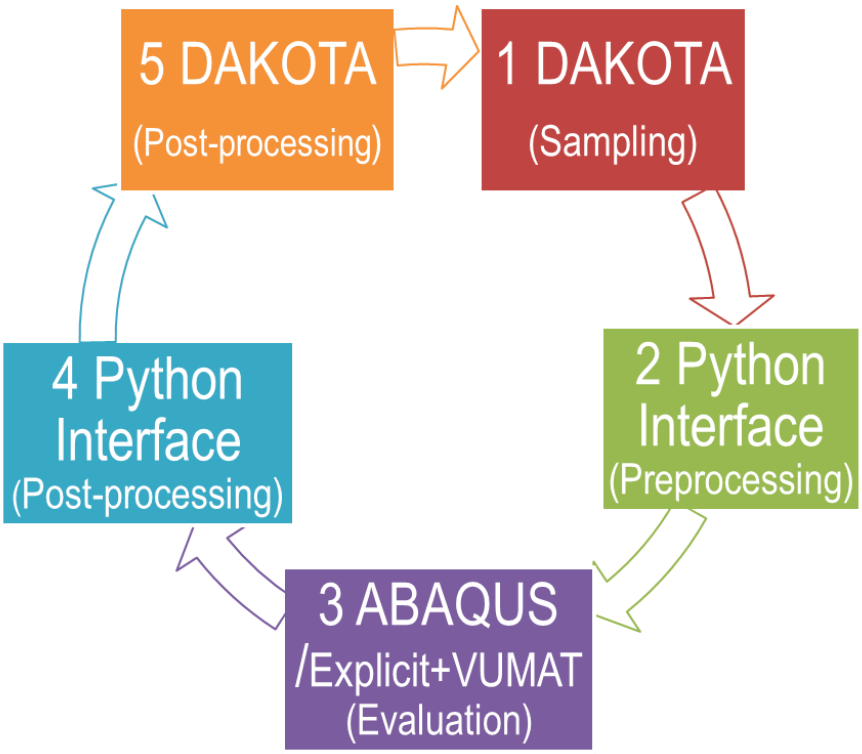

Figure 4.1: Stochastic analysis framework for risk assessment of building structures.

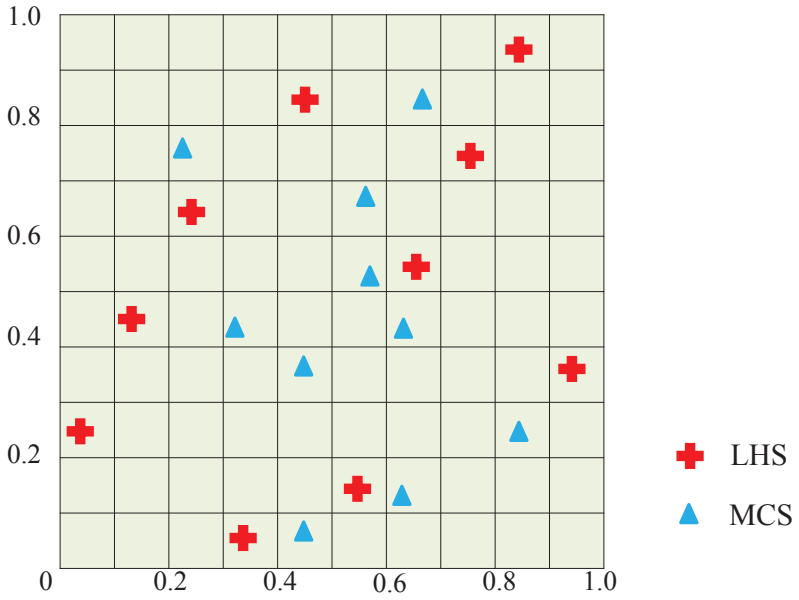

Figure 4.2: Distribution of sample points for the MCS and LHS methods with 5 samples.

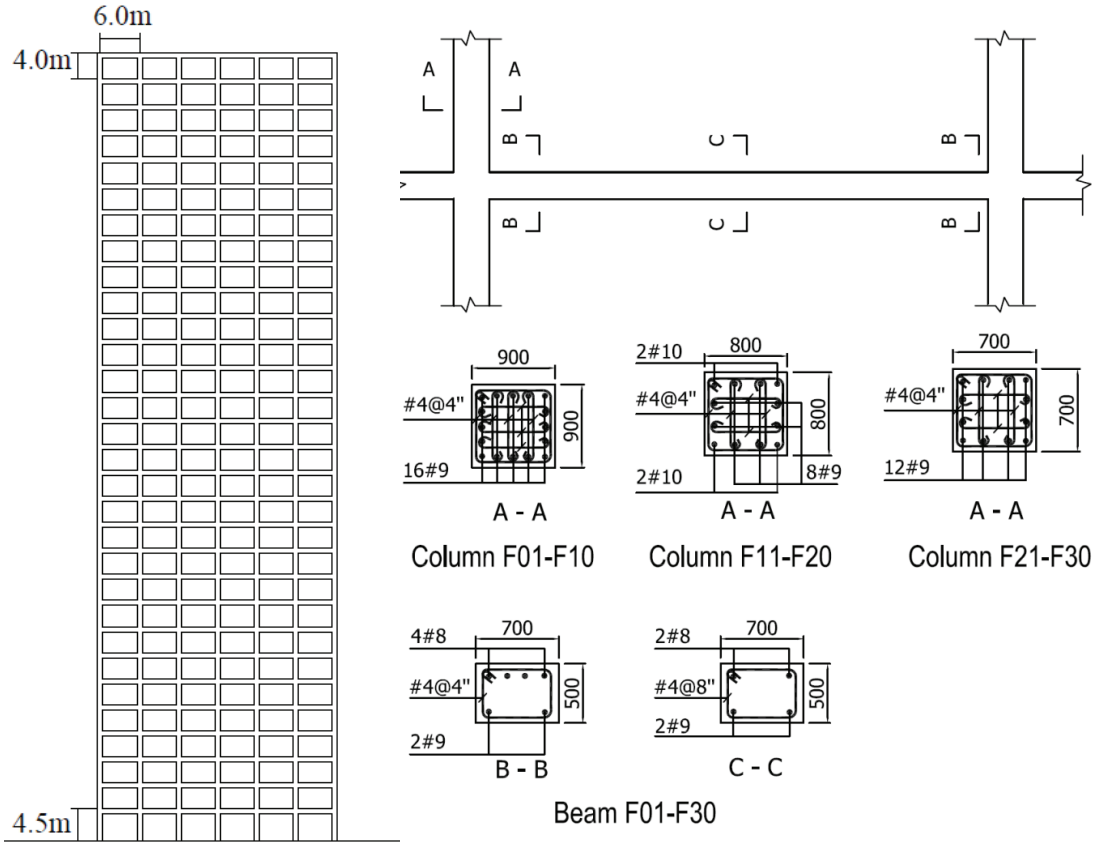

Figure 4.3: Structural Design of a 2D 30-story RC frame structure.

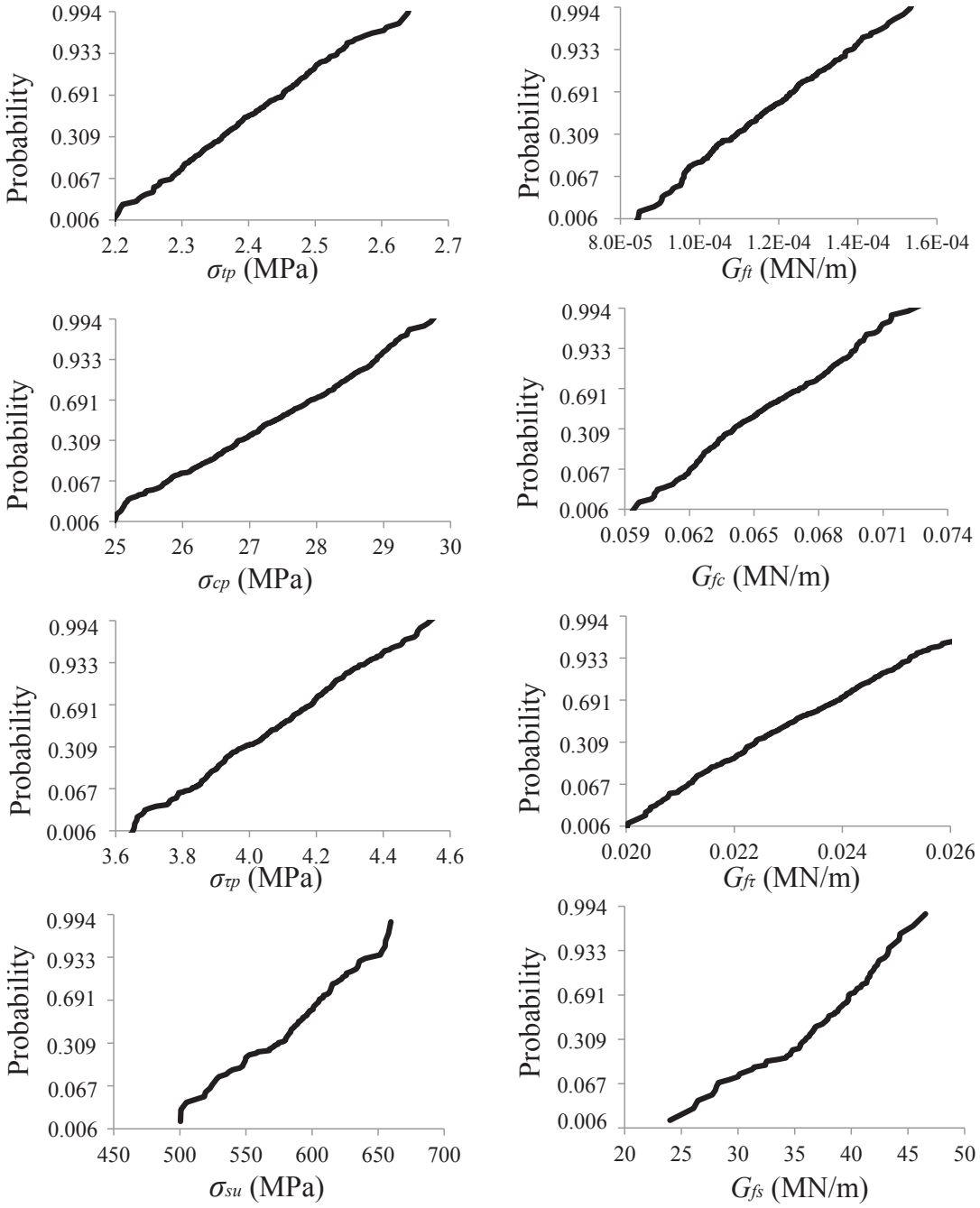

Figure 4.4: Probabilistic distribution of cohesive properties of one PDZ.

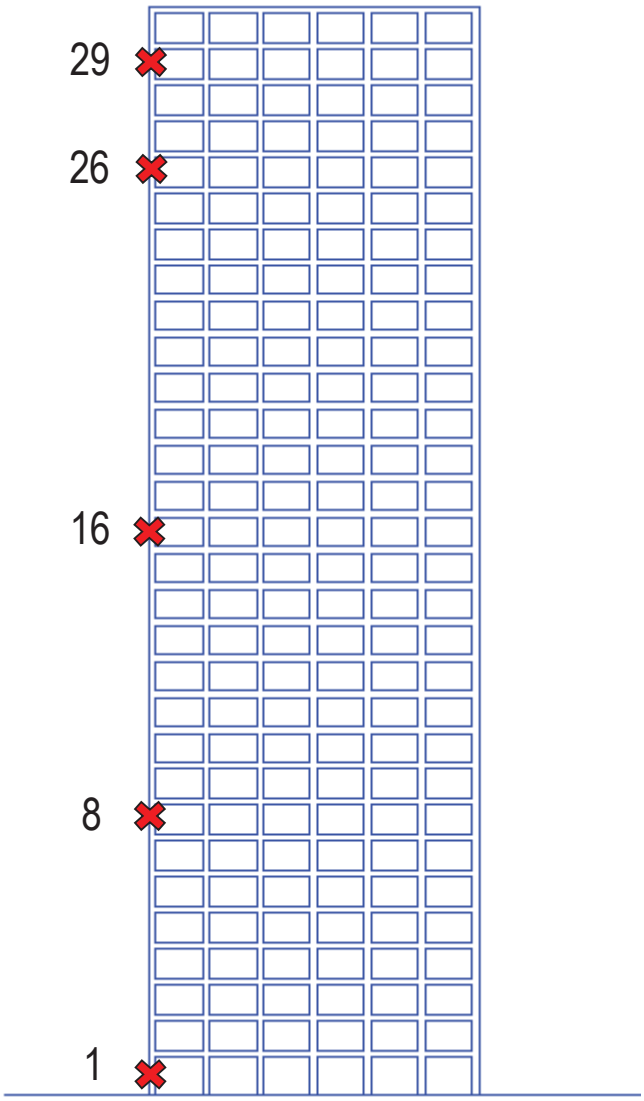

Figure 4.5: Five initial damage scenarios for collapse analysis.

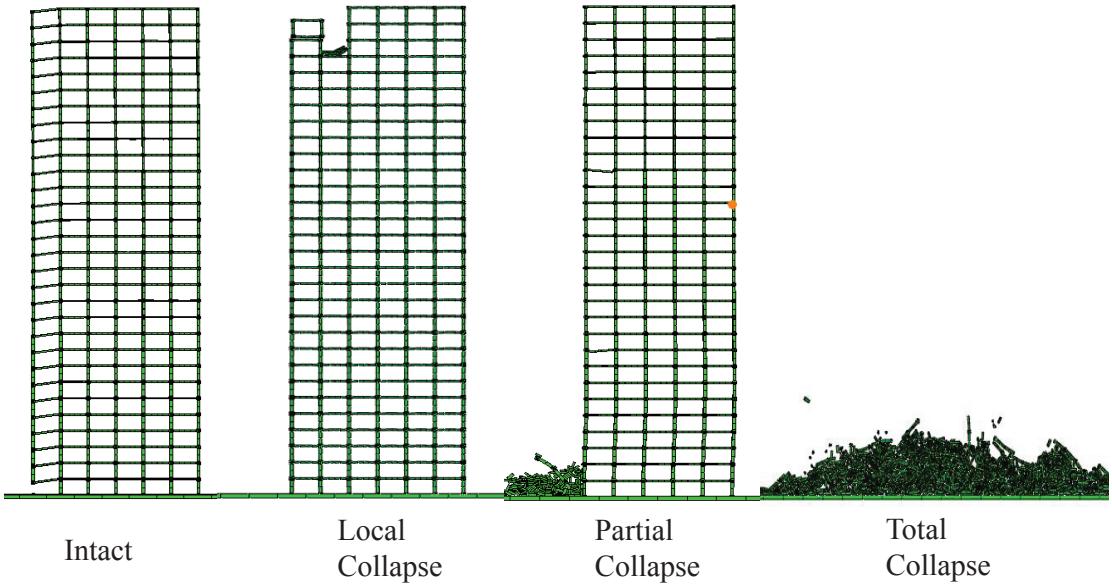

Figure 4.6: Four final collapse extents.

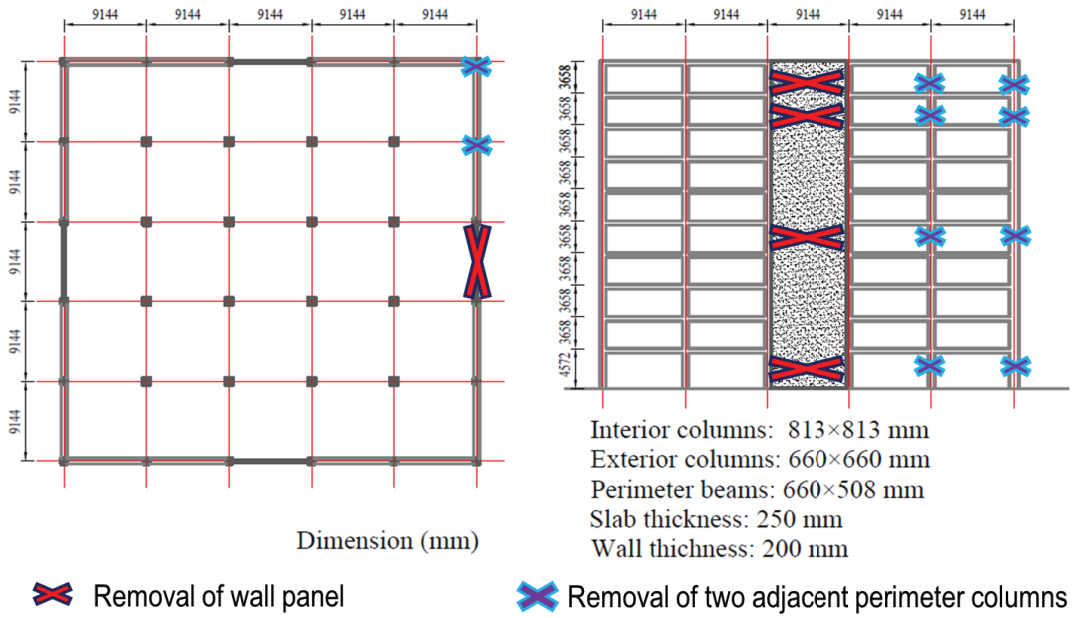

Figure 4.7: A 10-story RC building with eight initial damage scenarios.

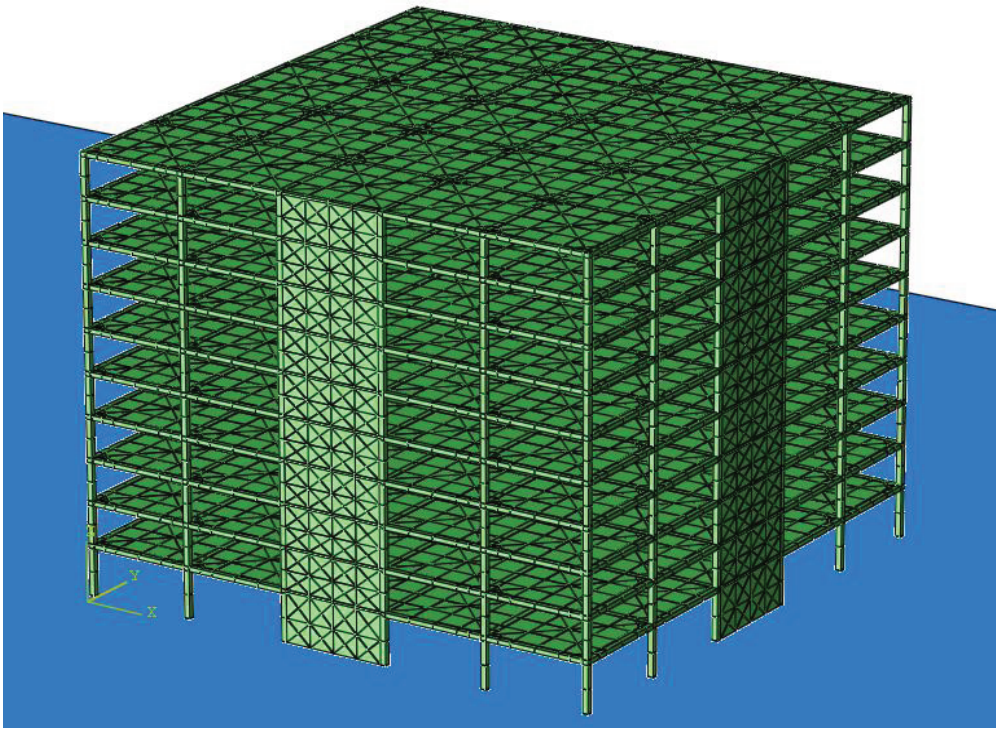

Figure 4.8: Two-scale model of the 10-story prototype building.

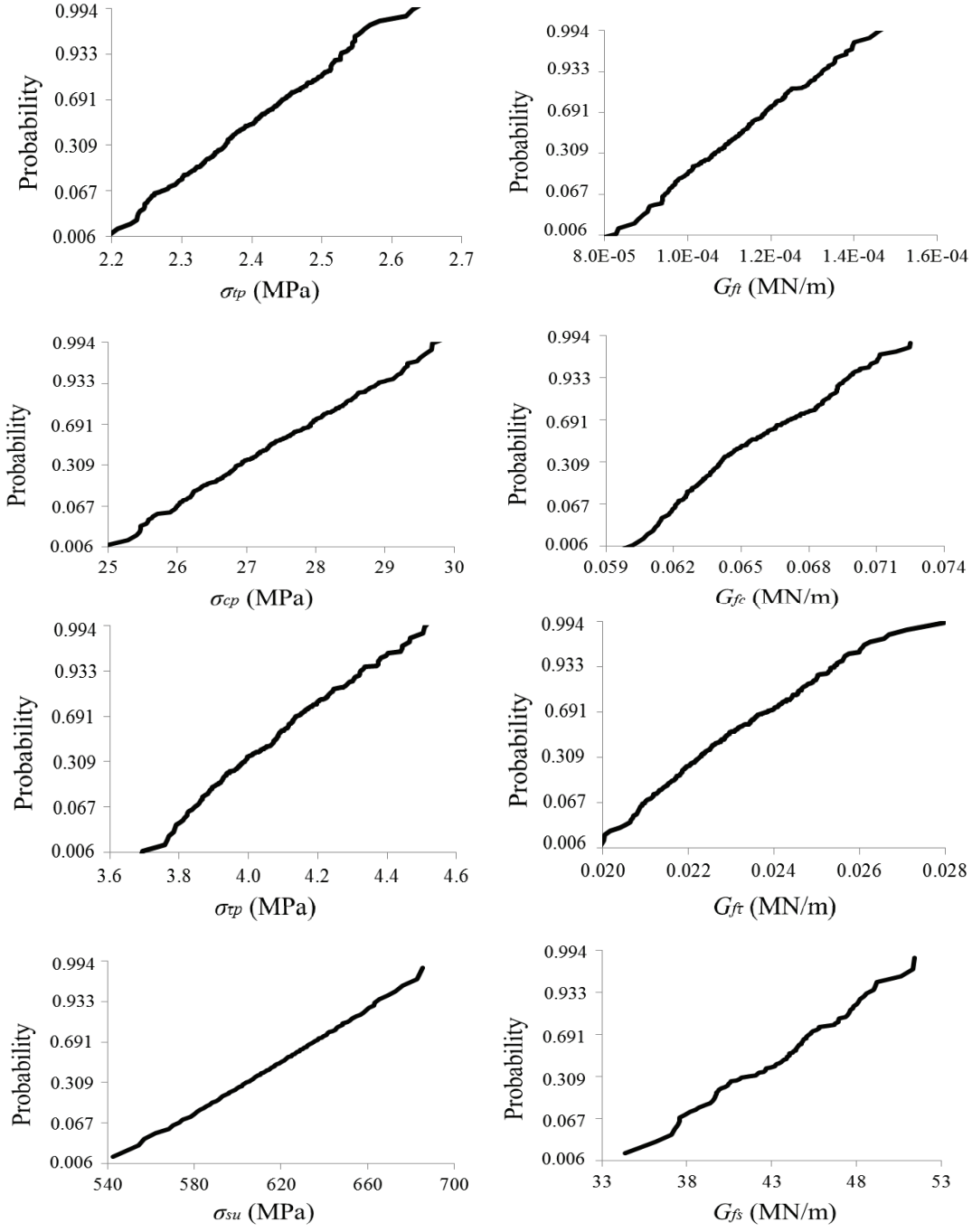

Figure 4.9: Probabilistic distributions of cohesive properties of one beam-end PDZ.

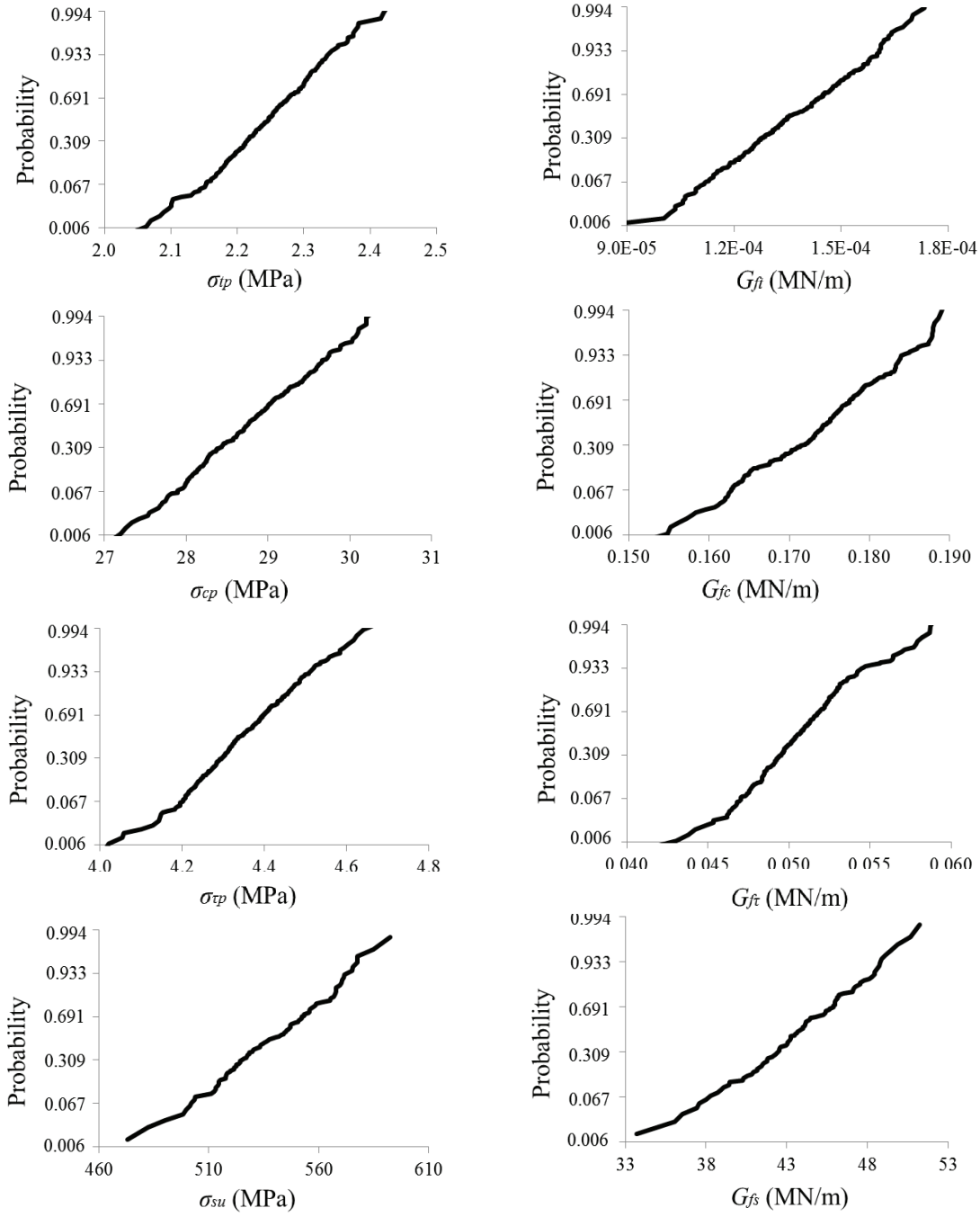

Figure 4.10: Probabilistic distributions of cohesive properties of one interior-column PDZ.

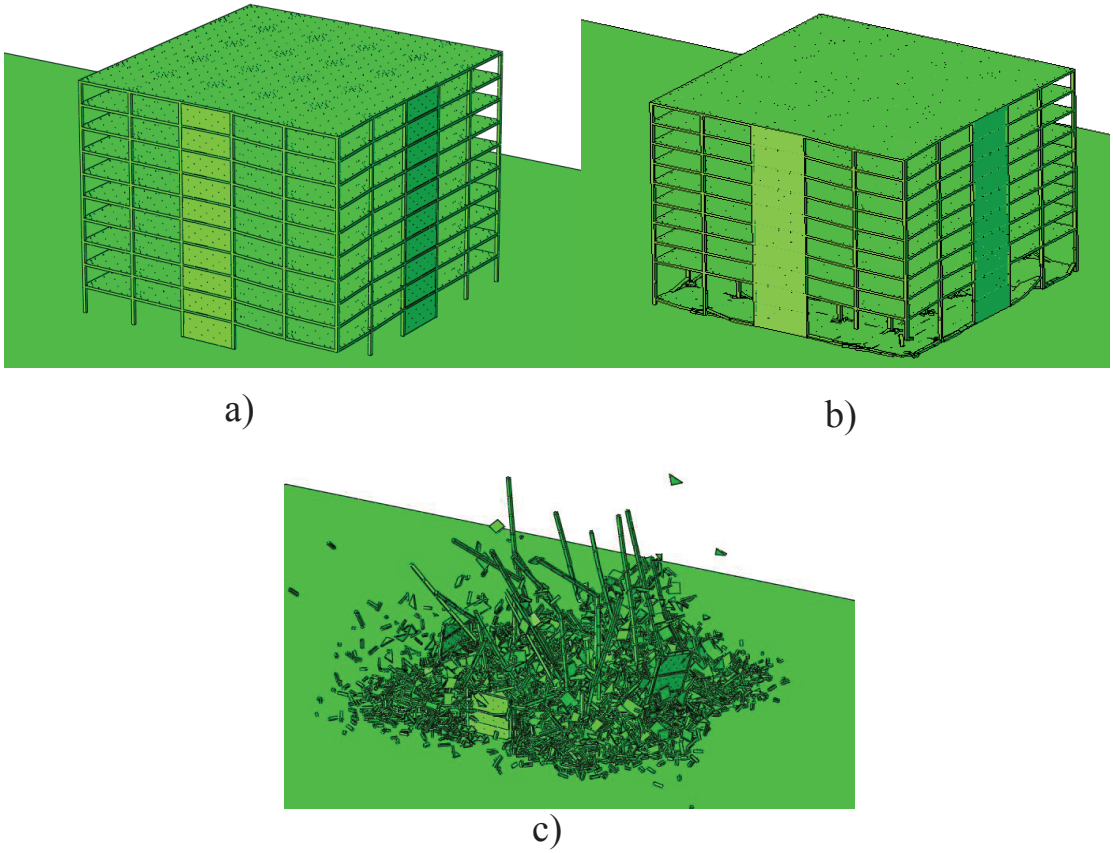

Figure 4.11: Three final collapse extents of the 3D prototype building.

Chapter 5

Simplified Energy-Based Analysis Method

5.1 Background

From the viewpoint of the system reliability analysis, $P[C|LD]$ in Eq. 4.1 is equivalent to the union probability of the occurrence of all possible failure sequences that could lead to a collapse event [28, 73], i.e.:

$$P[C|LD] = \Pr(\cup_i S_i) \tag{5.1}$$

where $S_i = i$th failure sequence. For large structural systems, it is common to approximate Eq. 5.1 by considering only the significant failure sequences, which are believed to contribute to the most part of the overall failure probability. Over the past two decades, extensive efforts have been devoted towards the development of efficient methods for calculating this union probability for large structural systems, such as branch and bound method [79], importance and adaptive sampling methods [76, 58, 78], hybrid simulation-based method [73], bounds estimation using linear programming [100, 101], etc. In most

applications of these methods, the calculation of the structural resistance usually does not consider detailed material constitutive models. However, for the analysis of collapse behavior of reinforced concrete (RC) buildings, it is essential to consider damage and fracture of materials under a general loading state, which requires a considerable amount of modeling and computational efforts.

In previous chapters, a stochastic cohesive element model was developed to calculate the collapse probability of RC buildings through nonlinear dynamic analysis. The model adopted the concept of cohesive fracture to simulate the nonlinear behavior of RC structural members. Despite that nonlinear dynamic analysis was used, the model was shown to be able to handle normal RC buildings with a reasonable computational cost. However, it is still a computational challenge to directly apply the model to high-rise RC buildings, where many of them could be critical buildings requiring the collapse analysis. Furthermore, the computational efficiency of the model has not reached a level suitable for reliability-based design optimization (RBDO) of general RC buildings against progressive collapse, which usually combines the optimization procedure and stochastic simulations [35]. Therefore, there is still a need to develop some more efficient numerical models, which can fully facilitate the reliability-based analysis and design of RC buildings against progressive collapse.

In this chapter, we develop a simplified computational model for assessing the collapse risk of RC buildings subjected to local structural damage. The model combines an energetic-equivalent cohesive element model and a sequential linear analysis method. Here collapse is defined as the initiation of the movement of collapse front. This is because studies have shown that, once a collapse front is formed and moves under gravity, the lower intact part of the building is unlikely to be able to resist the upper falling part [108, 65]. Such a definition of collapse also aligns with the Unified Facilities Criteria (UFC) recommendations, in which the tolerable damage is only allowed in a limited

area around the location where the local structural damage occurs [29].

5.2 Energetic-Equivalent Elastic Cohesive Model

In Chapter 2, a two-scale computational model is proposed to efficiently evaluate the collapse potential of RC buildings subjective to initial damage. In this model, a set of coarse-scale cohesive elements is used to simulate the nonlinear behavior of various structural members, representing potential damage zones (PDZs) during the collapse process. The constitutive behavior of the cohesive element is formulated by separating the PDZ into two parts, the effective concrete section and the longitudinal reinforcement. The mechanical behaviors of these two parts are both characterized by nonlinear traction-separation relationships, which can be calibrated through the procedure presented in Chapter 2.

With this two-scale model, the collapse risks of two prototype RC buildings are quantified in Chapter 4 through stochastic analysis, which involves the nonlinear cohesive modeling of RC structures. According to the risk assessment results of the prototype 10-story RC building in Chapter 4, it is found that about 400 CPU hours by using a regular quadcore computer would be required for each initial damage scenario. Such computational cost is acceptable for a single collapse risk quantification but is not suitable for design optimization, which would involve a number of trial design schemes and for each trial design scheme stochastic analysis is required. In light of the above, the efficiency of two-scale model still needs to be improved.

It is evident that one major part of the computational cost for collapse analysis comes from the modeling of the nonlinear constitutive behavior of materials. Therefore, it is desirable to remove the nonlinear cohesive elements in the model. In this study, we model the nonlinear damage of the PDZ by an energetic-equivalent elastic cohesive element. It is noted that in several studies various kinds of energy-based approaches

have been developed for the analysis of progressive collapse [19, 52, 112], where the essential idea is to create a simplified structural model that preserves the total energy dissipation of the failure of structural members. The present model shares the same spirit with these studies as the energy equivalence principle is used to formulate the elastic cohesive element as well as to determine the damage extent of the element. As will be described in the next section, the present elastic cohesive elements can be implemented with a sequential analysis framework, which allows an efficient calculation of the collapse risk.

Following the aforementioned formulation of the constitutive behavior of cohesive elements, we consider that the elastic stiffnesses of each integration point of the cohesive element are determined such that the elastic energy stored at the ultimate separation is equal to the actual energy dissipation of the corresponding portion of the PDZ (Fig. 5.1), i.e.:

$$\bar{E}_i = 2G_i/\delta_{iu}^2 \tag{5.2}$$

where $\bar{E}_i$ $(i = t, c, \tau)$ = effective stiffnesses of the integration point of the elastic cohesive element under tensile, compressive and shear loading, respectively, G_i = actual fracture energies of the corresponding portion of the PDZ under these single-mode loading, and δ_{iu} = actual ultimate separations under these loading.

To use the elastic cohesive element for the collapse analysis, certain failure criterion must be enforced. Here we define a load-to-resistance ratio μ, which compares the total elastic energy stored in the cohesive element with the actual energy dissipation capacity of the corresponding PDZ:

$$\mu = \frac{\sum_{k=1}^{4} \sigma_{kn} w_{kn} + G_\tau (w_{km}^2 + w_{kl}^2)}{2 \sum_{k=1}^{4} G_{kt}} \tag{5.3}$$

where w_{kj} $(j = n, l, m)$ = cohesive separations of the kth integration point in the

normal and two shear directions, and G_{kt} = actual overall energy dissipation capacity of the kth integration point under the given loading mode. It is clear that $\mu \geq 1$ represents a sufficient condition for the failure of the PDZ. As will be discussed in the next section, this load-to-resistance ratio is used to determine the damage status of the PDZ within the framework of linear elastic structural analysis. It is noted that the present formulation essentially captures the energy equivalence between the present elastic elements and the previously developed nonlinear cohesive elements at the actual ultimate separation. It is evident that these two models will yield different time histories of the cohesive response during the loading. However, the essential point here is that both models will give the same prediction of the failure status of the structural member evaluated based on the energy dissipation. This is sufficient for the purpose of searching the failure sequences for the collapse initiation.

The key parameters that determine the effective stiffnesses of the elastic cohesive element and the load-to-resistance factor are 1) total energy dissipation of the PDZ for any given mode mixity, and 2) ultimate separation under single-mode loading. In this study, we determine these parameters from the properties of the aforementioned nonlinear cohesive elements. Therefore, we can use the calibration procedure for the nonlinear cohesive elements, as described in Chapter 2, to determine the properties of the elastic cohesive elements.

According to the constitutive relationship of the nonlinear cohesive element, the energy dissipation of the PDZ can be calculated from the effective concrete section and longitudinal reinforcement:

$$G_{kt} = G_{kec} + G_{ks} \tag{5.4}$$

where G_{kec} and G_{ks} denote the energy dissipations of the effective concrete section and longitudinal reinforcement, respectively, for the kth integration point of the cohesive

element. It is clear that G_{kec} is dependent on the mode mixity angle governed by w_n, w_m and w_l. Based on the formulation of the aforementioned nonlinear cohesive elements (Eqs. 2.1a-2.1c), the mode mixity dependence of the energy dissipation of the effective concrete section can be simply written as

$$G_{kec} = \frac{1}{2}\sigma_p \bar{w}_u = F(\sigma_{ip}, w_{iu}, \alpha_t, \alpha_c, \beta_t, \beta_c, \gamma_t, \gamma_c) \tag{5.5}$$

where $i = t, c, \tau$ denoting tensile, compressive, and shear loading, respectively. Based on the simplified constitutive relationship proposed for effective concrete section (Eqs. 2.5), the ultimate separations can be computed as $w_{iu} = 2G_{ip}/\sigma_{ip}$, where G_{ip} = cohesive energy dissipations under the pure tensile, compressive and shear loading, respectively.

The energy dissipation of the longitudinal reinforcement can be calculated from its cohesive behavior as $G_{ks} = \rho_k G_{cs}$ (ρ_k = reinforcement ratio of the part of the PDZ represented by the kth integration point, and G_{cs} = cohesive energy dissipation of the longitudinal reinforcement). If the normal force is tensile, then G_{cs} is equal to the entire area under the cohesive law of the longitudinal reinforcement (Fig. 2.3). If the normal force is compressive, then we consider that the RC section would disintegrate once the concrete fails in compression [65], and therefore in this case G_{cs} is equal to the area under a part of the cohesive law of the longitudinal reinforcement, where the ultimate separation is determined by the concrete failure.

The ultimate separation δ_{iu} under single loading mode can be determined as follows: 1) for pure tensile loading, δ_{tu} is equal to the ultimate separation of the longitudinal reinforcement since the ultimate tensile failure is governed by the rupture of the steel reinforcement, 2) for compressive loading, δ_{cu} is equal to the ultimate separation of the effective concrete section in compression and 3) for shear loading, $\delta_{\tau u}$ is equal to the ultimate separation of the effective concrete section in shear since the longitudinal reinforcement has a negligible contribution to the shear resistance.

It is evident that the effective stiffness of the elastic elements and total energy dissipation would be inherently random variables, whose probability distributions are directly related to the randomness of the material properties of concrete and steel reinforcement. It should be pointed out that, even though the present framework is anchored by a linear elastic model, the calibration of the model parameters involves nonlinear stochastic simulations of the PDZ, which enforces the energy-equivalence of the model and therefore ensure an accurate estimation of the damage status.

5.3 Sequential Linear Elastic Structural Analysis

Now we apply the present elastic cohesive model to analyze the collapse behavior of the building. As mentioned earlier, the essence of the collapse analysis is to search the possible failure sequences that would lead to the collapse initiation (Eq. 5.1). Meanwhile, we attempt to avoid nonlinear dynamic analysis in order to improve the computational efficiency. In this study, we adopt a sequential analysis approach to perform the search of the failure sequences, in which every step only involves a linear elastic static analysis.

For the probabilistic analysis of progressive collapse, we consider randomness in both gravity loads and material properties. Since the loads and material properties are statistically independent, we can calculate the collapse risk as

$$P_f = \int_L P_f|_L f(L)\mathrm{d}L = \mathrm{E}(P_f|_L) \tag{5.6}$$

where $P_f|_L$ = probability of collapse initiation for given gravity loads L, $f(L)$ = joint probability density function of the applied loads, and $\mathrm{E}(x)$ = expectation of x. Eq. 5.6 can be rewritten as

$$P_f = \frac{1}{p}\sum_{i=1}^{p} P_f|_{L_i} = p^{-1}\sum_{i=1}^{p}\left[q^{-1}\sum_{j=1}^{q}\Phi_j(L_i)\right] \tag{5.7}$$

where p = number of samplings of the gravity loads, q = number of samplings of the properties of the cohesive elements, and $\Phi_j(L_i)$ = failure index for the jth sampling of the cohesive property with the ith sampling of loads. If a failure sequence is found, $\Phi_j = 1$, otherwise $\Phi_j = 0$.

It is clear that the critical step of evaluating the collapse risk is the calculation of $\Phi_j(L_i)$, which is essentially the search of a complete failure sequence that could lead to collapse initiation. For each set of sampled gravity loads and cohesive properties, we use the algorithm shown in Fig. 5.2 to search the failure sequences, which is described as below:

1) We perform an linear elastic analysis of the entire building for sudden removal of individual structural members, e.g. a set of columns. During this step, we apply a factor of two to the factored gravity loads, which takes into account the dynamic effect from the sudden loading as a result of structural element removal [91]. It is noted that this dynamic load factor is in correspondence with the present linear elastic static analysis. This would certainly over-predict the dynamic effect and give a conservative estimation of the damage status since the actual PDZs would behave in a quasi-brittle or ductile manner depending on the loading mode. From this analysis, we calculate the load-to-resistance ratio μ for each cohesive element. If all μ values are less than one, it implies that for this particular set of sampled loads and cohesive properties no failure of cohesive element is observed and therefore the building is intact, i.e. $\Phi_j = 0$.

2) If some μ values are larger than one, we deactivate the cohesive element with the largest μ value by setting its stiffness to be zero, which leads to a new structure. We will then perform a linear elastic analysis of the updated structure with the original factored gravity load. It should be pointed out that no dynamic load factor is applied in this step because the PDZ is expected to experience a gradual failure. This is different from the previous step of analysis, where the additional loading due to structural element

removal is instantaneously applied to the building. Similar to step 1, we can calculate the μ values for all cohesive elements and check them against one. If all of them are smaller than one, then we assign $\Phi_j = 0$. Otherwise, we repeat this step by deactivating the most damaged cohesive element and create a new structure for the subsequent linear elastic analysis.

3) We repeat step 2 till either no more damaged cohesive elements can be found (i.e. all μ values are less than one and the structure is intact) or the stiffness matrix of the entire structure becomes singular (i.e. collapse initiates). For the former case, we have $\Phi_j = 0$ and for the latter case we have $\Phi_j = 1$.

The aforementioned procedure essentially searches the most damaged cohesive element with $\mu \geq 1$ in a sequential manner, where the required number of linear elastic static analysis is equal to the number of cohesive elements that form a complete failure path. From a computational viewpoint, the present procedure is much more efficient than the conventional dynamic analysis which naturally involves the modeling of the nonlinear material constitutive behavior. In order to save the computational effort, the present analysis clearly includes some simplifications and approximations. As a result, it is expected that the analysis would not yield an exact collapse probability. But how would the results of the present analysis compare with those obtained by using nonlinear dynamic analysis?

To answer this question, we consider that all the cohesive properties are fixed and we are interested in calculating the critical value of the gravity load that would lead to collapse initiation. Now consider a failure sequence, which involves the failures of k numbers of cohesive elements. Within the framework of the present analysis, the failure criterion of ith cohesive element ($i = 1, ...k$) can be written as:

$$\frac{1}{2} C_i P^2 = G_{ti} \tag{5.8}$$

where P = applied gravity loading, C_i = effective compliance of the cohesive element

such that $0.5C_iP^2$ = strain energy stored in the ith cohesive element, and G_{ti} = total energy dissipation capacity of the corresponding PDZ. Based on Eq. 5.8, the failure load for the ith cohesive element P_i is equal to $\sqrt{2G_{ti}/C_i}$. The present sequential analysis method essentially implies that the collapse load P_c is equal to the minimum of the failure loads for all k number of cohesive elements, i.e.:

$$P_c = \min_{i=1,\ldots,k} \left(\sqrt{2G_{ti}/C_i} \right) \tag{5.9}$$

It is noted that for each step of the sequential analysis the equilibrium condition is satisfied and only one element is allowed to fail. This implies that the computed failure load corresponds to a statically admissible field but not a kinematically admissible mechanism. Therefore, the actual collapse load would be greater than the failure load computed from each step, i.e. $P_{act} > \sqrt{2G_{ti}/C_i}$. With Eq. 5.9, it is clear that for a given set of energy dissipation capacities of the cohesive elements the collapse load predicted by the present model would be a lower bound of the actual collapse load, i.e. $P_c < P_{act}$. Therefore, for a given set of random gravity loads, the present model would yield an upper bound of the collapse risk.

Now the question is how good is this upper bound of the collapse risk predicted by the present model. The understanding of the tradeoff between the improvement of computational efficiency and the accuracy of the results is critical for evaluating the applicability of the present method. In the next section, we attempt to answer this question by applying the present model to analyze the prototype RC building, which has been analyzed in Chapter 4.

5.4 Application to Risk Analysis of RC Building

In this section, we apply the present elastic cohesive model to evaluate the collapse risk of a 10-story prototype RC building. This building was also analyzed by using the

nonlinear cohesive elements as described in Chapter 4. The results of this recent study will serve as a benchmark for comparison, through which we evaluate the performance of the present model in terms of the accuracy of the prediction as well as the computational efficiency.

5.4.1 Description of Analysis

In this application, we consider four column-removal scenarios of the 10-story prototype RC building in Chapter 4 as shown in Fig. 4.7, i.e. removal of two adjacent perimeter columns on the 1st, 5th, 9th, and 10th floors. The risk assessment with this simplified energy-based model uses the same load combination and load probability distributions as the probabilistic analysis in Chapter 4, which are listed in Table 4.5. The values of mode-mixity parameters and the probability distributions of cohesive properties of all types of PDZs have already been calibrated in Chapter 4 and presented in Table 4.8. The statistical spatial correlation of cohesive properties and gravity loads also follows the spatial division approach in Chapter 4.

In the stochastic simulations, all the partially correlated random cohesive properties are sampled by the LHS technique as discussed in Chapter 4. The sampled cohesive properties, i.e. fracture energies and cohesive strengths, are further used to compute the effective stiffnesses of the elastic cohesive elements (Eq. 5.2) as well as the load-to-resistance ratio (Eq. 5.3). Based on Eq. 5.6, for a given sampled set of gravity loads we check the calculated collapse probability $P_f|_{L_i}$ every 20 realizations until the calculated probabilities converge within a relative error of 5% or within an absolute error of 0.001. Similarly, we keep sampling the gravity loads until the overall collapse probability P_f meets the aforementioned convergence criterion.

5.4.2 Results and Discussion

Table 5.1 shows the calculated collapse probabilities by the present model in comparison with those recently computed using the nonlinear cohesive element model [114]. From Table 5.1, it is seen that the collapse probabilities predicted by the present analysis are always greater than those predicted by the nonlinear dynamic analysis. This is consistent with the upper bound characteristics of the present analysis, as discussed in previous section. It is noted that the differences in collapse probabilities predicted by the present model and benchmark solutions are reasonably acceptable. For high failure risk cases, the difference is about 0.09, and for low failure risk cases, the difference is about 0.01. Yet, the present model is seen to significantly improve the computational efficiency. For columns removal at a lower story, the computational time is reduced by about 60%, and for columns removal at a higher story, the computational time is reduced by about 10-20 times.

It is noted that for nonlinear dynamic analysis the computational time is almost independent of the location of column removal, and on the contrary, the computational time of the present analysis significantly reduces as we remove columns at a higher story. The computational cost of nonlinear analysis is mainly due to the small time increment required for handling the material nonlinearity as well as the dynamics. If the entire building is modeled by nonlinear cohesive elements, it is expected that the computational cost for simulating collapse initiation is almost the same for different column removal locations. Nevertheless, if we are interested in simulating the entire collapse process including the collapse front propagation, then the computational cost of the nonlinear analysis would strongly depend on the column removal locations due to the large difference in the collapse duration. For the present analysis, the majority of the computational time is contributed to the sequential analysis procedure. It is found that for column removal at lower stories there are more failure sequences which involve

failures of more cohesive elements. This indicates that there would be more steps in the sequential analysis to search a complete failure sequence, which leads to a considerable increase in computational cost.

By using the sequential analysis approach, this present model enables us to tract the development of each failure sequence. After collecting the information of all failure sequences for these four initial damage scenarios, it is found that nearly 95% of the failed cohesive elements are within four slab regions as indicated by Fig. 5.3. In this figure, three regions (region 1, 2 and 4) are around the columns, mainly involving cohesive elements near the slab-column connections while region 3 is located in the middle of an exterior span. For most failure sequences, the failure of cohesive element starts from region 2 due to a shear-dominant failure, commonly known as punching shear failure. After the failure of PDZs in region 2, the extra gravity load is transferred to columns in the vicinity horizontally and also to adjacent floors vertically. During this process, the cohesive elements in regions 1 and 4 start to fail and at the same time more failed cohesive elements are observed in region 2. As more and more PDZs fail in region 1, 2 and 4, the slab in region 3 loses its integrity due to the excessive gravity load imposed on it and a number of cohesive elements in this region fail under a flexural-shear loading condition. The above failure mechanisms are similar to what have been observed from the nonlinear dynamic analysis of the collapse process in Chapter 4.

Overall speaking, it is seen that for the purpose of risk analysis the present model is able to yield a reasonable upper bound with a low computational cost. If a more accurate prediction is needed, we could use the nonlinear cohesive model at a much higher computation cost. However, the nonlinear models would be computationally unaffordable for reliability-based design optimizations against progressive collapse. By contrast, the present model would be well suited for such a task because the model can explicitly enumerate the critical failure sequences and the corresponding cohesive

elements, which need to be specially designed or strengthened to achieve a targeted collapse risk. This would effectively limit the scope of the design optimization, which speeds up the optimization process, and more importantly, for each optimization trial, the present method can be used to evaluate the collapse risk in an efficient manner.

5.5 Conclusions

A linear cohesive element is developed to model the PDZs of different RC structural members. The linear behavior of the cohesive element is formulated based on an energetic equivalence principle, and an energy-based load-to-resistance ratio is proposed to characterize the damage status of the element. The cohesive model is calibrated from the nonlinear structural behavior of the corresponding PDZ under different loading modes.

The linear cohesive element model is implemented in a sequential analysis framework to efficiently evaluate the collapse risk of RC buildings. It is shown that the present model would yield an upper bound of the collapse risk due to the fact that each analysis step essentially enforces a statically admissible field but not a kinematically admissible mechanism. Moreover, this simplified model can still capture main failure mechanism observed by the nonlinear dynamic analysis.

The present model is applied to a prototype RC buildings subjected to different column removal scenarios. It is found that the present model is able to capture the same qualitative probabilistic collapse behavior as the nonlinear model does. In comparison with the nonlinear dynamic analysis, the present model overestimates the collapse probability by 0.01 (for low collapse risk cases) and 0.09 (for high collapse risk cases). Meanwhile, it is shown that the present model can significantly save the computational time. For column removal at a lower story, where there are a number of cohesive elements involved in the failure sequences, the computational time of the present analysis is about 40% of that of the existing nonlinear dynamic analysis. For column removal at a

higher story, where there are a less number of cohesive elements in the failure sequences, the present model can reduce the computational time by a factor of 10-20 compared to the nonlinear dynamic analysis. For the prototype building analyzed in this study, the tradeoff between the accuracy of the collapse risk prediction and the improvement of computational efficiency indicates that the present model could be an attractive choice for a simplified analysis of collapse risk of RC buildings.

Table 5.1: Comparison of calculated collapse probabilities.

Location of column removal	Nonlinear dynamic analysis [114]		Present analysis	
	Collapse risk	CPU time	Collapse risk	CPU time
1st story	0.7550	425	0.840	183
5th story	0.5350	419	0.620	115
9th story	0.0767	408	0.110	46
10th story	0.005	423	0.015	21

The unit for CPU time is "hour"

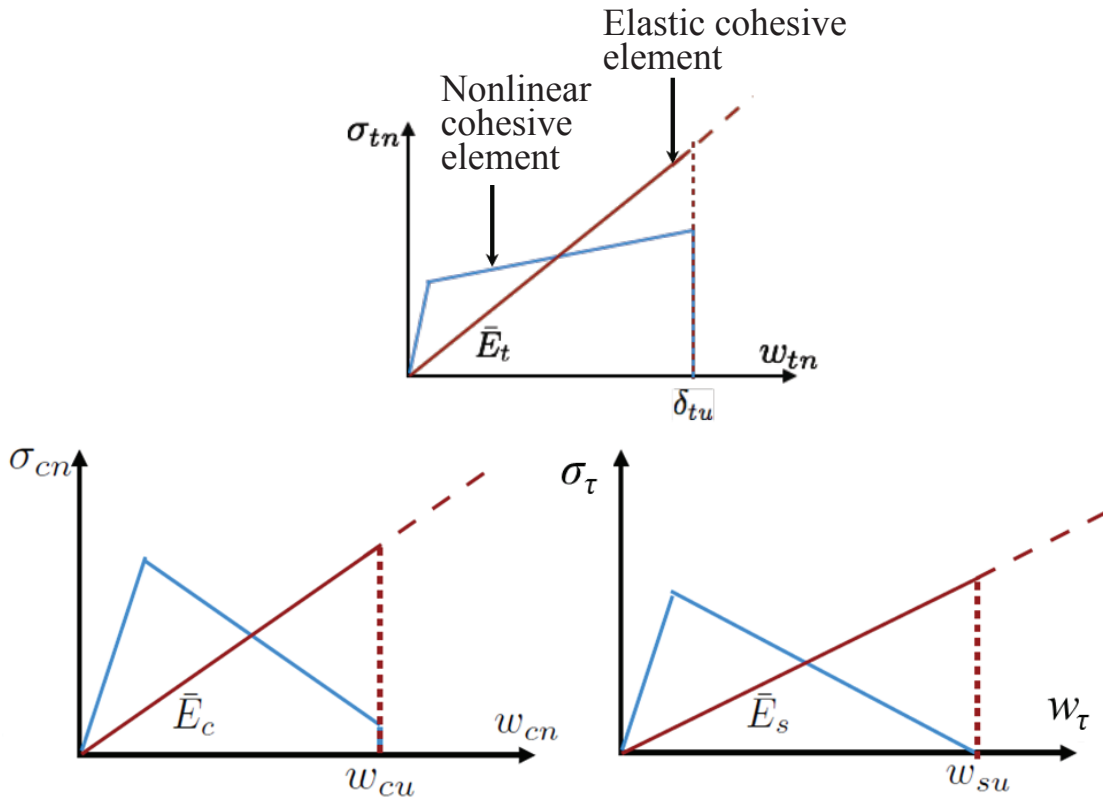

Figure 5.1: Energy-based equivalent stiffness calculation.

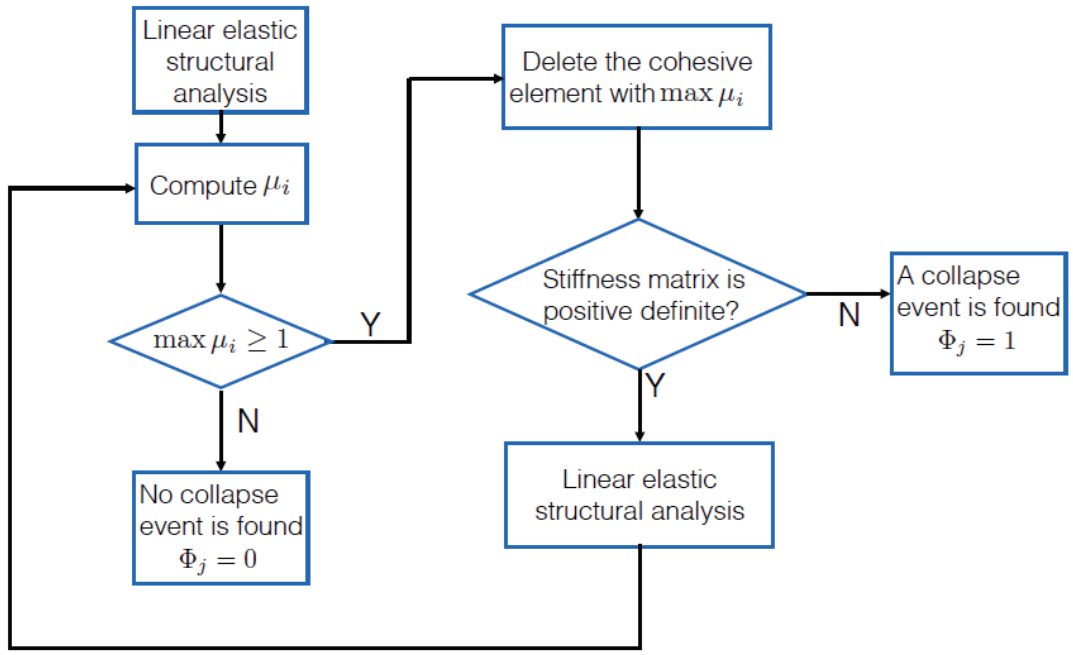

Figure 5.2: Flowchart for the failure sequence search with the simplified energy-based analysis method.

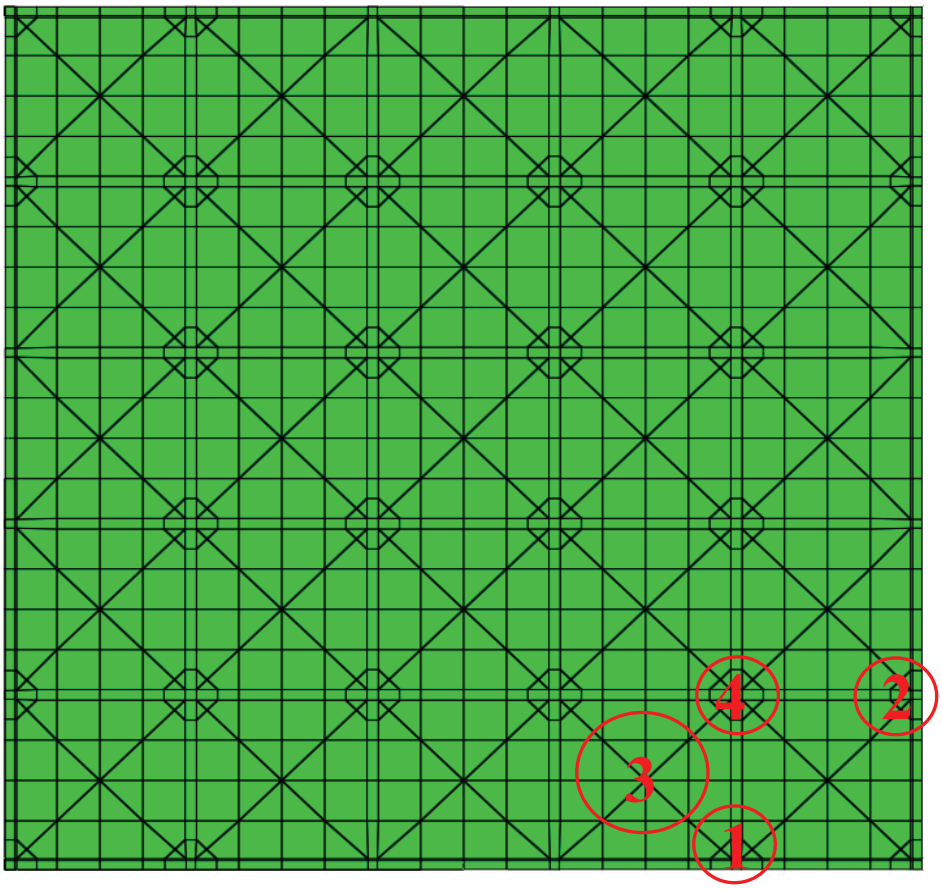

Figure 5.3: Concentrated damage regions on the floor.

Chapter 6

Reliability-Based Design Optimization

6.1 Background

RBDO has been recognized as an essential tool for reliability-based structural design[37]. In 1990s, a conceptual framework for RBDO [38] was first proposed to search for the most cost-effective means of inspection and repair to maintain the serviceability of concrete components or structures. The RBDO method was also used to improve the performance-based structural design of highrise buildings under wind excitations [102, 103]. Recently, both component- and system-level RBDO methods were proposed to search for the optimal topology scheme of 2D and 3D structures under the uncertainties coming from external loading [81]. Meanwhile, the RBDO method was applied for a multi-objective design optimization of automative doors [115]. In aerospace engineering, the RBDO method was used for the optimal design of a 3D aeroelastic wing in order to maximize the surviving probability against the uncertainties from the design process and also the operation conditions[7]. So far, there are very few studies focusing on

enhancing the resistance of the building against progressive collapse through a design optimization.

During the last decade, design provisions and methodologies have been introduced to the current design guidelines, e.g. the UFC [29] and the GSA [42], aiming to mitigate the risk of progressive collapse. These design principles mainly fall into two categories: 1) indirect methods which typically involves enhancing the structural robustness (e.g. redundancy, ductility and connection strength) to allow for more load redistribution and 2) direct methods which intend to strengthen key structural components to resist potential abnormal loading events with the specific local resistance (SLR) method or improve the structural resistance for a given initial damage with the alternative load path (ALP) method. These design principles are prescriptive in nature and is unable to reveal the actual collapse risk of buildings. Therefore, the current design guidelines are not associated with the actual collapse risk.

In previous chapters, we have demonstrated that the proposed two-scale computational model and the simplified energy-based analysis method provide an efficient means for risk analysis of RC buildings subjected to given initial structural damage. By comparing the calculated collapse risk with the acceptable risk level, we are able to decide whether we need to pursue a structural strengthening scheme that can guarantee the acceptable collapse risk target.

In this chapter, we present a double-loop structural optimization scheme based on the proposed two-scale computational model. This entire optimization process is presented through the double-loop optimization procedure shown in Fig. 6.1. The outer loop is responsible for finding the most efficient structural strengthening scheme which minimizes the construction cost and the inner loop is used to quantify the collapse risk for a trial strengthening scheme. The RBDO framework is applied to perform a design optimization against progressive collapse for the prototype 10-story RC building

subjected to a two-column removal on the 9th story.

6.2 Optimization Methods

The general formulation for a standard optimization problem can be written as:

$$\min_{\forall \mathbf{s} \in \mathbf{S}} f(\mathbf{s}, \mathbf{x}), \mathbf{x} \in \mathbb{R}^n \tag{6.1}$$

$$\text{subjected to } g_l \leq g(\mathbf{x}) \leq g_h \text{ and/or } \mathbf{A}\mathbf{x} = a_t$$

In the above equation, $\mathbf{s}$ is a feasible solution belonging to the feasible domain $\mathbb{S}$; g_l and g_h represent the lower bound and upper bound of the nonlinear inequality constraints on the optimization problem while $\mathbf{A}\mathbf{x} = a_t$ is the linear equality constraint.

General speaking, the existing optimization methods can be classified into three categories according to the intended searching algorithm and searching scope [4]: 1) the gradient-based method, which can efficiently locate a local optimum solution by using the gradient information if available; 2) the non-gradient-based local method, which is used to search the optimal solution in the vicinity of the initial point without the aid of gradient information; and 3) the non-gradient-based global method, which is commonly used to find the global optimal solution especially when there are multiple local optimum solutions.

6.2.1 Gradient-Based Methods

The gradient-based methods are designed to efficiently solve the optimization problem, in which the gradient of the objective function is available. When the problem is non-smooth and discontinuous, this type of methods loses its robustness and efficiency. If the analytic gradient information is not available, the finite difference method can be used to compute the gradient of the objective function. Some commonly used gradient-based methods include:

- The classical Newton's method was initially used in calculus to find the solution of a differentiable function in an iterative form. It was then applied in solving an optimization problem by finding the location in the design space where the derivative of the objective function vanishes. This method has many variations, such as the quasi-Newton methods in [97] for minimizing the objective function guided by the gradient information.

- The Conjugate Gradient method firstly proposed by [48] in 1952 is an optimization algorithm initially developed for searching the optimal solution of systems with linear equations. It is often applied in large sparse systems along with an iterative algorithm when the large system size prevents a direct implementation, which is often the case for an optimization problem. This method is more suitable for optimization problems without constraints.

- The Sequential Quadratic Programming method [93] was developed to solve a specific type of optimization problem, the objective function and constraints of which have continuous derivatives. This method involves solving a set of sequential subproblems, each of which is essentially the optimization of a quadratic problem with linearized constraints. This method can be used for both linear and nonlinear constraints. Moreover, this method is equivalent to the aforementioned Newton's method for an unconstrained optimization problem.

- The Method of Feasible Directions (MFD) was first developed by [116] to solve optimization problems with nonlinear constraints for structural design. This method first starts from an initial point satisfying the constraints and then jump to a better point based on the information of useful directions, following which the objective function is reduced and the constraints are not violated at the same time.

6.2.2 Non-gradient-Based Local Methods

When the objective function is nonsmooth or has a poor behavior, the non-gradient-based methods are more robust than the gradient-based methods. Compared to the gradient-based method, the non-gradient-based method converges much slower. It often needs several hundreds or even thousands of iterations to get the exact local optimal solution. Some existing non-gradient-based methods include:

- The Pattern Search first developed by [51] is a optimization method for non-smooth or non-differentiable problems, which can be subjected to nonlinear constraints. For each trial, this method evaluates the objective function for a set of points based on a discrete mesh generated. Depending on whether an improvement is obtained or not, the mesh will be coarsened or refined. The iteration is continued until a converged solution is reached.

- The Greedy Search Heuristic method as implemented by [4] is an optimization algorithm which finds a local minimum at each stage. During each stage, this algorithm is short-sighted in nature for it searches the local minimum only in vicinity of the starting point while neglecting any better solution in the rest of design space. This temporary local minimum will be used as the initial point of the next stage. This method does not aim to find a global optimum and it will terminate after a reasonable number of stages due to the huge number of stages required by locating the global solution. However, these local solutions can be used to approximate the global optimum solution with an affordable computational cost.

6.2.3 Non-gradient-based Global Methods

Different from the non-gradient-based local methods, the non-gradient-based global methods can step over local optimum and eventually find the global optimal solution. Except with a global search scope, they are very similar to the non-gradient-based local methods in term of the absence of gradient information, the slow convergence rate and robustness in approaching nonsmooth or discontinuous optimization problems. The most popular non-gradient-based global method is so-called Evolutionary Algorithm (EA) [43]. The EA is usually considered to be one of the most efficient optimization methods for problems with multiple local optima or those where the calculation of gradient information is either too expensive or not feasible due to the discontinuous nature of the problem.

The EA was inspired by the evolution process in biology, which has several different types of breeding behavior, such as reproduction, crossover and mutation. During each generation, the evaluation for each individual is performed, based on which the best-fit individuals are selected for reproduction and others will be replaced by new individuals generated through crossover and mutation approaches. This evolutionary process continues till the optimal solution is obtained according to certain convergence criteria. Generally speaking, the EA is not efficient as mentioned earlier. Therefore, it is suggested that in order to efficiently reach the exact solution the non-gradient-based global method should be combined with the previously discussed gradient-based local method.

6.3 Design Optimization for Structural System against Progressive Collapse

Within the framework of the proposed two-scale computational model, the RBDO of RC buildings against progressive collapse is formulated as the minimization of the total energy dissipation capacity of all PDZs, which can be considered to be equivalent to the minimization of the retrofit cost. The objective function can be written as:

$$\min_{\forall \mathbf{s} \in \mathbb{S}} \sum [\alpha^{ij} (G^{ij}_{fn}(\mathbf{s}) + G^{ij}_{f\tau}(\mathbf{s}))] \tag{6.2}$$

subject to: $P_f \leq P_{f0}$, $G^{ij}_{fn} \geq G^{ij}_{fn0}$ and $G^{ij}_{f\tau} \geq G^{ij}_{f\tau 0}$

where $\mathbf{s} = [s_1, s_2, ..., s_n]$ is a specific structural strengthening scheme belonging to the set of all possible schemes $\mathbb{S}$, in which s_i defines the ratio between the current and the initial values of certain energy dissipation capacity; G^{ij}_{fk} ($k = n$ or τ) is the energy dissipation capacity of the ith PDZ and the jth integration point (IP) under normal or shear loading, respectively while G^{ij}_{fk0} is the corresponding energy dissipation capacity related with the initial structural design; P_f is the collapse probability with respect to the current structural design scheme while P_{f0} is the collapse risk target specified, e.g. 1.00%; α_{ij} is the area of the jth IP of the ith PDZ .

In order to find the most efficient and robust optimization algorithm, this structural optimization will be performed using three different types of optimization algorithms, which are 1) a gradient-based method, MFD, 2) a non-gradient-based global method, EA; and 3) a combination of the MFD method and the EA method. In this study, the non-gradient-based local method is not considered since this type of optimization algorithms does not suit for a large-scale structural optimization, which inevitably has multiple local optima. For the third optimization approach, the first phase of optimization with the non-gradient-based method (i.e. EA) is performed in search of the

region of interest containing the global optimum and then the second phase employs the gradient-based method (i.e. MFD) to locate the optimal retrofitting scheme within this region.

For a specific structural retrofitting scheme chosen by an optimization algorithm, the risk assessment of the building is performed with the probabilistic analysis based on the simplified energetic-equivalent method proposed in Chapter 5. As shown in Chapter 5, this simplified method can reasonably predict the upper bound of the actual collapse risk at an affordable computational cost. With this calculated collapse risk, we can decide whether a trial design scheme is a feasible solution, satisfying the constraint imposed by the user-specified collapse risk target.

6.4 Application to A 10-Story RC Building

Based on the risk assessment with the probabilistic analysis methods in Chapter 4 and 5, we find that the collapse risks for the prototype 10-story RC building shown in Fig. 4.7 under three column-removal scenarios are larger than 1%, a typical user-specified collapse level of $P[C|LD]$ for general-purpose buildings. Therefore, a RBDO will be needed to find the most efficient structural strengthening scheme to reduce the collapse risk to the target level for these three initial damage scenarios. As a demonstration, we will focus on the case of two-column removal on the 9th story.

6.4.1 Description

As discussed above, the structural optimization is performed with three different algorithms, MFD, EA and a combination of MFD and EA, respectively, to compare their efficiency and robustness when it comes to searching the global optimal structural retrofitting scheme. Each structural retrofitting scheme is represented by a set of design variables, s_i. For the optimization with the first two algorithms, a single optimization

method (i.e. either MFD or EA) is used and the optimization starts from the initial structural design, which means that no structural components will be strengthened, i.e. s_i=1. The search with these two algorithms is continued until the exact solution is found based on the convergence criteria that the difference of the increases in the total energy dissipation capacity of the building is smaller than 1% for two successive structural strengthening schemes

For the third optimization algorithm, due to its the hybrid nature, the optimization process is inevitably divided into two phases: 1) the search of the local region containing the global optimum with EA and 2) the pursue of the exact optimal solution within that local region with MFD. For the first phase, the search starts from the original structural design. The convergence criteria for the first phase is that: 1) for two most recent generations of design schemes the relative difference between the lowest two increments of total energy dissipation capacity is smaller than 5% and 2) the corresponding two retrofitting schemes have the same pattern, i.e. within the same region of the design space. With this local region identified by EA, the second phase of the optimization with MFD is initiated from the retrofitting scheme with the lowest increase in the total energy dissipation capacity during the first phase. This second phase of optimization searches the local minimum guided by the gradient information numerically calculated. We assume that the final solution is reached once the same convergence criteria as the first two optimizations is reached.

To reduce the optimization cost, we reduce the number of design variables (i.e. the ratio between the current and original energy dissipation capacities) by focusing on the structural strengthening of some key cohesive elements identified by the previous collapse risk assessment with the sequential analysis method in Chapter 5. The simulation results in Chapter 5 shows that most of the cohesive elements in all observed failure sequences are within four regions on each floor marked with red circles indicated by Fig.

5.3. The cohesive elements with highest failure frequencies are located in concentrated regions around three columns and in the middle of an exterior span, which comprise totally 8 regions above the removed columns on the 9th story. Within each optimization region, we assume there are two optimization design variables which strengthen the fracture energies of the effective concrete section in compression and shear (i.e. G_{fc} and G_{fs}) of all PDZs in that region, respectively. Meanwhile, the fracture energy of longitudinal reinforcement G_{st} and the fracture energy of effective concrete section G_{ft} in tension will not be strengthened. This is because previous simulation results in Chapter 4 and 5 indicate that the collapse of the prototype building is mainly initiated by the shear-dominant failure of cohesive elements around the column under the compression and shear interaction mode. Therefore, increase in tensile fracture energy of concrete and longitudinal reinforcement will not reduce the collapse risk effectively. During the optimization, each structural strengthening scheme, $\mathbf{s}$, represents a vector made up of 16 design variables, $\mathbf{s} = [s_1, s_2, ..., s_{16}]$, strengthening all PDZs in these 8 optimization regions.

For the rest of cohesive properties, the separations at peak and the ultimate points under single mode loading, w_{iu} and w_{iy} ($i = t, \tau$ and c) for the effective concrete section and the separations at the yielding and rupture points, w_{sy} and w_{su} for the longitudinal reinforcements are considered to be constant as indicated by Fig. 6.2. This means the peak strength and the initial stiffness for a specific mixed mode are proportional to the enhanced energy dissipation capacity. For the fracture energies of the effective concrete section in compression and shear (i.e. G_{fc} and G_{fs}), we only change the mean value and assume that the CoV is fixed during the optimization, which means that the standard deviation is linearly proportional to the increased mean value of the energy dissipation capacity.

Over the last decade, a number of practical strengthening measures have been proposed and tested to increase the shear and compressive resistances, which mainly involve the use of steel shear bolts and various types of fiber-reinforced polymer (FRP) sheets and bolts [106, 22]. In [5, 87], shear bolts made of FRP rods and steel reinforcement were developed, respectively, to enhance the shear resistance of RC slab-column connections to avoid a sudden and brittle failure due to shear. Meanwhile, glass fiber reinforced-ploymer (GFRP) sheets were recently applied in the slab retrofitting by [23] to increase the ultimate punching shear resistance.

6.5 Results and Discussion

As mentioned earlier, this structural optimization has been attempted with three optimization algorithms. The final results of these optimization attempts are listed in Table 6.1. For the optimization using MFD, it is observed that the optimization reaches a converged design scheme after 21 trial design schemes. However, all these 21 trial schemes are localized within the region close to the initial design point and don't satisfy the nonlinear constraint set by the collapse risk target as shown in Fig. 6.3. In this figure, the increases of objective function for all trial schemes are set to be a very large artificial value, 4000 kN·m instead of their actual values if the constraint is violated. This phenomenon is due to the fact that the MFD is a local gradient-based optimization method in nature, during which each new trial design scheme is obtained from the vicinity of the initial design point guided by the local gradient information. However, in order to obtain a feasible design scheme which satisfies the nonlinear constraint, the trial design scheme needs to be far away from the initial design point in the design space. This means that certain structural components need to be significantly strengthened to control the collapse risk when the initial collapse risk, i.e. 11.0% is considerably larger than the target value, 1.0%.

Considering the failure nature of the previous optimization with the single MFD method staring from the initial design, we make a second attempt with the same algorithm, yet starting from an over-strengthened scheme, with all design variables equal to "1.35". After 42 iterations, this optimization ends up with a converged feasible optimum solution, which yields an increase of the total energy dissipation capacity as 1162 kN·m. The convergence process of this optimization process is shown in Fig. 6.3. Compared with the solution obtained by the optimization with the third algorithm, we can find out that this optimal solution is in fact a local one instead of the global optimal solution. Therefore, this first algorithm using the single MFD algorithm is not suitable for thiss kind of global structural optimization with multiple local optimums.

For the second optimization using the EA only, we find that after 63 iterations EA is able to locate a local region of interest, satisfying the convergence criteria for the region of interest containing the global solution: 1) within two most recent generations the difference between the lowest two increments in the value of the objective function is no larger than 5% and 2) the corresponding two retrofitting schemes are in the same region of the design space. However, after identifying this region of interest, EA becomes inefficient in locating the exact solution because the best-performing scheme of each generation seems to oscillate within the region of interest and the reduction in objective function value is not significant in the following iterations even after 88 iterations, as shown in Fig. 6.3. Therefore, it is obvious that the first two algorithms are unsuitable and inefficient for RBDO of the present building against progressive collapse.

For the third optimization attempt, which utilizes EA and MFD, the first phase of the optimization procedure is the same as that of the above mentioned second optimization method. The second phase of this optimization with MFD starts with the solution obtained by the above mentioned second optimization attempt. During this second phase, the optimization with MFD starts from the design scheme with the best

performance obtained in the first phase and swiftly locates the exact global solution within 24 iterations based on the aforementioned convergence criteria, as shown in Fig. 6.3.

With the probabilistic analysis methods proposed in Chapter 4 and 5, the collapse risks related with the original structural design of the prototype building are 7.67% and 11.0%, respectively, for the two-column removal case on the 9th story. Through the aforementioned RBDO framework with a hybrid optimization algorithm, the optimal retrofitting scheme for the prototype building is obtained and the collapse risk for this specific initial damage scenario is controlled within 1.00%. For this final global optimal retrofitting design scheme, the values of all 16 design variables of the design vector, $\mathbf{s}$, are presented in Table 6.2 and the increase in total energy dissipation capacity of all PDZs in the building is found to be 796 kN·m. This total energy increase is the minimum amount of enhancement in fracture energy of all PDZs required by the structural retrofitting to protect this prototype building against the user-specified collapse risk target (i.e. 1.00 %) under the initial damage scenario of two-column removal on the 9th story.

Among these four optimization regions on each floor, the 1st, 2nd and 4th regions mainly involve the slab-column connections while the 4th region is the slab in an exterior span . From the results listed in Table 6.2, we can see that for the 1st, 2nd and 4th regions the increase in fracture energies in compression and shear on the 9th floor are relatively larger than those on the 10th story. This can be explained by the fact that the failure of PDZs in those region is mainly caused by the shear failure of the slab-column connections under gravity loading and also that the shear demands on the 10th story are relatively lower due to the reduced roof load.

Furthermore, we also notice that for the 1st region on each story the shear fracture energy requires more increase than the fracture energy in compression does while for the 2nd and 4th regions the opposite trend is observed. This interesting phenomenon can

be attributed to the mode mixity effect since under mixed-mode loading that is close to pure shear the increase in shear fracture energy will be more effective than that in the compressive one while the increase in the compressive fracture energy is more effective if compression is considerably involved in the mixed mode. From the calibration results of the mode mixity parameters under compression-shear interaction as shown in Fig. 3.2, we can see that both the peak strength and the energy dissipation capacity of a shear dominated case with $w_n/w_s = 0.5$ are several times larger than those in pure shear mode, which demonstrates that small amount of compression can greatly raise the overall resistance under a mixed mode.

Another interesting observation is that the 1st and 2nd regions require much more strengthening than the 3rd and 4th regions. This trend matches with the results seen in previous nonlinear dynamic analysis and the sequential linear elastic analysis, which indicate that the PDZ damage initially starts from the 1st and 2nd regions and gradually propagates to the 4th region and finally to the 3rd region. From this observation, we can conclude that the energy dissipation capacities of the PDZs in the 3rd and 4th regions are not as critical as those in the 1st and 2nd regions in preventing the damage propagation.

For values of design variables within the 3rd region on the 9th and 10th story, we observe that the increase of fracture energies on the 10th story are larger than those belonging to the 9th story, which actually turn out to be zero. This is opposite to the strengthening pattern we see in region 1, 2 and 4. This result is actually caused by the effect of the increased equivalent stiffness of the slab on the associated load redistribution among two stories. Based on the proposed simplified energy-based model, the increase in the fracture energy leads to the increase in the equivalent stiffness of the structural components. With an enhanced slab stiffness on the 10th story and an unchanged slab stiffness on the 9th story, the 10th story will help take over more gravity load from the

9th story. Therefore, we can conclude that both the energy dissipation capacities and the equivalent stiffnesses of the PDZs are important for mitigating the collapse risk.

6.6 Conclusion

A RBDO framework to search for the most effective retrofitting scheme to control the collapse risk of RC buildings is developed. After making four optimization attempts with three different algorithms, we find that the optimization with single gradient-based method (i.e. MFD) can swiftly locate a local minimum only close to the initial design point as demonstrated by the first two attempts and also that the optimization with the non-gradient-based method (i.e. EA) becomes inefficient in convergence when the optimization reaches the region close to the global solution. Thus, the final optimization framework is constructed on a hybrid optimization algorithm combining these two types of distinct optimization algorithms and also the risk assessment method proposed in Chapter 5. The framework is used to perform structural strengthening optimization of a prototype RC building for a target collapse risk. Based on the optimization results, we can conclude that: 1) structural strengthening should focus directly on the key elements in the critical regions where the local damage starts to propagate and 2) enhancing the stiffness of structural components in certain noncritical regions can help to allow for more load redistribution.

Table 6.1: Optimization results with three different algorithms.

Algorithm	Iter. number	Obj. inc. (kN·m)	Const. satisfied?	Converged?
MFD-1	21	31	No	Yes
MFD-2	42	1162	Yes	Yes
EA	88	838	Yes	No
EA & MFD	87	796	Yes	Yes

Table 6.2: Values of all design variables for the final optimal retrofitting scheme.

location	s_{c1}	s_{s1}	s_{c2}	s_{s2}	s_{c3}	s_{s3}	s_{c4}	s_{s4}
9th story	1.236	1.341	1.216	1.155	1.000	1.000	1.150	1.070
10th story	1.206	1.263	1.120	1.059	1.101	1.123	1.055	1.034

s_{ci} and s_{si} are design variables strengthening the compressive and shear energy dissipation capacities of PDZs in the ith region of each floor

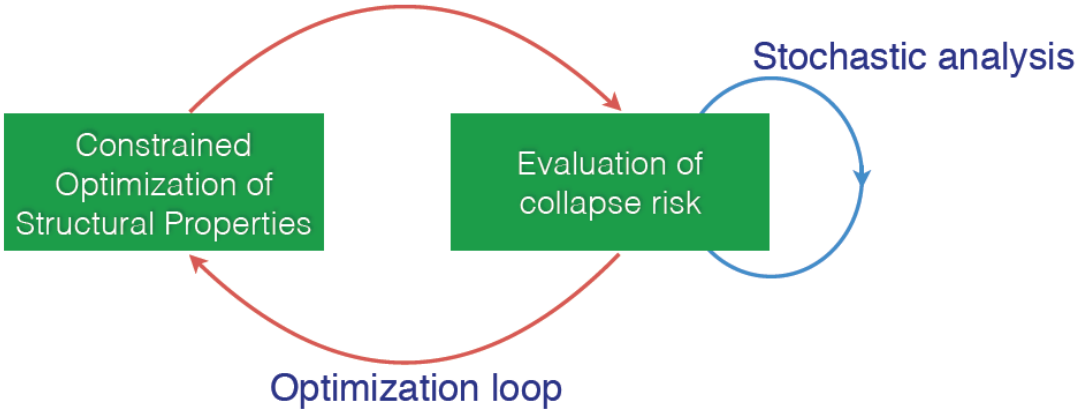

Figure 6.1: Double-loop optimization framework for collapse risk control.

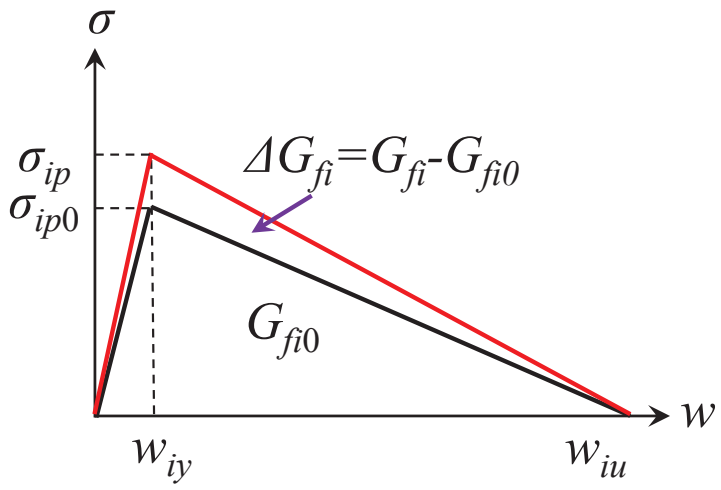

Figure 6.2: Strengthened traction-separation relationship for the PDZ ($i = s$ or c).

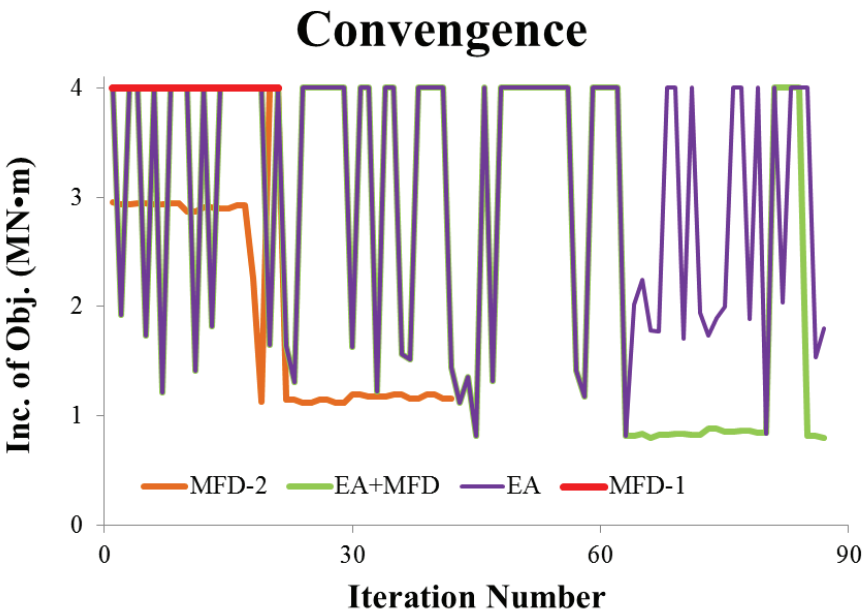

Figure 6.3: Curves of convergence for all four optimization attempts.

Chapter 7

Conclusions and Future Research

7.1 Conclusions

In this study, a new cohesive-fracture type computational model is developed to evaluate the collapse potential of RC buildings subjected to given initial structural damage. The accuracy of the two-scale model is validated both experimentally and numerically. The validation results show that the present model is capable of simulating the nonlinear behavior of various types of RC structural subassemblages, which includes the essential collapse resisting mechanisms such as arch effect, catenary effect and membrane effect, as well as the typical failure modes like the punching shear failure of slab-column connections. Meanwhile, the simulation of the 2D frame subassemblage shows that the present model is computationally efficient for it requires only about 2% of the computational time of the conventional FE analysis.

Based on this two-scale model, the probabilistic analysis is performed with the nonlinear dynamic analysis method to assess the collapse risks of a 2D RC frame structure and a 3D RC building with a flat-slab system. The risk assessment results show that the

two-scale model can successfully capture various collapse mechanisms including crush-down, crush-up, and lateral propagation of the crush-front. The probabilistic analysis takes into account different possible failure paths caused by the randomness of material properties and applied gravity loads, whereas the deterministic calculation only captures the dominant failure path that corresponds to the mean behavior. This causes some differences in the prediction of the effect of initial damage location on the overall collapse resistance. The comparison between the deterministic and probabilistic analyses shows that the conventional deterministic analysis suggested by UFC is sufficient for predicting a collapse event with an occurrence probability on the order of 5%. Such a collapse risk is generally acceptable for most conventional buildings. Nevertheless, for some sensitive RC buildings, where a lower collapse risk is required, probabilistic analysis becomes necessary.

To further reduce the high computational cost of the nonlinear cohesive modeling of RC structures in Chapter 4, a simplified energy-based cohesive model coupled with a sequential analysis method is proposed to quantify the collapse initiation risk of RC buildings. By comparing the risk assessment results with the nonlinear cohesive model and the simplified energy-based model, it is found that the simplified method is able to capture the same qualitative probabilistic collapse behavior as the nonlinear cohesive method does. In comparison with the nonlinear dynamic analysis, the simplified model can yield an reasonable upper bound of the collapse risk. Meanwhile, it is shown that the present model can reduce the computational time by a factor of 10-20 compared to the nonlinear dynamic analysis. It is found that the tradeoff between the accuracy of the collapse risk prediction and the improvement of computational efficiency indicates that the simplified method could be an attractive choice for the analysis of the collapse initiation risk of large-scale RC buildings.

Based on this simplified energy-based model, we develop a RBDO framework to

search for the most effective structural strengthening scheme to mitigate the collapse initiation risk of RC buildings. After performing design optimization with three different types of algorithms, the hybrid optimization algorithm combining the non-gradient-based and the gradient-based methods is found to be the most reliable and efficient algorithm in searching the optimal structural strengthening scheme. This RBDO framework is applied to the design optimization of the prototype 10-story RC building. The optimization results show that strengthening key elements in critical regions where the collapse front initiates and enhancing the equivalent stiffness of structural components in certain uncritical region are both effective in mitigating the collapse risk. Moreover, the application of this RBDO framework to this prototype 3D building demonstrates that the structural design optimization of RC buildings against progressive collapse can be realized with an affordable computational cost.

7.2 Outlook for Future Research

This study mainly focuses on the reliability-based analysis and design optimization of RC buildings against progressive collapse for a given initial structural damage scenario. In the future, the proposed framework can be improved or extended in the following aspects:

1. Though a reliability-based design optimization has been achieved at an affordable cost for a 3D 10-story RC building to mitigate the collapse risk, the computational cost could still be prohibitive for large-scale RC buildings. Further research efforts should be devoted to improving the efficiency of the design optimization by considering new optimization scheme or simplifying the risk analysis method.

2. The current two-scale model mainly focuses on the blast-induced collapse events, during which the columns and walls are removed suddenly. However, the current framework can be readily extended to perform the risk assessment and the subsequent

design optimization for RC buildings undergoing other types of natural or manmade disasters, such as earthquake and fire. For instance, by introducing an appropriate cohesive behavior for cyclic loading, the two-scale model can be adopted in the earthquake-induced collapse analysis of RC buildings.

3. In this study, we assume that a blast loading event always causes a local structural damage, which is modeled by removing key structural components instantly. However, in reality, the local damage may not occur during an abnormal event (e.g. fire, gas explosion and etc). Instead, these key elements can only suffer from limited amount of damage, which will not induce any immediate collapse initiation. However, the partially damaged structural components can severely deteriorate the long-term performance of buildings. It will be an important topic to investigate the effect of local structural collapse on time-dependent behaviors of the buildings. Such model requires the coupling between damage, creep and shrinkage mechanisms of RC structures.

4. Besides its application in building structures, the proposed risk quantification and design optimization procedure based on the two-scale can be extended to other types of civil structures, such as bridges. For bridges, ships may collide with bridge piers and lead to the potential collapse of the bridge immediately after the collision or during its subsequent service life. With the current two-scale model, the collapse risk and the reduction in the service life of bridge structures can be assessed. Furthermore, optimal retrofitting schemes can be designed to achieve a targeted collapse risk.

References

[1] ABAQUS 6.11 documentation *SIMULIA*, Providence, RI.

[2] American Concrete Institute Committee 318 (2011). *318-11 Building Code Requirement for Structural Concrete and Commentary.* American Concrete Institute, Farmington Hills.

[3] ACI Committee 408 (2003) *Bond and Development of Straight Reinforcing Bars in Tension*, Report No. ACI 408R-3.

[4] Adams, B., Bohnhoff, W., Dalbey, K., Eddy, J., Eldred, M., Gay, D., Haskell, K., Hough, P., Swiler, L. (2011) *DAKOTA, A Multilevel Parallel Object-Oriented Framework for Design Optimization, Parameter Estimation, Uncertainty Quantification, and Sensitivity Analysis: Version 5.2 User's Manual*, Sandia technical report SAND2010-2183.

[5] Adetifa, B., and Polak, M. A. (2005). "Retrofit of slab column interior connections using shear bolts." *ACI Structural Journal*, 102(2).

[6] Alashker, Y., Li, H. and El-Tawil, S. (2011) "Approximations in progressive collapse modeling." *J. Struct. Engrg., ASCE*, 137(9), 914–924.

[7] Allen, M. and Maute, K. (2004). "Reliability-based design optimization of aeroelastic structures." *Structural and Multidisciplinary Optimization*, 27(4), 228-242.

[8] Applied Technology Council. *Seismic Performance Assessment of Buildings Volume 1-Methodology, FEMA P-58-1.* Federal Emergency Management Agency, September 2012.

[9] Aycardi, L. E., Mander, J. B., and Reinhorn, A. M. (1994) "Seismic resistance of reinforced concrete frame structures designed only for gravity loads: experimental performance of subassemblages." *ACI Struct. J.* 91(5), 552–563.

[10] Bao, Y. (2008) *Macromodel-Based Progressive Collapse Simulation of Reinforced Concrete Structures*, Ph.D. Dissertation, University of California, Davis.

[11] Bao, Y., Kunnath, S. K., El-Tawil, S. and Lew, H. S. (2008) "Macromodel-based simulation of progressive collapse: RC frame structures." *J. Struct. Engrg., ASCE*, 134(7), 1079-1091.

[12] Bao, Y., Kunnath, S. K. (2010) "Simplified progressive collapse simulation of RC frame–wall structures." *Engrg. Struct.*, 32(10), 3153-3162.

[13] Barrenblatt, G. I. (1959) "The mathematical theory of equilibrium of cracks in brittle fracture." *Adv. Appl. Mech.*, 7, 55–129.

[14] Bažant, Z. P. (2005) *Scaling of Structural Strength*, Elsevier.

[15] Bažant, Z. P. and Cedolin, L. (1991) *Stability of Structures: Elastic, Inelastic, Fracture, and Damage Theories.* Oxford University Press, New York.

[16] Bažant, Z. P., Le, J.-L., Greening, F. R. and Benson, D. B. (2008) "What did and did not cause collapse of WTC twin towers in New York." *J. Engrg. Mech., ASCE*,

134(10), 892–906.

[17] Baŵant, Z. P. and Pang, S.-D. (2007) "Activation energy based extreme value statistics and size effect in brittle and quasibrittle fracture." *J. Mech. Phys. Solids*, 55, 91–134.

[18] Bažant, Z. P. and Planas, J. (1998) *Fracture and Size Effect in Concrete and Other Quasibrittle Materials*, CRC Press.

[19] Bažant, Z. P. and Verdue, M. (2007) "Mechanics of progressive collapse: Learning from World Trade Center and building demolitions." *J. Engrg. Mech., ASCE*, 133(3), 308–319.

[20] Bažant, Z. P., and Zhou, Y. (2002) "Why did the World Trade Center collapse?– Simple analysis." *J. Eng. Mech., ASCE*, 128(1), 2–6; with Addendum, 128(3), 369–370.

[21] Bennett, R. M. (1988) "Formulations for probability of progressive collapse." *Struct. Safety*, 5(1), 66–77.

[22] Carse, A., Spathonis, M. J., Chandler, M. L., Gilbert, M. D., Johnson, M. B., UWS, A. J., and Pham, L. (2002). *Review of strengthening techniques using externally bonded fiber reinforced polymer composites, Report 2002-005-C-01*, CRC for Construction Innovation, Brisbane.

[23] Chen, C. C., and Li, C. Y. (2005). "Punching shear strength of reinforced concrete slabs strengthened with glass fiber-reinforced polymer laminates." *ACI Structural Journal*, 102(4), 535.

[24] Cusatis, G., Bažant, Z.P. and Cedolin, L. (2003) "Confinement-shear lattice model for concrete damage in tension and compression: I. Theory." *J. Engrg. Mech.,*

ASCE, 129(12), 1439–1448.

[25] Camacho, G. T., and Ortiz, M. (1996) "Computational modeling of impact damage in brittle materials." *Int. J. Solids Struct.*, 33(20-22), 2899 – 2938.

[26] Cornell, C.A. (1996) "Reliability-based earthquake-resistant design; the future." In*11th World Conference on Earthquake Engineering*, Acapulco, Mexico.

[27] Darwin, D., Idun, E. K., Zuo, J. and Tholen, M. L. (1998) "Reliability-based strength reduction factor for bond." *ACI Struct. J.,* 95-S39.

[28] Dey, A. and Mahadevan, S. (1998) "Ductile structural system reliability analysis using adaptive importance sampling." *Struct. Safety*, 20:137–154.

[29] Department of Defense (DOD) (2009) *Design of Buildings to Resist Progressive Collapse, UFC-4- 023-03*, Washington, DC.

[30] Dugdale, D. S. (1960) "Yielding of steel sheets continuity slits." *J. Mech. Phys. Solids*, 8,100–104.

[31] Ellingwood, B.R. (2001) "Earthquake risk assessment of building structures." *Reliability Engineering and System Safety*, 74:251–262.

[32] Ellingwood, B. R. (2006) "Mitigating risk from abnormal loads and progressive collapse." *J. Perfor. Constr. Fac.*, 20(4), 315–323.

[33] Ellingwood, B. R. and Leyendecker, E. V. (1978) "Approaches for design against progressive collapse." *J. Struc. Div.*, 104(3), 413–423.

[34] Ellingwood, B. R., Smilowitz, R., Dusenberry, D. O., Duthinh, D., Lew, H. S., and Carino, N. J. (2007) *Best Practices for Reducing the Potential for Progressive Collapse in Buildings*, NISTIR 7396.

[35] Enevoldsen, I. and Sorensen, J.D. (1994) "Reliability-based optimization in structural engineering." *Struct. Safety*, 15(3):169–196.

[36] Elstner, R. C., and Hognestad, E. (1956) "Shearing strength of reinforced concrete slabs." *ACI J. Proc.*, 53(2), 29–58.

[37] Frangopol, Dan M., and Kurt Maute. "Life-cycle reliability-based optimization of civil and aerospace structures." *Computers & structures* 81.7 (2003): 397-410.

[38] Frangopol, Dan M., Kai-Yung Lin, and Allen C. Estes. "Life-cycle cost design of deteriorating structures." *Journal of Structural Engineering* (1997), 123(10), 13901401.

[39] Freed, Y. and Banks-Sills, L. (2008) "A new cohesive zone model for mixed mode interface fracture in bimaterials." *Engrg. Frac. Mech.* 75, 4583–4593.

[40] Grassl, P., and Bažant, Z.P., (2009) "Random lattice-particle simulation of statistical size effect in quasi-brittle structures failing at crack initiation." *J. Engrg. Mech. ASCE*, 135 (2), 85–92.

[41] Grierson, D. E., Xu, L., and Liu, Y. (2005) "Progressive-failure analysis of buildings subjected to abnormal loading." *Comp. Aided Civ. Infra. Engrg.* 20, 155–171.

[42] General Services Administration (GSA) (2003) *Progressive Collapse Analysis and Design Guidelines for New Federal Office Buildings and Major Modernization Projects*, Washington DC.

[43] Haftka R. T. and Grdal, Z. Elements of structural optimization[M]. Springer Science and Business Media, 2012.

[44] Haldar, A., and Mahadevan, S. (2000) *Probability, Reliability, and Statistical Methods in Engineering Design*, Wiley, New York.

[45] Hawkins, N. M., Bao, A. and Yamazaki, J. (1989) "Moment transfer from concrete slabs to columns?" *ACI Struct. J.*, 86(6), 705–716.

[46] Hansen, E., Levine, H., Lawver, D., and Tennant, D. (2006). "Computational failure analysis of reinforced concrete structures subjected to blast loading." *Proc.: the 17th Analysis and Computation Specialty Conference*, St. Louis, Missouri.

[47] Helmy, H., Salem, H., and Mourad, S. (2012) "Progressive collapse assessment of framed reinforced concrete structures according to UFC guidelines for alternative path method." *Engrg. Struct.*, 42, 127–141.

[48] Hestenes, M. R., and Stiefel, E. (1952). "Methods of conjugate gradients for solving linear systems." *Journal of Research of the National Bureau of Standards* vol.49 (6)

[49] Hillerborg, A., Modeer, M. and Petersson, P. E. (1976) "Analysis of crack formation and crack growth in concrete by means of fracture mechanics and finite elements." *Cem. Concr. Res.*, 6(6), 773–782.

[50] Hogberg, J. L. (2006) "Mixed mode cohesive law." *Int. J. Frac.*, 141, 549–559.

[51] Hooke, R., and Jeeves, T. A. (1961). "Direct Search Solution of Numerical and Statistical Problems." *Journal of the ACM (JACM)*, 8(2), 212-229.

[52] Izzuddin, B. A., Vlassis, A. G., Elghazouli, A. Y., and Nethercot, N. A. (2008) "Progressive collapse of multi-storey buildings due to sudden column losses? Part I: Simplified assessment framework." *Engrg. Struct.*, 30, 1308–1318.

[53] Jirásek, M. (1997) "Analytical and numerical solutions for frames with softening hinges." *J. Engrg. Mech., ASCE*, 123(1), 8-14.

[54] Jirásek, M. and Bažant, Z. P. (2002) *Inelastic Analysis of Structures*, Wiley.

[55] Kaewkulchai, G., and Williamson, E. B. (2004) "Beam element formulation and solution procedure for dynamic progressive collapse analysis." *Comp. Struct.*, 82, 639–651.

[56] Kaewkulchai, G. and Williamson, E. B. (2006) "Modeling the impact of failed members for progressive collapse analysis of frame structures." *J. Perform. Constr. Fac., ASCE*, 20(4), 375–383.

[57] Kameshwar, S. and Padgett, J.E. (2014) "Multi-hazard risk assessment of highway bridges subjected to earthquake and hurricane hazards." *Engrg. Struct.*, 78:154–166.

[58] Karamchandani, A., Bjerager, P. and Cornell, C.A. (1989) "importance sampling." In *Proceedings 5th International Conference on Structural Safety and Reliability*, pages 855–862, San Francisco, U.S..

[59] Kanoh, Y. and Yoshizaki, S. (1979) "Strength of slab-column connections transferring shear and moment?" *ACI J. Proc.*, 76, 461–478.

[60] Kent, D. C, and Park, R. (1971). "Flexural members with confined concrete." *J. Struct. Div., ASCE*, 97(7), 1969–1990.

[61] Khandelwal, K. and El-Tawil, S. (2008) "Pushdown resistance as a measure of robustness in progressive collapse analysis." *Engrg. Struct.*, 33, 2653–2661.

[62] Krauthammer, T. (2008) *Modern Protective Structures*, CRC Press, Boca Raton.

[63] Le, J. L. and Bažant, Z. P. (2011) "Why the observed motion history of World Trade Center towers is smooth." *J. Engrg. Mech., ASCE*, 137(1), 82–84.

[64] Le, J. L. and Xue, B. (2015) " Risk analysis of reinforced concrete buildings against progressive collapse: II. Simplified energetic-based analysis", *Journal of Structural Engineering, ASCE*, (under review)

[65] Le, J. L. and Xue, B. (2014) "Probabilistic analysis of reinforced concrete frame structures against progressive collapse." *Engrg. Struct.*, 76, 313–323.

[66] Lee, J. and Fenves, G. L. (1998) "Plastic-damage model for cyclic loading of concrete structures." *J. Engrg. Mech., ASCE*, 124(8), 892–900.

[67] Lew, H. S., Bao, Y., Sadek F., and Main, J. A. (2011) "An experimental and computational study of reinforced concrete assemblies under a column removal scenario." *NIST Technical Note 1720.*

[68] Li, Y. and Ellingwood, B.R. (2006) "Hurricane damage to residential construction in the US: Importance of uncertainty modeling in risk assessment." *Engrg. Struct.*, 28:1009–1018.

[69] Liu, J., Tian, Y., Orton, S. L. and Said, A. M. (2015) "Resistance of flat-plate buildings against progressive collapse. I: Modeling of slab-column connections?" *J. Struct. Eng.*, 04015053.

[70] Lowes, L. N. and Altoontash, A. (2003) "Modeling reinforced concrete beam-column joints subjected to cyclic loading." *J. Struct. Engrg., ASCE*, 129(12), 1686-1697.

[71] Low, H. Y. and Hao, H. (2002) "Reliability analysis of direct shear and flexural failure modes of RC slabs under explosive loading." *Engrg. Struct.*, 24(2), 189–198.

[72] McKay, M. D., Beckman, R. J., and Conover, W. J. (1979). "Comparison of three methods for selecting values of input variables in the analysis of output from a computer code." *Technometrics*, 21(2), 239-245.

[73] Mahadevan, S. and Raghothamachar, P. (2000)"Adaptive simulation for system reliability analysis of large structures." *Comp. Struct.*, 77:725–734.

[74] Mander, J. B., Priestly, J. N., Park, R. (1988) "Theoretical stress-strain Model for confined concrete," *J. Struc. Engrg., ASCE*, 114(8),1804–1826.

[75] Masoero, E., Wittel, F. K., Herrmann, H. J. and Chiaia, B. M. (2010) "Progressive collapse mechanisms of brittle and ductile framed structures." *J. Engrg. Mech., ASCE*, 136(8), 987–995.

[76] Melchers, R.E. (1989) "Importance sampling in structural systems." *Struct. Safety*, 6:3–10.

[77] Moehle, J. P. (1992) "Displacement-based design of RC structures subjected to earthquakes." *Earthquake Spectra*, 8(3), 403–428.

[78] Mori, Y. and Ellingwood, B.R. (1993) "Time-dependent system reliability analysis by adaptive importance sampling." *Struct. Safety*, 12:59–73.

[79] Morutsu, Y., Okada, H., Yonezawa,M. and Kishi, M. (1993) "Identification of stochastically dominant failure modes." In *Proceedings Fourth International Conference on Applications of Statistics and Probability in Soil and Structural Engineering*, pages 1325–1338, Florence, Italy.

[80] Mitra, N. and Lowes, L. N. (2007) "Evaluation, calibration, and verification of a reinforced concrete beam-column joint model." *J. Struct. Engrg., ASCE* 133(1), 105–120.

[81] Nguyen, T. H., Song, J., and Paulino, G. H. (2011) "Single-loop system reliability-based topology optimization considering statistical dependence between limit-states." *Structural and Multidisciplinary Optimization*, 44(5), 593-611.

[82] Panagiotou, M., Restrepo, J., Schoettler, M. and Kim, G. (2012) "Nonlinear cyclic truss model for reinforced concrete walls." *ACI Struc. J.*, Vol. 109, No. 2, p.p. 205-214.

[83] Park, J. and Kim, J. (2010) "Fragility analysis of steel moment frames with various seismic connections subjected to sudden loss of a column." *Engrg. Struct.*, 32(6), 1547-1555.

[84] Park, K., Paulino, G. H. and Roesler J. (2009) "A unified potential-based cohesive model of mixed- mode fracture." *J. Mech. Phys. Solids*, 57, 891–908.

[85] Pesce, C. P., Casetta, L., and dos Santos, F. M. (2012) "Equation of motion governing the dynamics of vertically collapsing buildings." *J. Engrg. Mech, ASCE*, 138(12), 1420–1431.

[86] Pham, X. D. and Tan, K. H. (2013) "Membrane action of RC slabs in mitigating progressive collapse of building structures." *Engrg. Struct.*, 55, 107–115.

[87] Polak, M. A., and Lawler, N. (2011). "Application of FRP for Punching Shear Retrofit of Concrete Slab-Column Connections." *In Advances in FRP Composites in Civil Engineering* pp. 854-857, Springer Berlin Heidelberg.

[88] Sadek, F., Main, J. M., Lew, H. S. and Bao, Y. (2011) "Testing and analysis of steel and concrete beam-column assemblies under a column removal scenario." *J. Struct. Engrg., ASCE*, 137, Special Issue Commemorating 10 Years of Research Since 9/11, 811-892.

[89] Sagiroglu, S. and Sasani, M. (2014) "Progressive collapse-resisting mechansims of reinforced concrete structures and effects of initial damage locations " *J. Struct. Engrg., ASCE*, 140(3), 04013073.

[90] Sasani, M., Kazemi, A., Sagiroglu, S., and Forest, S. (2011) "Progressive collapse resistance of an actual 11-story structure subjected to severe initial damage." *J. Struct. Engrg., ASCE*, 137(9), 893–902.

[91] Sasani, M. and Kropelnicki, J. (2008) "Progressive collapse analysis of an RC structure." *Struct. Design Tall Spec. Build.*, 17:757–771.

[92] Sasani, M. and Sagiroglu, S. (2008) "Progressive collapse resistance of Hotel San Deigo" *J. Struct. Engrg., ASCE*, 134(3), 478–488.

[93] Schittkowski K. NLPQLP: A Fortran implementation of a sequential quadratic programming algorithm with distributed and non-monotone line search-users guide[J]. 2006.

[94] Seffen, K. A. (2008) "Progressive collapse of the World Trade Center: Simple analysis." *J. Engrg. Mech., ASCE*, 134(2), 125–132.

[95] Sezen, H., and Moehle, J. P. (2003) "Bond-slip behavior of reinforced concrete members." *In fib - Symposium (CEB-FIP); Concrete Structures in Seismic Regions*, Athens, Greece.

[96] Shanley, F. R. (1947) "Inelastic column theory." *J. Aero. Sci.*, 14(5), 261–268.

[97] Shanno, D. F. "Conditioning of quasi-Newton methods for function minimization". *Mathematics of computation*, 1970, 24(111): 647-656.

[98] Shi, Y., Hao, H. and Li, Z.-X. (2008) "Numerical derivation of pressure-impulse diagrams for prediction of RC column damage to blast loads." *Int. J. Impact Engrg.*, 35(11), 1213– 1227.

[99] Song, B. I. and Sezen, H. (2013) "Experimental and analytical progressive collapse assessment of a steel frame building." *Engrg. Struct.*, 56, 664–672.

[100] Song, J. and DerKiureghian, A. (2003) "Bounds on system reliability by linear programming." *J. Engrg. Mech., ASCE*, 129(6):627–636.

[101] Song, J. and Kang, W.-H. (2009) "System reliability and sensitivity under statistical dependence by matrix-based system reliability method."*Struct. Safety*, 31:148–156.

[102] Spence S. M. J. and Gioffr M. "Efficient algorithms for the reliability optimization of tall buildings". *Journal of Wind Engineering and Industrial Aerodynamics*, 2011, 99(6): 691-699.

[103] Spence S. M. J. and Gioffr M. "Large scale reliability-based design optimization of wind excited tall buildings". *Probabilistic Engineering Mechanics*, 2012, 28: 206-215.

[104] Szyniszewski, S. and Krauthammer, T. (2012) "Energy flow in progressive collapse of steel framed buildings." *Engrg. Struct.*, 42, 142–153.

[105] El-Tawil, S., Li, H., and Kunnath, S. (2014) "Computational simulation of gravity-induced progressive collapse of steel-frame buildings: Current trends and future research needs." *J. Struct. Engrg., ASCE*, 140, Special Issue: Computational Simulation in Structural Engineering, A2513001.

[106] Ueda, T. and Shimomura, T. *Guidelines for Retrofit of Concrete Structures*, Concrete Library No. 95, JSCE, September 1999

[107] Vecchio, F. J. and Collins, M. P. (1986) "The modified-compression field theory for reinforced-concrete elements subjected to shear." *ACI J.*, 83(2), 219–231.

[108] Vlassis, A. G., Izzuddin, B. A., Elghazouli, A. Y., and Nethercot, D. A. (2009) "Progressive collapse of multi-storey buildings due to failed floor impact." *Engrg. Struct.*, 31(7), 1522–1534.

[109] Wierzbicki, T., and Teng, X. (2003) "How the airplane wing cut through the exterior columns of the World Trade Center." *Int. J. Impact Engrg.*, 28, 601–625.

[110] Xiao, Y., Zhao, Y. B., Li, F. W., Kunnath, S., and Lew, H. S. (2013) "Collapse test of a 3-story half-scale RC frame structures." *Proc. Structures Congress, ASCE*, 11–19.

[111] Xu, G. and Ellingwood, B. R. (2011a) "Probabilistic robustness assessment of pre-Northridge steel moment resisting frames." *J. Struct. Engrg., ASCE*, 137(9), 925–934.

[112] Xu, G. and Ellingwood, B. R. (2011b) "An energy-based partial pushdown analysis procedure for assessment of disproportionate collapse potential." *J. Constr. Steel Res.*, 67, 547–555.

[113] Xu, X. P. and Needleman, A. (1993) "Void nucleation by inclusion debonding in a crystal matrix." *Model Simul. Mater. Sci. Engrg.*, 1(2):111–132.

[114] Xue, B. and Le, J.-L (2015) "Risk Assessment of Reinforced Concrete Buildings against Progressive Collapse." *ACI Structural Journal Special Issue* 2015. (Under review)

[115] Zou, T. and Mahadevan, S. (2006) "Versatile formulation for multiobjective reliability-based design optimization." *Journal of Mechanical Design*, 128(6): 1217-1226.

[116] Zoutendijk, G. (1960). "Methods of feasible directions: a study in linear and non-linear programming", Elsevier, Amsterdam

Vita

Born in Wuxi, Jiangsu Province, China, Bing Xue obtained his Bachelor of Science and Master of Science in Theoretical and Applied Mechanics from University of Science and Technology of China (USTC) in 2004 and 2007, respectively. After graduation with his master degree, he worked as a structural engineer in the A+E Design Division of the China Electronics Engineering Design Institute. In 2011, he started his doctoral studies in Civil Engineering focusing on structural mechanics at University of Minnesota under Professor Jia-Liang Le's advisorship. His research interests include: solid mechanics, computational mechanics, fracture mechanics and reliability analysis. His journal publications include:

1. B. Xue and J.-L. Le, Simplified Energy-Based Analysis of Collapse Risk of Reinforced Concrete Buildings, *Structural Safety* (under review)

2. B. Xue and J.-L. Le, A Stochastic Numerical Model for Progressive Collapse of Reinforced Concrete Buildings, *Journal of Structural Engineering* (under review)

3. B. Xue and J.-L. Le, Risk Assessment of Reinforced Concrete Buildings against Progressive Collapse, *ACI Structural Journal* (under review)

4. J.-L. Le, M. DesHarnais, B. Xue, S. D. Pang and H. Du, A Two-Scale Thermo-mechanical Computational Model for Reinforced Concrete Frames, *Engineering Structures* (under review)

5. J.-L. Le and B. Xue, Probabilistic Analysis of Reinforced Concrete Frame Structures against Progressive Collapse, *Engineering Structures*, 76 (2014): 313-323.

6. J.-L. Le and B. Xue, Energetic-Statistical Size Effect in Fracture of Bimaterial Hybrid Structures, *Engineering Fracture Mechanics*, 2013;111:106-115

7. J.-L. Le and B. Xue, Influence of Stress Singularities on Scaling of Fracture of Metal-Composite Hybrid Structures, *CMC: Computers, Materials & Continua*, 34 (2013): 251-264.

8. B. Xue, H.Wu, X. Wang, Z. Lian and J. Zhang, A Three-Dimensional Finite Element Model of Hydraulic Progressive Damage, *Key Engineering Material* Vols. 324-325 (2006) pp. 375-378.